CONTROL AND CHARACTERIZATION OF PHASE-MODULATED CONTINUOUS-WAVE LASER FREQUENCY COMBS

A Dissertation
Submitted to the Faculty
of
Purdue University
by
Chen-Bin Huang

In Partial Fulfillment of the
Requirements for the Degree
of
Doctor of Philosophy

May 2008
Purdue University
West Lafayette, Indiana

This dissertation is dedicated to my parents, Kun-Gin Huang and Yen-Sen Chang,
from whom I learned the values of diligence and endurance.

ACKNOWLEDGMENTS

I would like to acknowledge my gratitude towards Professor Andrew M. Weiner for providing me the research environment, his superb guidance, constant support and patience in every aspect. Without his trust and encouragement, I could not have gone this far. His never-ending pursuit in truth, kindness and fairness essentially set the best role model for me. To my Advisory Committees, Professor Michael R. Melloch, Professor Timothy D. Sands, and Professor Vladimir M. Shalaev, thank you for spending a considerable amount of time caring about my works and providing valuable instructions.

I am greatly indebted to Dr. Zhi Jiang, for his generosity in passing down his knowledge, his good will in welcoming my participation in line-by-line shaping, and countless inspiring conversations. I only wished I could have been smarter and we had more overlap.

Enormous appreciations are to Dr. Daniel E. Leaird, for all his efforts in making things work and at the same time making my everyday in the lab enjoyable. It would not have been as productive without his technical guidance and fruitful discussions.

Special thanks to Dr. Jason D. McKinney, for his valuable inputs and enlightenment in microwave photonics.

To Prof. Sany-Gyu Park: thank you for advises, especially for the DPSK work.

Thanks to the line-by-line shaping members: Houxun Miao, Supradeepa Venkata, and Fahmida Ferdous. Thanks to all group members in our lab for their friendship and support.

To my parents: you are the best Moms and Dads a child could ever want.

To my brother and sister-in-law: you provided all the warmth and support. Especially you gave birth to my super cute nephew, Bear.

Most importantly, my sincere thanks go to Ling-Ti, my lovely wife, for her immeasurable love and support, bringing joy to my life everyday.

TABLE OF CONTENTS

LIST OF TABLES

LIST OF FIGURES

Figure Page

Figure Page

Figure Page

Figure Page

Figure Page

LIST OF ABBREVIATIONS

Abbreviation	**Interpretation**
ASE	Amplified spontaneous emission
BER	Bit-error rate
CW	Continuous-wave
DDF	Dispersion decreasing fiber
DPSK	Differential phase-shift keying
EDFA	Erbium-doped fiber amplifier
ESA	Electrical spectrum analyzer
FWHM	Full-width half-maximum
HNLF	Highly nonlinear fiber
IM	Intensity modulator
LCM	Liquid crystal modulator
MLL	Mode-locked laser
NOLM	Nonlinear optical loop mirror
NSE	Nonlinear Schrödinger equation
OAWG	Optical arbitrary waveform generation
OSA	Optical spectrum analyzer
OSNR	Optical signal to noise ratio
PBS	Polarization beam splitter
PM	Phase modulator
PMCW	Phase-modulated continuous-wave
PS	Pulse shaper
PZT	Piezo-electric transducer
RF	Radio frequency
RMS	Root-mean-square
SC	Supercontinuum
SHG	Second harmonic generation
SPM	Self-phase modulation
SSF	Split-step Fourier

ABSTRACT

Huang, Chen-Bin Ph.D., Purdue University, May 2008. Control and Characterization of Phase-Modulated Continuous-Wave Laser Frequency Combs. Major Professor: Andrew M. Weiner.

Spectral line-by-line shaping is a key enabler towards optical arbitrary waveform generation, which promises broad impact both in optical science and technology. Significant new physics arises in the line-by-line regime, where the shaped pulse fields generated from one laser pulse now overlap with those generated from adjacent pulses. This leads to coherent interference effects related to the properties of optical frequency combs which serve as the source in these experiments.

Phase-modulated continuous–wave (PMCW) laser frequency combs are chosen as the optical source within this dissertation for their relatively high frequency stability and ease of tuning. We experimentally demonstrate the followings: (1) 300 fs optical pulse train generations at 9 and 10 GHz rates by applying line-by-line control to PMCW combs. (2) 5 GHz optical arbitrary waveform generations using more than 100 comb lines. (3) Generations of reprogrammable microwave arbitrary waveforms at rates approaching 10 GHz. (4) Generation of nonlinearly broadened optical frequency combs from PMCW seed pulses using both anomalous and normally dispersive media. Broadened comb coherence properties are further analyzed using differential phase-shift keying decoding. (5) Quantitative analysis on the impact of static comb frequency stability on line-by-line shaped waveforms. (6) Systematic investigations on time-varying comb frequency-noise to intensity-noise conversion in line-by-line shaping.

1. INTRODUCTION

The central theme of this dissertation is generation, control and characterization of optical frequency combs using spectral line-by-line shaping. In this chapter, basic introductions to optical frequency combs and spectral line-by-line shaping are provided.

1.1 Optical frequency comb sources

An optical frequency comb is comprised of complex electrical field lines in the form

$$E(f) = \sum_{m=0}^{\infty} A_m \delta(mf_{rep}) \exp(j\phi_m) \tag{1.1}$$

where f_{rep} denotes the repetition frequency, δ the Kronecker delta function, A_m and ϕ_m are the amplitude and phase of the mth comb line, respectively. Figure 1.1(a) depicts an ideal comb: all field lines are having the same amplitude and phase.

Traditionally, optical frequency combs have been derived from mode-locked lasers. Mode-locked laser combs typically exhibit Gaussian envelope due to the gain profile, as shown in Fig. 1.1(b), with the comb lines all in phase. In reality, comb lines are not at the absolute frequency positions due to the difference between phase and group velocities within the laser media, resulting in a frequency offset ε to each comb lines, with the comb line frequencies now at

$$f_m = mf_{rep} + \varepsilon \tag{1.2}$$

A typical mode-locked laser frequency comb with frequency offset is illustrated in Fig. 1.1(b). For mode-locked lasers, ε is time-varying and can undergo large variations without stabilization mechanisms. From a frequency domain perspective, stabilization of the frequency offset positions of the spectral lines of mode-locked lasers is highly desirable and has been recently achieved [1]. The resulting optical frequency combs have led to enormous progress in precision optical frequency synthesis and metrology [2], with uncertainties reported at the 10^{-19} level [3].

As a result of uniform spectral line phases of the frequency comb, in the time-domain, mode-locked lasers generate pulsed envelope function through a simple Fourier transform relation. Figure 1.1(c) shows the time-domain intensity i(t), where the pulse repetition time T is related to the inverse of f_{rep}. The full-width at half maximum (FWHM) temporal width τ is inversely proportional to the FWHM of the comb spectral bandwidth Δ. Note that the magnitude of the time-domain intensity waveforms from a mode-locked laser output is invariant of the comb frequency instability, but the carrier-envelope phase varies and has been measured [4].

Another type of optical frequency comb can be obtained by phase-modulating a continuous-wave laser (PMCW) in the time-domain, as pictured in Fig. 1.2(a). Under normal modulation, the output time-domain field can be mathematically described using Bessel's series of the first kind [5]:

$$E(t) = E_0 \exp\{j(\omega_0 t - \beta \cos(\omega_{rep} t))\} = E_0 \sum_{m=-\infty}^{\infty} J_m(\beta) \exp\{j(\omega_0 - m\omega_{rep})t\} \tag{1.3}$$

where $\omega=2\pi f$ is the frequency in radians, ω_0 the carrier frequency and $\beta=\pi V_p/V_\pi$ is the modulation index. V_p is the applied peak signal voltage and V_π the voltage required to create a π phase shift by the modulator. In the frequency-domain, comb line amplitudes are defined by the values of $J_m(\beta)$ and are spaced by f_{rep}. As a result of the Bessel series, electrical fields of the PMCW comb lines may show abrupt 0 and π relative phase jumps between two adjacent lines. Figure 1.2(b) shows a typical PMCW comb with modulation frequency of 9 GHz and driven at $2V_\pi$. Special attention should be paid to the fact that although a well defined frequency comb is generated in the frequency-domain, in the time-domain, the modulated field is still CW.

This "modulation-of-CW" scheme has the significant advantage that frequency offset and coherence of individual lines are controlled by the input CW laser and are decoupled from the pulse generation process; this provides a degree of control not yet readily available at high (> 2.5 GHz) repetition rate from mode-locked sources. A drawback is that timing jitter is impacted by the driving electronics (also the case for harmonically mode-locked lasers). However, for purposes of this dissertation this should not limit our ability to work in the "stable enough" regime. In this dissertation we operate the laser with offset frequency wanders of less than a few percent of the line spacing. This small wander is stable enough to remain centered on a specific spectral control element, which should permit high quality shaping. Femtosecond optical pulse generation at 9 and 10 GHz rate from a PMCW comb will be described in Chapter 2 [6].

1.2 Spectral line-by-line shaping

Ultrafast optical pulse shaping, a technique in which intensity and phase of frequency comb lines are controlled in the spectral-domain using a liquid crystal modulator (LCM), has been well developed throughout the years [7]. Through programmable manipulation of the comb lines, pulse shaping is capable of generating user-defined time-domain waveforms, also referred to as optical arbitrary waveform generation (O-AWG). In the past, pulse shapers have been constructed in a regime where group of lines are being controlled with the same parameter. Figure 1.3(a) illustrates a group-of-line shaper, in which one LCM pixel controls three comb lines (M=3) in the spectral-domain. In the time-domain, the periodicity of the generated waveforms is still T, but the maximum allowed pulse span is T/M (inverse of spectral resolution). This means the complexity of the generated waveforms is limited, regardless of the number of comb lines used.

In order to realize true O-AWG, frequency comb lines must be independently controlled (line-by-line shaping). Figure 1.3(b) illustrates the impact of a line-by-line shaper, in which the spectral resolution is increased so independent intensity and phase control to each comb line is allowed. As a consequence, the waveform span in the time-domain may well extend beyond a single period (> 100% duty factor), enabling the complexity required by O-AWG [8]. Another essential impact as a result of line-by-line shaping is that within the overlapped regimes, fields from different contributing pulse envelope interact in a coherent manner, sensitive to the comb frequency offset ε [9]. Thus, manipulation of individual spectral lines leads to a new regime in which the advantages of pulse shaping and of stabilized frequency combs can be simultaneously realized. Quantitative analysis on the impact of static comb frequency shift through line-by-line shaped waveforms are presented in Chapters 5 [10].

Figure 1.4 shows the schematic of our line-by-line shaper. The line-by-line shaper is a grating-based, fiber coupled Fourier-Transform pulse shaper which incorporates a 2×128 pixel LCM array to independently control both amplitude and phase of each spectral line. The individual liquid crystal pixels can be electronically controlled to give precise amplitude control and a phase manipulation in the range of 0 to 2π after a proper calibration [7]. In achieving line-by-line control, pulse shaper design needs great care for spectral resolution improvement. A reflective fiber coupled pulse shaper is constructed, which includes a collimator and telescope combination to produce a collimated beam with ~18 mm diameter, an 1200 grooves/mm grating, a lens with 1000 mm focal length, a LCM with a 12.8 mm aperture and 2×128 independent pixels, a metal mirror, and a circulator. The amplitude suppression of the comb lines are achieved by polarization rotation defined by the LCM pixels, introducing loss through the polarization beam splitter on the way reflected back to the circulator. The typical line intensity suppression achieved is around 28 dB. The fiber coupled input-output loss of the pulse shaper is around 10 dB. The measured resolution (bandwidth controlled by an individual LCM pixel) agrees well with the calculated value of 4.5 GHz. Table 1.1 lists all the pertinent parameters of our line-by-line shaper.

1.3 Organization of the dissertation

This dissertation is organized as follows: In Chapter 2, experimental results of femtosecond pulse generation at high repetition rate from phase-modulated CW laser frequency comb is presented. Optical pulse pedestal suppression is also demonstrated using a nonlinear optical loop mirror. We further demonstrate 5 GHz optical arbitrary waveform generations using more than 100 comb lines. In Chapter 3, the fastest generation of reprogrammable microwave electrical arbitrary waveforms at rates approaching 10 GHz are explored. In Chapter 4, generation of nonlinearly broadened optical frequency combs from PMCW seed pulses using both anomalous and normally dispersive media are studied. Broadened comb coherence properties are further analyzed using differential phase-shift keying decoding. In Chapter 5, quantitative analysis on the impact of ***static*** comb frequency offset over line-by-line shaped waveforms are presented. In Chapter 6, systematic investigations on ***time-varying*** comb frequency-noise to intensity-noise conversion in line-by-line shaping are presented. The last chapter provides conclusions and future prospects.

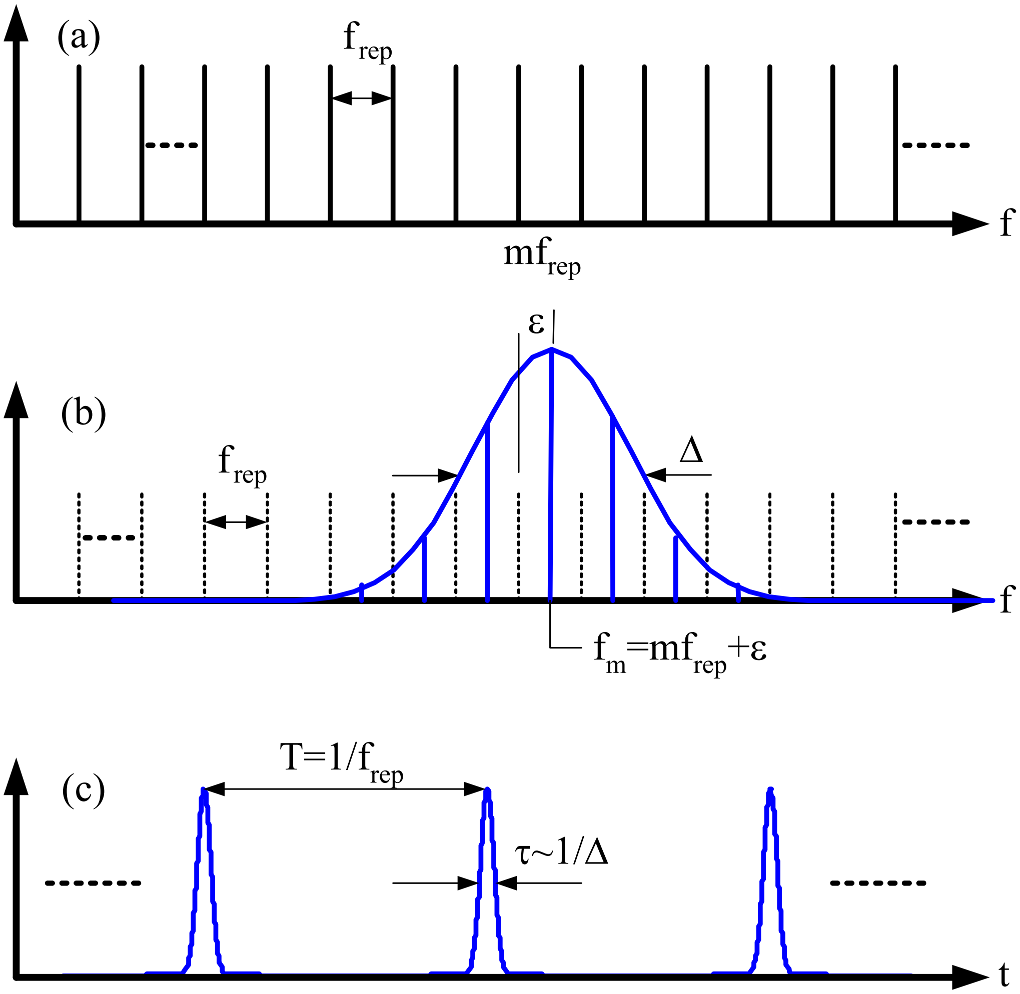

Fig. 1.1. (a) Ideal frequency comb; (b) frequency comb from a mode-locked laser and (c) time-domain pulse from a mode-locked laser.

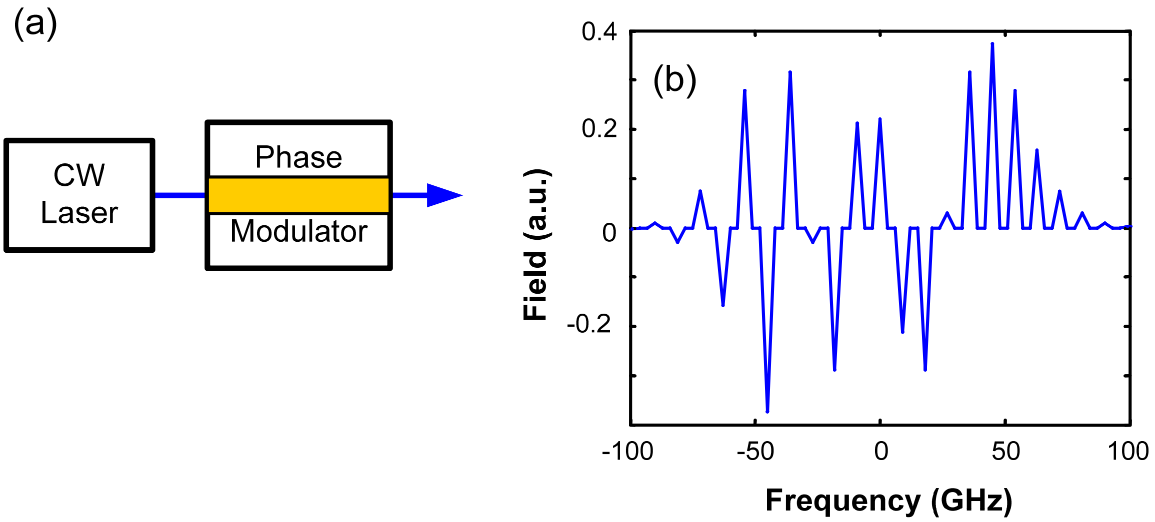

Fig. 1.2. (a) Schematic of a PMCW comb. (b) Fields of calculated phase-modulated comb lines.

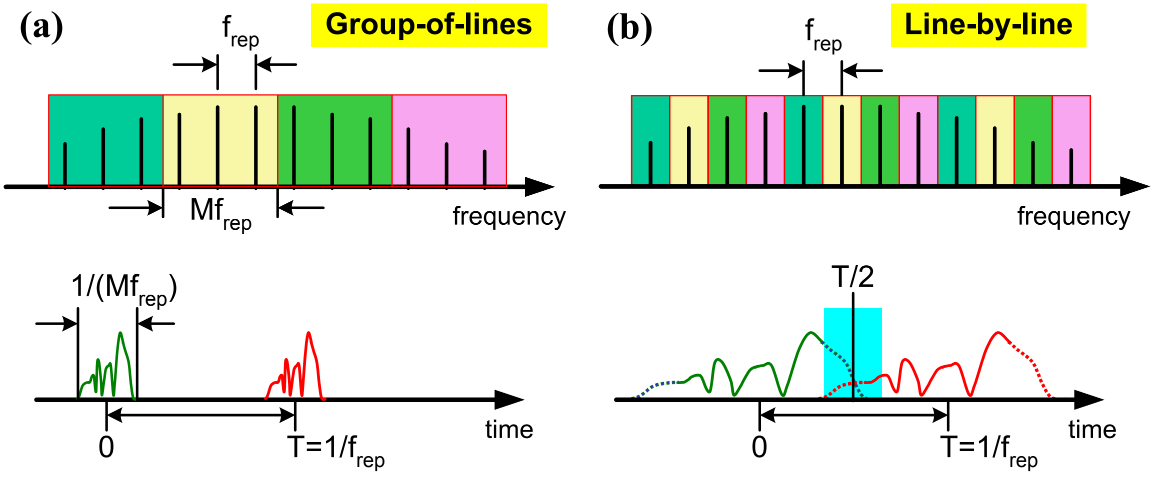

Fig. 1.3. Schematics of (a) Group-of-line shaping; (b) line-by-line shaping.

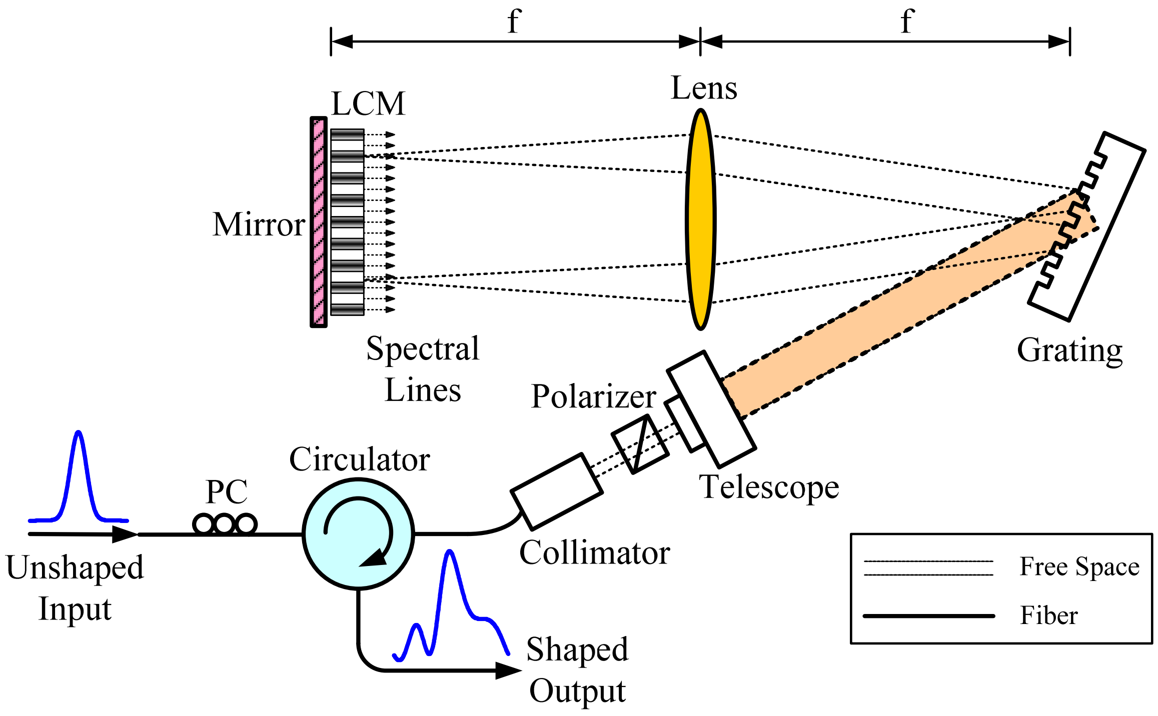

Fig. 1.4. Schematic of a spectral line-by-line shaper. LCM: liquid crystal modulator.

Table 1.1. Parameters of the reflective, grating-based line-by-line shaper.

Beam diameter after telescope *	**Grating groove**	**Grating diffraction angle**	**Lens focal length**
18 mm	1200 lines/mm	65 degree	1000 mm
Spectral bandwidth	**Minimum 3db bandwidth**	**Resolution****	**Loss**
4.5 nm	2.6 GHz	75 µm	10 dB

*: Beam diameter is defined as $1/e^2$ peak intensity.
**: Resolution is defined as beam diameter at LCM layer.

2. LINE-BY-LINE CONTROL ON A PHASE-MODULATED CONTINUOUS-WAVE LASER FREQUENCY COMB

In this chapter we demonstrate high repetition rate, ultafast optical pulse train generations using externally modulated CW laser frequency combs [6]. Subsequent pulse pedestal removal using a nonlinear optical loop mirror is experimentally demonstrated . 5 GHz optical arbitrary waveform generations using more than 100 comb lines are also performed in the last section.

2.1 Introduction

High repetition rate optical pulses in the few picosecond range and below are playing an increasingly important role in high speed optical fiber communication systems and optical networks, in areas such as return-to-zero format transmission, optical time-division-multiplexing and optical code-division-multiple-access. Such high repetition rate short pulses are routinely generated by harmonically mode locked lasers [11], but with the following limitations: (1) complicated feedback control is required which contributes to high cost; (2) the mode-locked frequency comb has limited tuning ability, both in terms of the absolute positions of the spectral lines and their separation; (3) at high repetition rates, the optical frequency combs from harmonically mode-locked lasers often suffer from frequency instability, which hinders their use in coherent communications and other applications where optical coherence is important. Alternatively, applying a strong periodic temporal phase modulation to a CW laser can generate a well-defined, broad comb of spectral lines [12], which can support short pulse generation after appropriate control of the spectral amplitude and phase. For example, a modulated CW laser followed by single mode fiber or other dispersion control components has been demonstrated for pulse generation [5,13-14]. Recently we demonstrated spectral line-by-line pulse shaping on frequency comb derived from a modulated CW laser to generate ~12 ps pulses at 9 GHz [15]. Line-by-line pulse shaping significantly extends the capability of optical processing with a modulated CW laser since the intensity and phase of all individual spectral lines can be independently and programmably controlled [9]. For example, using line-by-line control a transform-limited pulse train can be readily achieved, which still remains a challenge for other approaches. However, only a very limited number of lines (~10 lines or fewer) have been controlled in previous demonstrations [15]. Very recently an arrayed waveguide grating device was used to manipulate ~20 spectral lines also generated from a modulated CW laser, resulting in pulses as short as 4.7 ps [16]. The number of spectral lines to be controlled is one of the most important parameters for all applications: (1) for short pulse generation, more spectral lines correspond to shorter pulses assuming the same line spacing and pulse repetition rate; (2) generally for optical arbitrary waveform generation [8], the number of spectral lines determines the degree of complexity of the optical waveforms that can be generated. In this Chapter we report line-by-line pulse shaping on a phase modulated CW laser to generate and control over 40 lines, resulting in 2.76 ps pulse generation at 9 GHz repetition rate. This pulse width is comparable to those from typical harmonically mode-locked lasers at similar repetition rate, and thus can be further compressed down to 324 fs using a commercially available dispersion decreasing fiber. Compared with harmonically mode-locked lasers, short pulses generated in this way have significant advantages including simple control, low cost, and a tunable and a stable optical frequency comb (limited by the CW line-width and noise from the driving electronics).

2.2 Femtosecond optical pulse train generation

Figure 2.1 shows the schematic for our experimental setup. A CW laser with a specified line-width of 1 kHz at 1542nm (Koheras Adjustik) is used as an input source to provide for a stable generated comb. A low V_π lithium niobate phase modulator (20GHz bandwidth, V_π of ~3V at 1 GHz) is modulated at 18GHz (obtained by sending the 9 GHz RF signal to a ×2 RF frequency multiplier) with a driving voltage of ~4.8 V_π peak to peak to provide wider comb bandwidth than our previous report [15]. A second lithium niobate phase modulator (12.5 GHz bandwidth, V_π ~5V at 1 GHz) is driven at 9 GHz (~1.6 V_π peak to peak) to obtain a comb with spacing equal to the fundamental 9 GHz driving frequency. The first phase modulator driven at 18 GHz provides a broader spectral bandwidth, while the second modulator driven at 9 GHz fills in the missing lines while doubling the number of lines. Relative RF drive phases are adjusted by tuning a RF delay line to balance the power distribution among the 18 and 9 GHz comb lines. The comb lines are manipulated by our reflective line-by-line pulse shaper [8]. The modified comb lines are amplified via an erbium-doped fiber amplifier (EDFA) and sent to a non-collinear autocorrelator for pulse measurement and to an optical spectrum analyzer (OSA) for optical spectrum measurement with a resolution of 0.01nm.

Figure 2.2(a) shows the frequency comb without line-by-line control. Limited in part by the RF driving power to the second phase modulator, there is ~7 dB power variation among the central 30 lines. Figure 2.2(b) shows the resulting frequency comb with both intensity equalization and phase correction from the line-by-line pulse shaper. The comb lines are shown with solid lines while the designed apodization function (a super-Gaussian of 8th order) is shown with dots. Figure 2.2(b) indicates our capability of equalizing the intensities of the lines by demonstrating 28 lines within 1 dB, 35 lines within 10 dB, and 44 lines within 20 dB power levels off the peak, respectively. Relative phase differences between various pairs of spectral lines are determined by monitoring the relative temporal delays of the time-domain waveform on a sampling scope [17]. In an automated process, the line-by-line shaper is programmed to pass only two adjacent lines at a time; the resulting time-domain cosine waveforms on the sampling scope are recorded for delay calculations, and hence the relative spectral phase between each pair of two lines can be deduced. Figure 2.2(c) shows normalized experimental (dotted) and theoretical (solid) autocorrelation traces for the frequency comb shown in Fig. 2.2(b). The theoretical trace uses the experimental power spectrum but assumes flat spectral phase after the pulse shaper. Generated pulses have de-convolved FWHM duration of 2.76 ps (using a de-convolution factor of 1.43 appropriate for our super-Gaussian apodization function) and time periodicity T=111 ps. Although the central portions of the curves match well, we observe discrepancies in the wings which we attribute to phase errors in this experiment. In another experiment, the second phase modulator in Fig. 2.1 is replaced with an intensity modulator with similar specifications. The generated frequency comb is comparable to that shown in Fig. 2.2(b). Autocorrelation traces of the compressed pulses obtained after phase correction are shown in Fig. 2.2(d). Here the phase corrections are determined by maximizing the second harmonic generation (SHG) yield at zero delay position while adding one spectral line at a time. In this case, although the de-convolved FWHM duration is the same (2.76 ps), the agreement between the experimental (dotted) and theoretical (solid) autocorrelation, the latter again calculated assuming no phase errors, is improved.

The 2.76ps pulse train obtained in Fig. 2.2(c) is sent to a 2 km dispersion decreasing fiber (DDF) soliton compressor (Pritel FP-400). Figure 2.3(a) shows the autocorrelation of the compressed pulse train with a repetition rate of 111 ps (9 GHz). A magnified view of the compressed pulse is shown in the inset, indicating a FWHM of 324 fs (assuming sech^2). Figure 2.3(b) depicts the compressed spectrum, indicating stable frequency comb generation with over 100 lines within 12 dB of the peak. Zoomed-in views for the compressed comb of Fig. 2.3(b) are shown in Fig. 2.3(c) (circle) and Fig. 2.3(d) (rectangle). Fig. 2.3(c-d) reveals excellent comb structure and quality after soliton compression even in the spectrally broadened regions. We compared the widths of the individual comb lines against OSA measurements of the initial CW line-width and observed no broadening of individual lines, even to the very edges of the spectrum (limited by the OSA resolution).

Inspection of the compressed comb profile reveals that the pulse is well off from ideal solitons. This is a typical behavior of DDF compression since the dispersion decreasing length is still considered short for a true adiabatic process. Further examination at the compressed pulse quality is presented in Fig. 2.4, with the intensity autocorrelation trace plotted in logarithm. The pulse pedestal suppressions achieved are greater than 20 dB throughout the entire temporal period. However, for real telecommunication applications such as optical code-division multiple access (O-CDMA), an even higher pedestal suppression ratio is desired.

2.3 Pulse pedestal cleaning using nonlinear optical loop mirror

According to the discussion made in the end of the previous section, suppression ratio of the pulse-peak to pedestal intensity plays an important role for real applications. It is essential that a higher suppression ratio be achieved as compared to the current value (~20 dB). Nonlinear optical loop mirrors (NOLM) are well developed device for ultrafast optical pulse processing [18,19]. Soliton propagation and nonlinear filtering effect of a NOLM has been theoretically described in detail [20]. Pedestal cleaning of DDF compressed pulses have been demonstrated to give roughly 20 dB improvement [21-23].

Figure 2.5 shows the proposed NOLM configuration for pulse pedestal cleaning. The ~300 fs solitons from the DDF compressor are sent to the input of the NOLM. The NOLM is comprised of a 2x2 optical coupler (OC, ports labeled 1 through 4), with power coupling ration of α and $(1-\alpha)$ for ports 3 and 4, respectively. The working principle of a NOLM is to obtain different accumulated nonlinear phase (from self-phase modulation, SPM) between the clockwise (E_c) and the counter-clockwise (E_{cc}) pulses by attenuating E_{cc} with optical loss G_L. A polarization controller (PC) is usually required for optimum matching of the two pulse polarizations. In order to obtain a larger nonlinear phase accumulation in a shorter fiber length, we intend to employ highly-nonlinear fiber (HNLF).

The main HNLF parameters of particular concern are its nonlinearity coefficient (γ), dispersion value (D) and the length (L). To determine the proper values of {D, L}, we perform numerical simulation using split-step Fourier (SSF) method in solving the nonlinear Schrödinger equation (NSE) for soliton propagation within the NOLM [24] with a design target aiming for greater than 20 dB pedestal suppression improvement:

$$\frac{\partial A}{\partial z}+\frac{\alpha}{2}A+\frac{i}{2}\beta_2\frac{\partial^2 A}{\partial T^2}-\frac{\beta_3}{6}\frac{\partial^3 A}{\partial T^3}=i\gamma[|A|^2A+\frac{2i}{\omega_0}\frac{\partial(|A|^2A)}{\partial T}-T_RA\frac{\partial(|A|^2)}{\partial T}] \quad (2.1)$$

where A is the temporal electric field amplitude of the pulse, α is the optical loss of the fiber, β_2 is the second-order dispersion, β_3 is the third-order dispersion. Table 2.1 lists the optical parameter values of our commercially available HNLF (OFS Denmark) used in carrying out the simulations. The terms on the right-hand side of the equation account for self-phase modulation (SPM), self-steepening, and stimulated Raman scattering, respectively.

Within the simulations, input pulse to the NOLM is obtained from experimental spectrum as shown in Fig. 2.3(b) while assuming flat phase. An input averaged power of P_{avg} = 17 dBm (experimental value), arriving at a peak power of 10.8 W for the 300fs input. The NOLM is comprised of 50/50 (α=0.5) optical coupler with G_L= -1 dB, and a 100 m HNLF with normal dispersion value of D= 1.0 ps/nm/km is assumed. Figure 2.6(a) shows the resulting normalized input and output pulse in log scale, indicating greater than 20 dB additional pedestal pulse suppression. Figure 2.6(b) shows the normalized input and output spectrum in linear scale. Note the output spectrum has a smoothened profile, resulting in a better pulse quality. The expected loss for this case is calculated to be around 3.6 dB. Coupling ration other than 50/50 degrades the pedestal suppression. For optical power tolerance analysis, various combination of {P_{avg}, D, L} values are assessed through simulation.

We now show experimental pulse pedestal energy suppression using 10 GHz repetition rate optical pulse train. The comb generation setup is identical to as described in Fig. 2.1, but with RF drive frequency tuned to 10 GHz. Fig. 2.7(a) shows the 10 GHz comb spectrum after the DDF. Fig. 2.7(b) shows the intensity autocorrelation trace of the DDF pulses, showing the 315 fs de-convoluted pulses with evident pedestal structure at delays of +/- 10 ps, and pedestal suppression of roughly 23 dB. The NOLM is constructed as pictured in Fig. 2.5, a 150m highly-nonlinear fiber (OFS Denmark) with a dispersion value D=0.7 ps/nm/km and the rest optical parameters listed in Table 2.1 is employed. Fig. 2.7(c) shows the output comb spectrum after the NOLM, where a much smoother comb is obtained as compared to the DDF comb (Fig. 2.7(a)), and pedestal cleaning can be thus anticipated. Indeed, Fig. 2.7(d) shows the intensity autocorrelation trace of the pulses directly after the NOLM, revealing pedestal suppression of greater than 32 dB. This value should be limited by the electrical noise of the lock-in amplifier. Ideally, 200 fs pulses can be obtained after the NOLM, however, the 1 ps de-convoluted pulse-width in Fig. 2.7(d) is a result of the residual dispersion of arising from the pulse propagation within the NOLM. A coarse resolution shaper is used to correct the quadratic spectral phase and the resulting intensity autocorrelation trace of the dispersion compensated, pedestal cleaned pulses is shown in Fig. 2.7(e), where a de-convoluted pulse width of 400 fs and better than 30 dB pedestal suppression ratio is obtained. The pulse width is limited by the bandwidth of the coarse resolution shaper.

The intensity autocorrelation traces of the NOLM output pulses seem very promising for practical usage. Comb/pulse quality of the NOLM output will be examined using differential binary phase shift keying decoding process in Chapter 4.

2.4 5 GHz optical arbitrary waveform generation using more than 100 lines[1]

Previous pulse shapers operated in the group-of-lines regime, which yields waveform bursts that are isolated in time. For true optical arbitrary waveform generation (O-AWG), the phases and intensities of individual spectral lines should be controlled, which leads to waveforms spanning the full time period between mode-locked pulses. Recently, line-by-line pulse shaping at ~10 GHz line spacing has been demonstrated in a free-space apparatus [8,9]; however, only a small number of spectral lines (~5) was fully controlled for O-AWG [8]. Line-by-line shaping in integrated planar lightwave circuit technology has also recently been reported at line spacings from 10 to 40 GHz; however, the number of lines remains small (10-20) while waveform fidelity is compromised due to phase errors and crosstalk [16]. Moreover, the number of lines controlled by these devices is limited by their free spectral range, and it is difficult to extend device resolution to below 10 GHz. Since the number of lines determines the degrees of freedom available for O-AWG, scaling to larger number of spectral lines is highly desirable. In this section we use a free-space platform to scale high resolution, line-by-line pulse shaping to obtain independent programmable control of greater than 100 lines at 5 GHz line spacing, while maintaining excellent waveform fidelity.

Figure 2.8(a) shows our experimental setup [25], the PMCW comb generator is similar to what is shown in Fig. 2.1, but now with the second modulator driven with a 5 GHz cosine waveforms. The modulator driven at 5 GHz determines the comb spacing

---

[1] Performed under extensive collaboration with Dr. Zhi Jiang.

and temporal periodicity. The resulting comb is manipulated by spectral line-by-line pulse shaper #1 to convert the broadband constant intensity waveform to a pulse train. Our experiments are the first to resolve comb lines spaced by only 5 GHz in a pulse shaping apparatus.

Figure 2.8(b) shows the measured spectrum after shaper #1; the discrete lines making up the spectrum are clear in the inset. Figure 2.8(c) shows the discrete spectral phases applied by shaper #1 onto the individual lines, in order to convert the phase-modulated but constant intensity field into bandwidth-limited 2.4 ps (FWHM) pulses (intensity autocorrelation shown in Fig. 2.8(d)). Although not yet illustrating true O-AWG, such high rate pulse generation starting from a CW source is already a powerful application of line-by-line pulse shaping [6]. The 2.4 ps pulses are then amplified by a fiber amplifier and directed into a dispersion decreasing fiber (DDF) soliton compressor. The interplay of self-phase modulation and dispersion in the DDF yield pulse compression to durations as short as 270 fs (Fig. 2.8(e)). Pulse compression is accompanied by strong spectral broadening. Figure 2.9 shows the spectrum after DDF compression obtained with slightly higher optical power coupled into the DDF. Over 1000 lines are generated between 1525 nm and 1565 nm.

Such a comb, created from a single CW laser, is highly useful for line-by-line pulse shaping studies. In our following O-AWG demonstrations we use a second line-by-line pulse shaper following the DDF (see Fig. 2.8(a)) to select and individually manipulate a set of 108 lines centered around 1537.5 nm and spanning 540 GHz bandwidth. The spectrum is shown in Fig. 2.10(a). An intensity cross-correlation measurement of the resulting pulse train, demonstrating transform-limited 1.65 ps pulses at 5 GHz repetition rate, is also shown. In this and subsequent measurements, temporal intensity waveforms are obtained via cross-correlation with high quality, pedestal-free, 1.02 ps reference pulses. Figure 2.10(b) demonstrates a simple example of line-by-line intensity control, where the LCM is programmed to block every other comb line. The resultant doubling of the comb spacing leads in the time domain to a doubling of the pulse repetition rate to 10 GHz.

We demonstrate the capability of line-by-line phase control for O-AWG by exploiting the relation $\tau(\omega) = -\dfrac{\partial \Psi(\omega)}{\partial \omega}$, where $\tau(\omega)$ and $\Psi(\omega)$ are the frequency-dependent delay and spectral phase, respectively. In the simplest case we apply linear spectral phase, which results in pure delay as shown in Figure 2.11. Notice that the delay is scanned across the whole repetition period T (200 ps), which is only possible when individual spectral comb lines are independently manipulated. The waveforms remain clean, with only very small satellite pulses. This is further evidence that we are in the line-by-line regime. In the group-of-lines regime, a strongly stepped masking function gives rise to significant satellite pulses, with satellite intensity becoming equal to main pulse intensity at phase steps of π per pixel.

Figure 2.12 shows examples of O-AWG with very complex waveforms: each pulse is split into two pulses per period, one of which is delayed and the other of which has cubic spectral phase. Each pulse corresponds to one half of the spectrum. Figure 2.12(a) shows such an example with the two pulses still non-overlapping. The cubic spectral phase corresponding to quadratic frequency-dependent delay yields a strongly oscillatory tail in the time domain. Figure 2.12(b) shows an example with larger cubic spectral phase. Here the waveform oscillations span the whole period with 100% duty cycle, which is one of the hallmarks of line-by-line pulse shaping. To confirm O-AWG fidelity, the calculated intensity cross-correlations are also shown for comparison. The agreement is excellent everywhere, even in the lowest intensity oscillations. Figures 2.12(c) and 2.12(d) show the unwrapped and wrapped discrete spectral phases applied to the 108 lines by shaper #2 in order to generate waveform Fig. 2.12(b). The linear and cubic spectral phases are clearly visible on respective halves of the spectrum. At some locations the phase change per pixel is π or more – again a hallmark of operation in the line-by-line regime.

In summary, we demonstrate 9 GHz, 2.76 ps pulse generation using spectral line-by-line processing of a greater than 40 spectral line frequency comb derived from a phase-modulated CW laser. The pulses have comparable pulse width with harmonically mode-locked lasers at similar repetition rate, but with simplified control, easy spectral tunability and excellent spectral stability. The generated pulses are further compressed to 324 fs by soliton compression. We also used 10 GHz comb generator to experimentally demonstrate pulse pedestal suppression of greater than 30 dB using a 150m highly nonlinear fiber to construct a nonlinear optical loop mirror. We also demonstrate 5 GHz line-by-line shaping using more than 100 lines for the first time. High fidelity time-domain waveforms are generated with high levels of feature complexities.

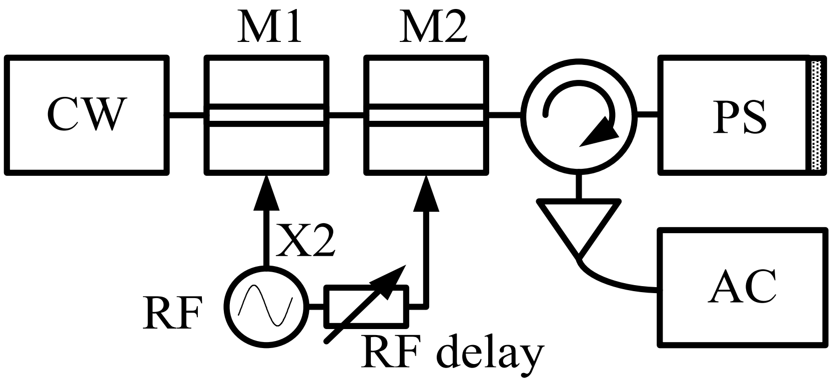

Fig. 2.1. Schematic of experimental setup. PS: reflective line-by-line pulse shaper; AC: autocorrelator; M1: low V_π phase modulator; M2: a phase or intensity modulator.

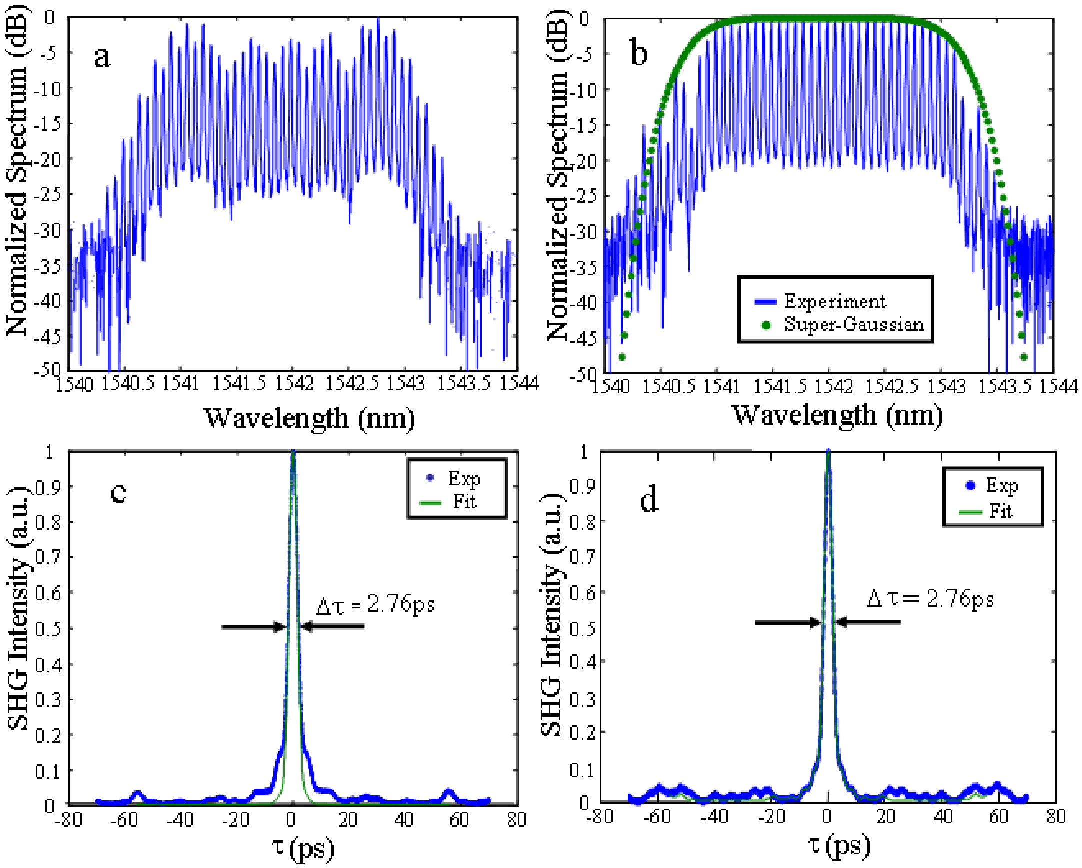

Fig. 2.2. Frequency comb and generated pulses. (a) Frequency comb without line-by-line control. (b) Intensity equalized and phase corrected frequency comb (solid); designed super-Gaussian apodization function (dot). (c) Autocorrelation trace (dotted: experimental; solid: calculated from frequency comb) of phase corrected output pulse, using two-line-beating phase measurement. (d) Autocorrelation trace (dotted: experimental; solid: calculated from frequency comb) of phase corrected output pulse, with phase adjusted to maximize SHG yield.

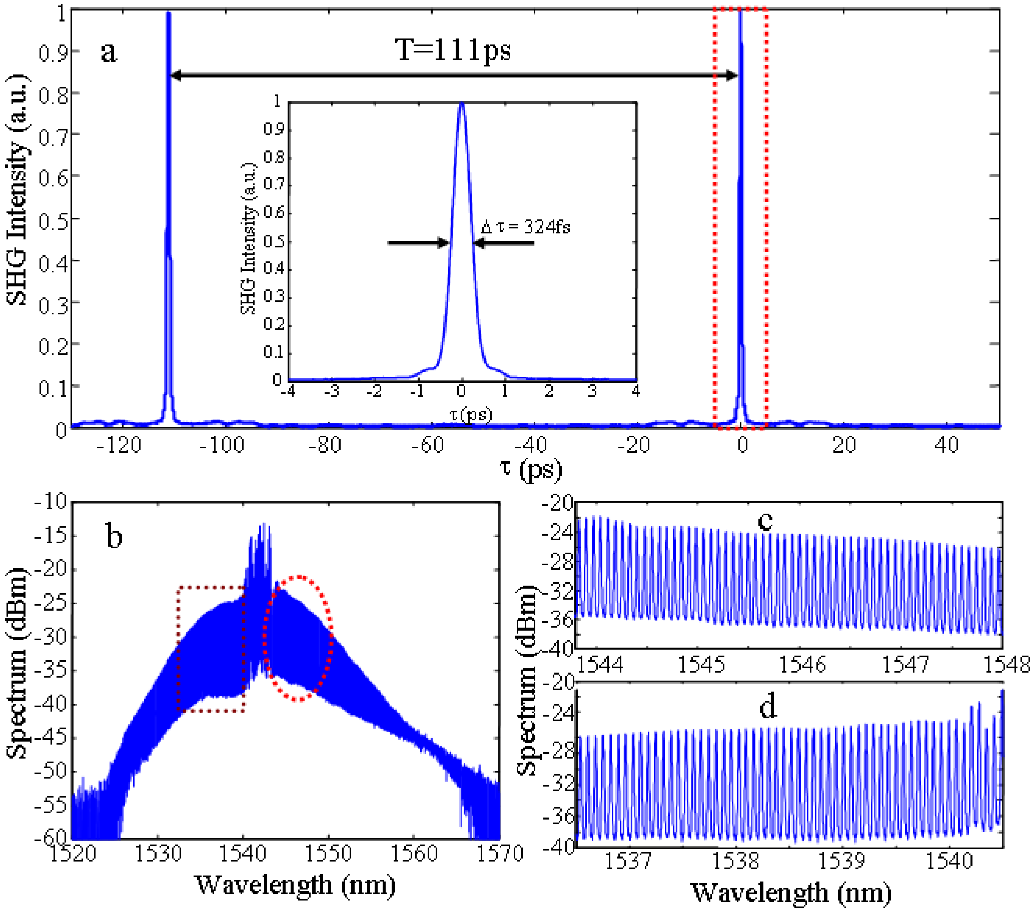

Fig. 2.3. Compressed pulses and frequency comb. (a) Autocorrelation showing the pulse train; the inset is zoomed in on a single pulse. (b) Frequency comb after soliton compression. (c) Zoomed-in view of the circle portion of (b). (d) Zoomed-in view of the rectangular portion of (b).

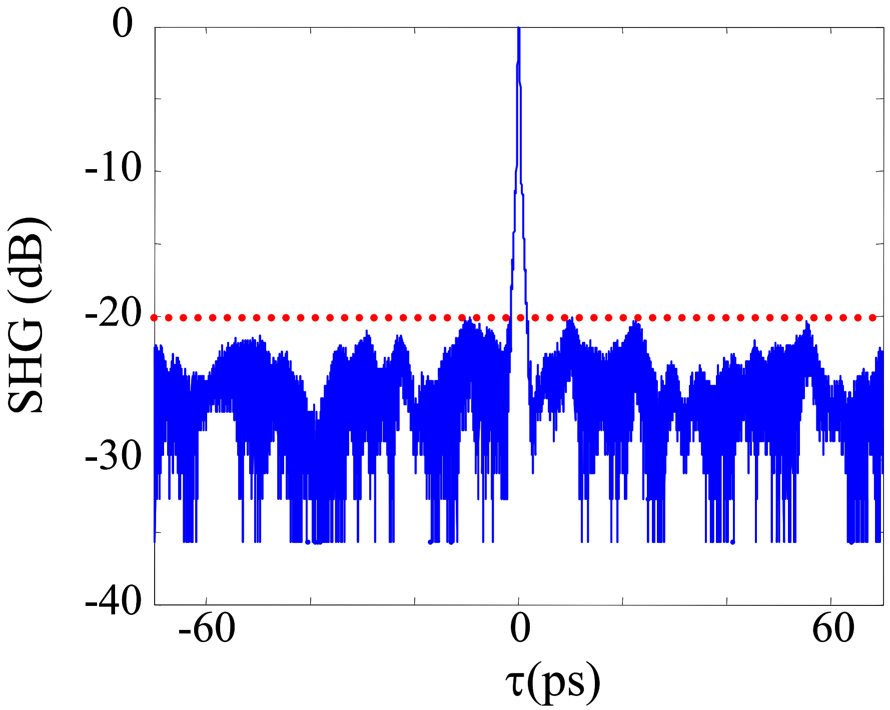

Fig. 2.4. Pulse quality inspection: autocorrelation of the compressed pulse in log scale.

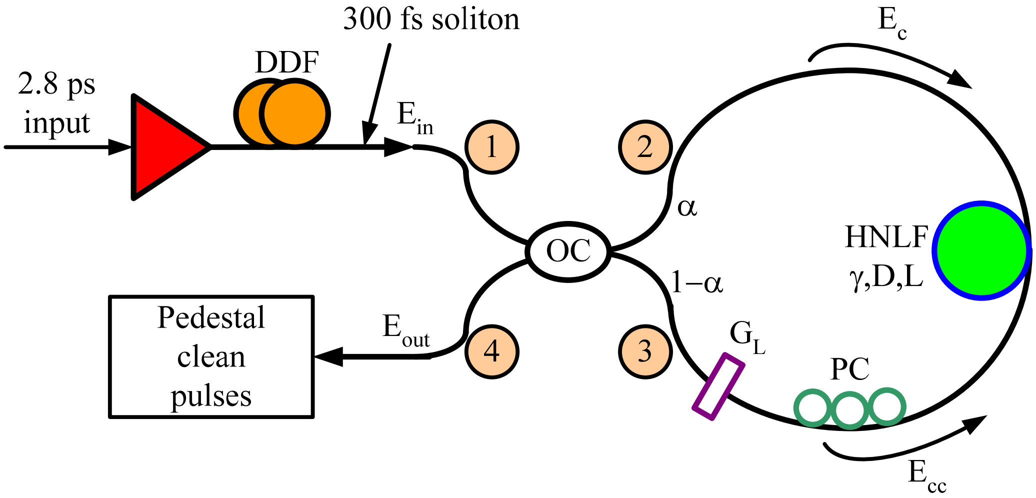

Fig. 2.5. NOLM configuration for pedestal cleaning. DDF: dispersion decreasing fiber; OC: optical coupler; α: power coupling ration of the OC; G_L: lumped optical loss element; PC: polarization controller; HNLF: highly-nonlinear fiber. γ, D, L are the nonlinear coefficient, dispersion value and length of HNLF, respectively.

Table 2.1. Optical parameters of OFS HNLF.

Cutoff wavelength (nm)	<1200±100	
Mode field diameter (mm)	3.9±0.2	
Nonlinear coefficient γ (/W/km)	10.5	
Attenuation (dB/km)	≤0.9	
Dispersion (ps/nm/km)	[-4~4] ±0.25	Determine through simulation
Dispersion slope (ps/nm2/km)	0.019±0.004	
PMD (ps/√km)	≤0.2	
Splicing loss (dB)	≤0.3	

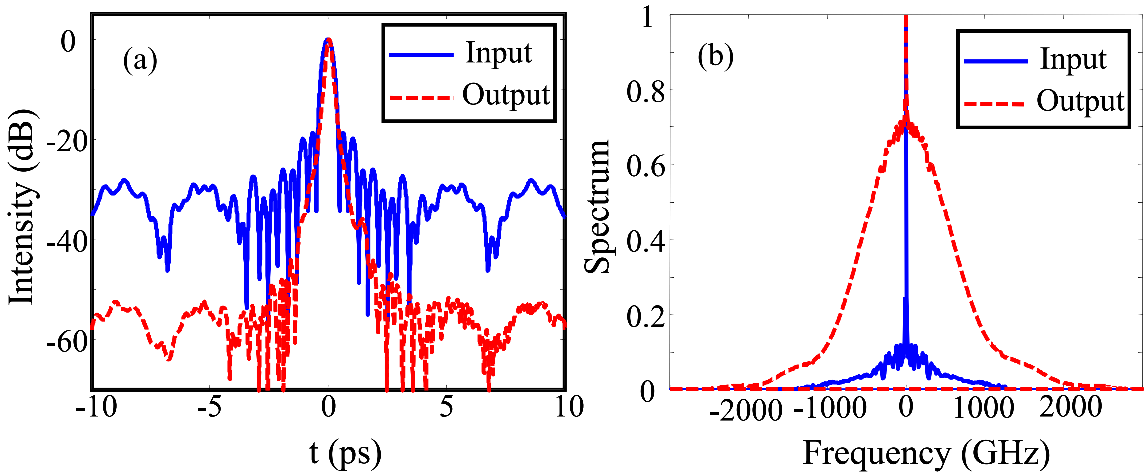

Fig. 2.6. (a) Simulated normalized input and output pulse of the NOLM in log scale. (b) Simulated normalized input and output spectrum of the NOLM in linear scale.

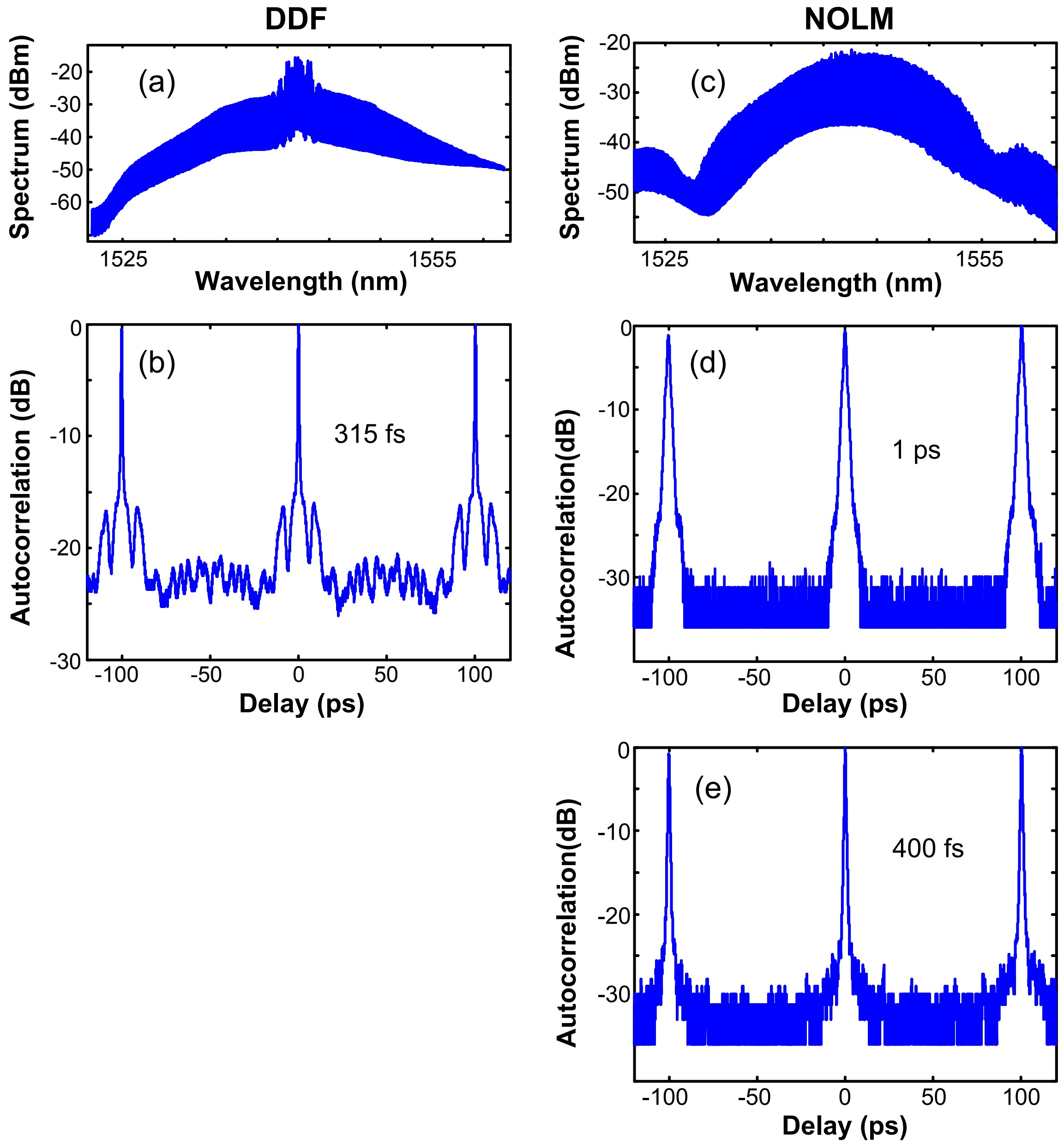

Fig. 2.7. (a,c) Experimental 10-GHz comb spectra after the DDF and NOLM. (b,d,e) Intensity autocorrelation traces of the pulses after DDF, directly after NOLM and after NOLM and with dispersion compensation, in log scale.

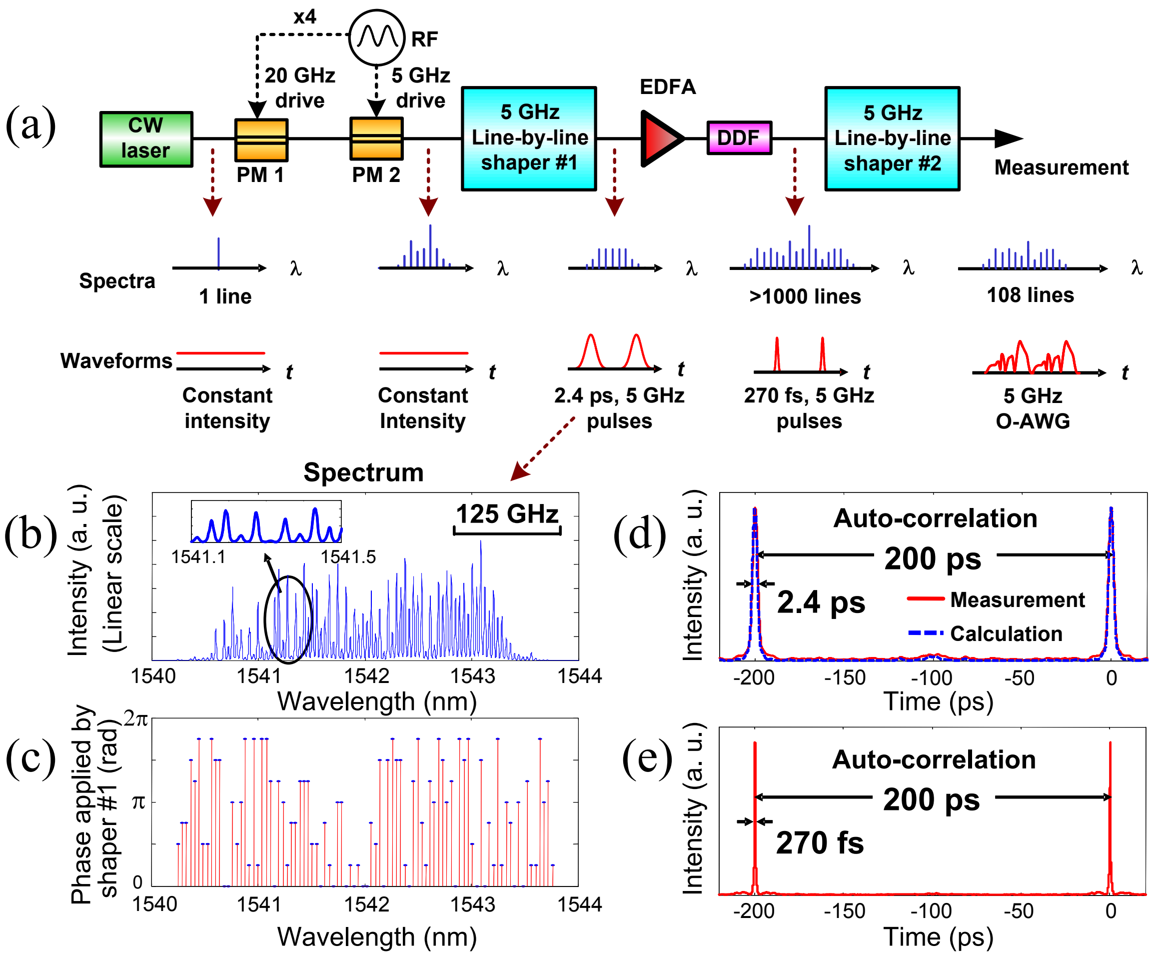

Figure 2.8. (a) Schematic diagram. (b) Spectrum (in linear scale) after shaper #1 with partial spectral intensity equalization to remove large spectral spikes. The discrete line feature of the spectrum is clear in the inset figure. (c) Spectral phases applied by shaper #1. (d) Pulse intensity auto-correlation after shaper #1. The theoretical auto-correlation, calculated using the measured power spectrum and assuming flat spectral phase, is also shown for comparison. (e) Pulse intensity auto-correlation after DDF with 20.4 dBm optical power at DDF input. CW: Continuous wave. PM: Phase modulator. RF: radio frequency. EDFA: Erbium doped fiber amplifier. DDF: Dispersion decreasing fiber. O-AWG: optical arbitrary waveform generation.

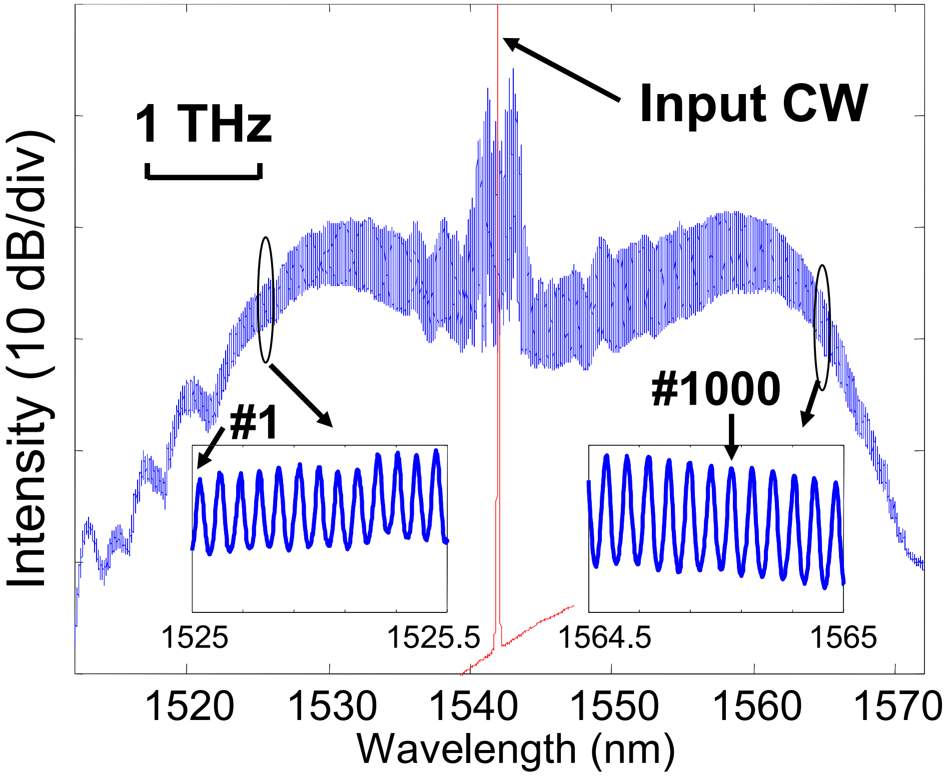

Figure 2.9. Generation of over 1000 stable spectral lines starting from 1 single line. Input CW (1 single line) is also shown for comparison. 22.0 dBm optical power at DDF input, showing over 1000 lines between 1525 nm and 1565 nm. The spectral intensity dynamic range for 1000 lines are 20 dB.

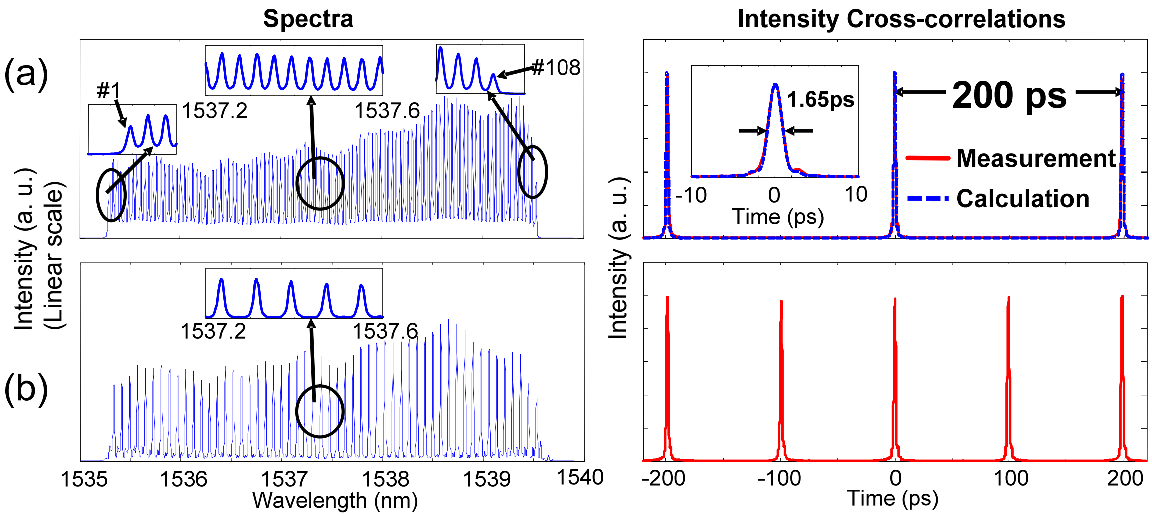

Figure 2.10. Spectral line-by-line shaping of 108 lines: spectral intensity control. (a) spectrum (linear scale) and intensity cross-correlation for the selected 108 lines. 20.4 dBm optical power at DDF input. Calculated intensity cross-correlation for transform limited pulses (using measured spectrum and assuming zero spectral phases) is also shown for comparison, which agrees very well to the measured cross-correlation. This confirms that the pulses are transform-limited. (b) Spectrum and intensity cross-correlation by blocking every other line.

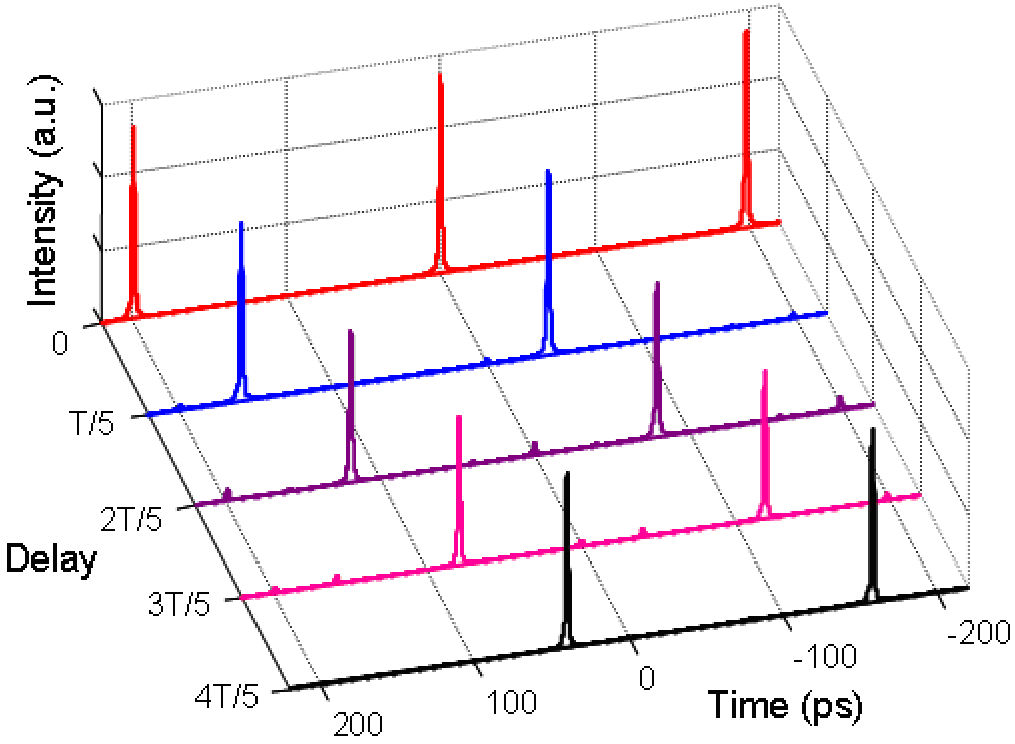

Figure 2.11. Spectral line-by-line shaping of 108 lines: spectral phase control. In a series of experiments, the pulse shaper applies various linear spectral phase ramps, resulting in delays proportional to the slope of the applied phase ramp. Intensity cross-correlation measurements are plotted for pulse trains delayed by 0, T/5, 2T/5, 3T/5 and 4T/5, by applying phase changes of 0, 2π/5, 4π/5, 6π/5, and 8π/5 per pixel, respectively. Notice that the delay is scanned across the whole repetition period T (200 ps), which is only possible when the individual spectral comb lines are independently manipulated.

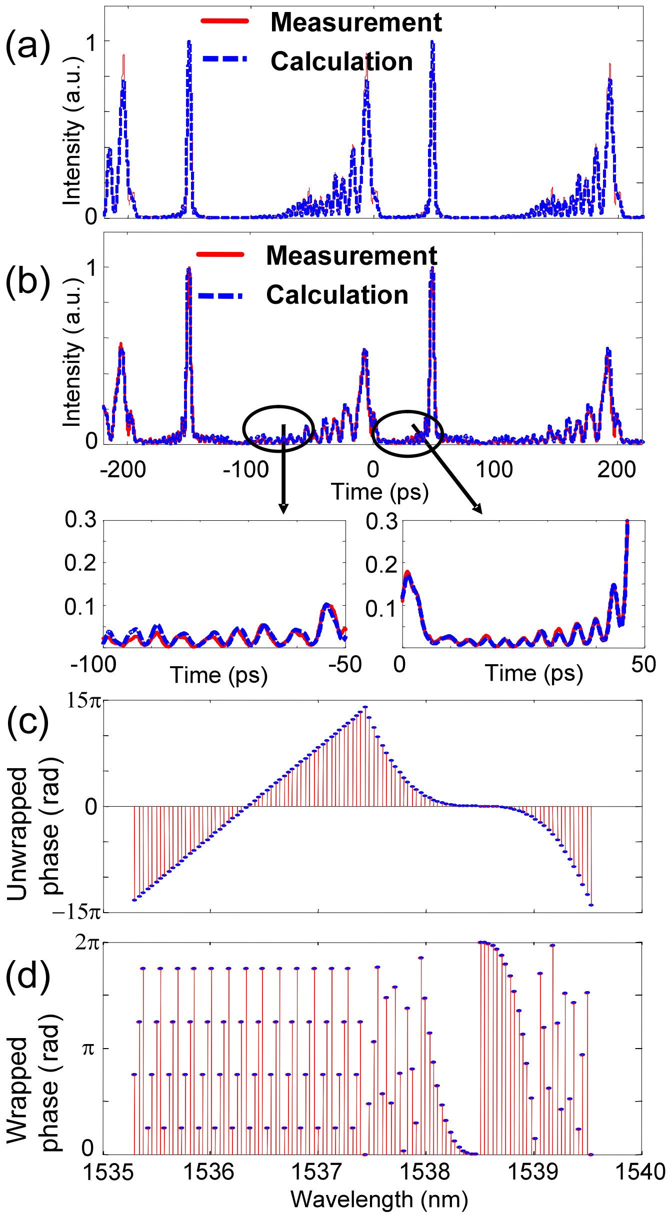

Figure 2.12 Line-by-line shaping of 108 lines: complex O-AWG. (a) The intensity cross-correlation shows an example of O-AWG with very complex waveform: each pulse is split into two pulses per period, one of which is delayed and the other of which has cubic spectral phase. Each pulse corresponds to one half of the spectrum. The two pulses are still temporally separated. (b) Similar to (a) but with a larger cubic phase on one pulse. Features of the two pulses now begin to merge; such temporal overlap is a hallmark of line-by-line shaping. The agreement between measurement and calculation for both (a) and (b) shows the high fidelity achieved in these O-AWG experiments. Red solid line: measured intensity cross-correlation. Blue dashed line: calculated intensity cross-correlation. (c) The unwrapped spectral phases applied to shaper #2 for waveform (b). (d) The wrapped spectral phases applied to shaper #2 for waveform (b).

3. TIME-MULTIPLEXED PHOTONICALLY ENABLED RADIO-FREQUENCY ARBITRARY WAVEFORM GENERATION WITH 100 PS TRANSITIONS

In this chapter we demonstrate, to our best knowledge, the fastest programmable arbitrary radio-frequency (RF) waveform enabled by integrating fast wavelength switching, phase-modulated laser frequency comb generation, and line-by-line shaping [26].

3.1 Introduction

Fourier-Transform (FT) based optical pulse shaping is a frequently adopted technique that has facilitated numerous applications [7]. Conventionally, a liquid crystal modulator (LCM) is placed on the Fourier-plane of the shaper to allow flexible amplitude and phase manipulation of the input source spectral components. The waveform update rate is limited by the response time of the LCM, typically tens of milliseconds. Recently, there have been several reported efforts to increase the waveform update rate, with results demonstrated up to 33 MHz [27-29]. However, due to limited spectral resolution, groups rather than individual spectral lines have been manipulated in these works.

Recently, by utilizing optical pulse shaping and gigahertz-period optical frequency combs together, quasi-static (~ 10 ms update time) spectral line-by-line pulse shaping examples have been demonstrated [9,25,30]. In line-by-line shaping, the amplitude and phase of discrete spectral comb lines are independently controlled. A LCM based FT shaper has been reported to generate optical arbitrary waveforms using more than 100 spectral lines at 5 GHz comb spacing [25]. A hyperfine wavelength de-multiplexer with subsequent electro-optical modulators have been reported with a waveform modulation rate ranging from tens to hundreds of MHz, but only two spectral lines were controlled [31-33]. In a previous demonstration, our group reported switching between two optical waveforms at 10 GHz in the group-of-lines shaping regime; however, each waveform required a separate shaper [34]. Here we report a novel scheme where distinct waveforms can be generated at high update speed using a single pulse shaper.

Photonically assisted radio frequency arbitrary waveform generation (RF-AWG) [35] is a promising application of pulse shaping that has been demonstrated previously at low pulse shaping resolution and with low update rate [36,37]. In this Chapter, we overcome the limitation of the LCM response time and report a simple structure which allows RF-AWG waveform updates in less than 100 ps (10 GHz), to our knowledge the fastest reported to date [38].

3.2 Principle and experimental results

The schematic of our proposed novel time-multiplexed setup is shown in Fig. 3.1. Two CW lasers (λ_a, λ_b) with a $LiNbO_3$ intensity modulator (IM) after each laser are used to provide rapid wavelength switching. IM1 (for λ_a) and IM2 (for λ_b) are driven by the programmable data port (Q) and inverted data port ($\overline{Q}$) of a bit-error-ratio test set (BERT) with bit duration of 100 ps (10 GHz signal), respectively. The wavelength switched CW outputs are combined via an optical coupler (node (i)) and sent to an optical frequency comb generator comprised of a lithium niobate phase modulator (PM) driven at a repetition frequency of f_{rep}=10 GHz by the clock of the BERT (node (ii)). These phase-modulated CW (PMCW) combs [13,25] are manipulated by a FT shaper where distinct waveforms are generated for each different input center wavelengths (node (iii), $I_a(t)$ and $I_b(t)$).

In order to enable high-speed waveform updates, the LCM pixels are logically divided into different regions, each of which may be programmed to generate different waveforms; each region may be selected by rapidly changing the input wavelength. An optical amplifier is used after the shaper and the rapid-updated waveforms are detected using a 50 GHz bandwidth sampling scope/photodiode. An optical spectrum analyzer (OSA) with 0.01 nm resolution is used to measure the comb spectra.

In order to more clearly explain the concept, first consider the use of only one CW laser. Figure 3.2(a) shows the λ_b PMCW comb (line {0} denotes the CW input). The spectral lines that have a π-phase difference are labeled within the figure. Note that without phase correction, the time-domain output intensity of the PMCW comb is still CW in nature. In our experiments, lines {-3~2} are selected by the line-by-line shaper to demonstrate shaped waveform updates so that the optical bandwidth does not exceed the electrical bandwidth of our sampling scope. Figure 3.2(b) shows the six-line PMCW combs when both CW lasers are turned on with λ_a=1540.95 nm and λ_b=1541.91 nm. As a first demonstration of shaped RF-AWG updates, Fig. 3.2(c) shows rapid waveform switching, in which a repetitive data pattern Q=[1111 0000] is fed to IM1. Here, two cosine waveforms (spectral lines $\{a_{-1}, a_0\}$ and $\{b_{-1}, b_0\}$ selected while others suppressed) are generated. The corresponding intensity waveforms $I_a(t)$ and $I_b(t)$ are labeled within the figure. The solid trace indicates the measured waveform when no optical phase control is applied, and I_a and I_b are identical cosine waveforms. Switching between I_a and I_b simply results in a continuous RF cosine signal shown in the figure (although transient effects are evident with a reduction in signal amplitude near the wavelength switching times). The dashed trace indicates the measured waveform when a π phase is applied to line $\{a_{-1}\}$ so that I_a is delayed by exactly half the period compared to I_b. This yields an RF waveform with abrupt π phase shifts inserted at times determined by the driving data. Figure 3.2(d) shows rapid switching of waveform frequencies. Here lines $\{a_{-1}, a_1\}$ are selected for the λ_a comb, resulting in a cosine waveform with repetition rate of $2f_{rep}$, while the λ_b comb is again filtered to yield a cosine waveform with repetition rate of f_{rep}. Rapid switching between the two waveforms is observed in direct correspondence to the data pattern. The update transition time is less than 100 ps, defined here by the data pattern frequency (10 GHz).

Fig. 3.3(a, b) show examples of RF-AWG using line-by-line phase control on the six-line combs. Here, a longer data pattern (length of 40) is used so that regions of the RF signals located away from the transition regions may be examined to check the fidelity of waveforms under quasi-static generation conditions. With a π phase applied to λ_a comb line {1}, transform-limited pulses are generated and measured in the sampling scope trace (dots) of Fig. 3.3(a), in excellent agreement with the calculated result (line). Figure 3.3(b) demonstrates pulse doublet generation by applying π phase to λ_b comb lines {-3, -2, -1 and 1}. The peak amplitude of the doublet pulse is faithfully lowered by a factor of two. In Fig. 3.3(c-e) we discuss the effect of data pattern length on the RF-AWG update using these two waveforms. In Fig. 3.3(c), we apply a repetitive 16-bit data pattern Q=[0000 111111111111] to IM1, defining the length of I_a. For I_a and I_b, slight amplitude variation is observed near the edges of the waveform transitions. We attribute this behavior to: (1) a non-ideal rectangular data pattern from the BERT (bandwidth of 13.5 GHz) due to finite rise (~20 ps) and fall (~65 ps) time; (2) finite optical intensity extinction ratio of the IM (~15 dB); and (3) pulse shaper frequency filtering effect. Inter-mixing of the two waveforms occurs during these intervals and may cause the observed amplitude modulation in the RF-AWG results.

In one extreme, one could envision the capability of a bit-by-bit (waveform-by-waveform) update function enabled by our scheme. Figures 3.3(d, e) compare the effects of gradually shortening the duration of each waveform using repetitive data patterns of Q=[000 11111] and Q=[11 00] to drive IM1. Waveform updates are apparent down to two-bits per waveform (Fig. 3.3(e)), but with larger amplitude variance within the waveforms due to the non-ideality of the drives discussed previously. In Fig. 3.3(d, e), λ_a comb lines are gradually attenuated using shaper amplitude control, lowering the bandwidth-limited pulse peaks of $I_a(t)$ as compared to Fig. 3.3(c), demonstrating another degree of freedom in waveform control.

Figure 3.4 demonstrates signals incorporating rapid triangular waveforms. These are obtained by applying a cubic spectral phase to a broader PMCW comb (using dual stage phase-modulation [6,25]) resulting in oscillatory tails, so that a triangular RF waveform is converted via the photo-detector. The resulting PMCW spectra are shown in Fig. 3.4(a), where 28 spectral lines (280 GHz bandwidth) are selected from each comb. The spectral line phases are corrected using an automated process, resulting in transform-limited pulses. On top of these phase corrections, a cubic spectral phase is applied to the λ_a comb, resulting in rapid updates between triangular and transform-limited pulses, shown in Fig. 3.4(b). Figure 3.4(c) shows the waveforms when the λ_b comb has an applied cubic phase of opposite sign to that of the λ_a comb, providing triangular pulse updates with opposite {fast, slow} edges. The slight ripples observed on the trailing edge of $I_b(t)$ are due to the detector impulse response. In these two examples, Q=[1111 0000] is used. To demonstrate flexibility of data patterning, Fig. 3.4(d) shows waveform updates using a repetitive 20-bit-length data pattern.

Our scheme has potential for significant scalability and extensibility. For example: (1) Waveforms of different repetition rates and bandwidths may be obtained through slight modification of the comb generator setup. (2) The bulk wavelength switching in our current scheme can be replaced by a monolithically integrated wavelength converter [38]. (3) Multiple waveforms can be controlled by switching among more CW wavelengths while incorporating a spatial light modulator with larger pixel count or in a two dimensional geometry [39]. (4) The waveform update rate can be increased by using a faster data pattern generator.

In summary, using a simple configuration, we demonstrate, to our best knowledge, the fastest reprogrammable RF arbitrary waveform generation ever reported. By combining 10-GHz wavelength switching, optical comb generation, and liquid crystal modulator based line-by-line pulse shaping, RF-waveforms are updated within 100 ps.

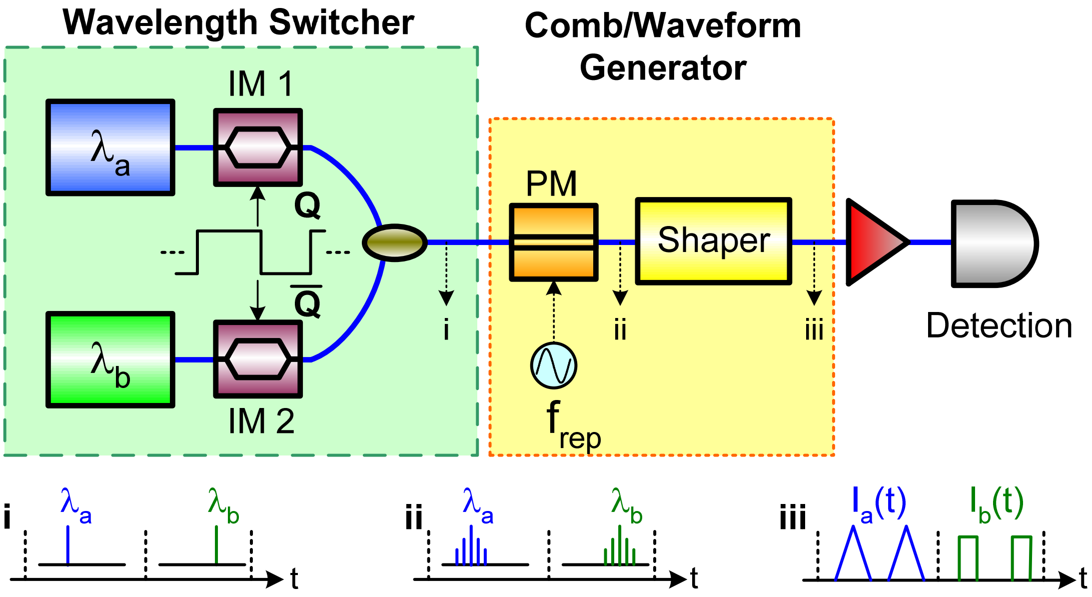

Fig. 3.1. Schematic of the experimental setup. (λ_a, λ_b): two CW lasers; IM: intensity modulator; Q: data pattern; PM: phase modulator; f_{rep}: comb frequency spacing.

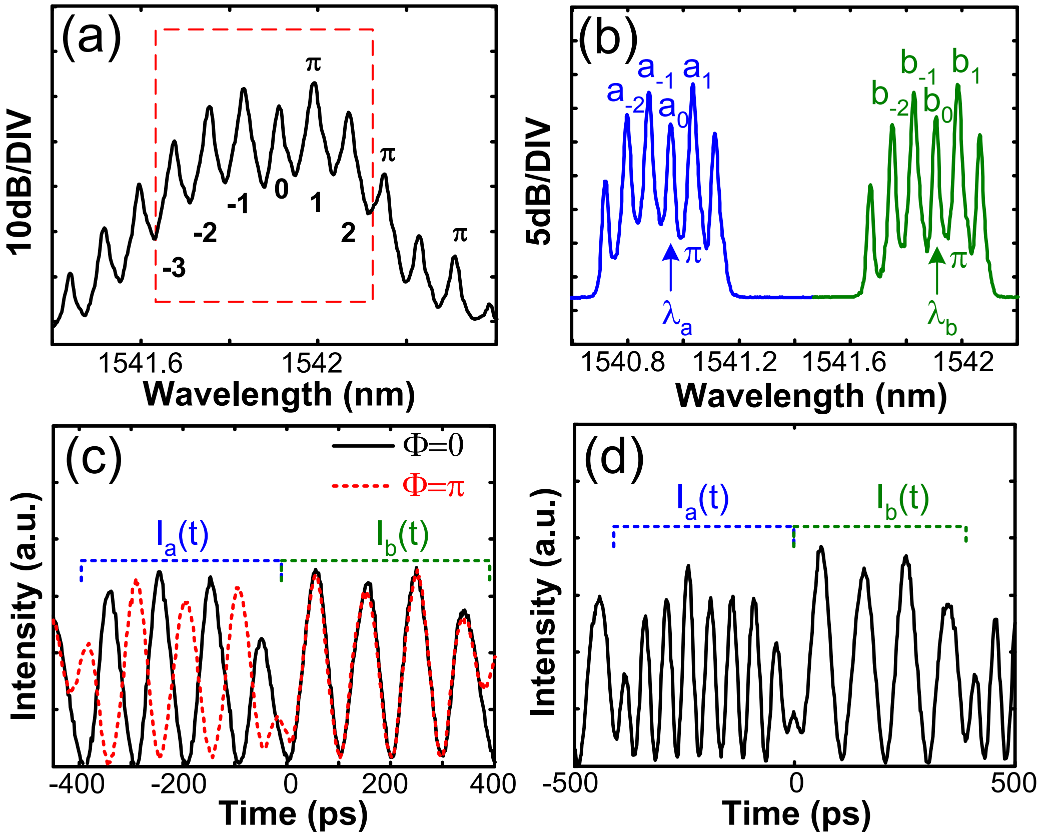

Fig. 3.2. (a) PMCW spectrum. Six lines within the rectangle are used for waveform generation. (b) Six-line selected PMCW combs when both CW lasers are on. (c, d) Sampling scope traces of rapid RF-AWG updates with Q=[1111 0000]. (c) Switching between waveform phase modulation using two spectral lines from each comb. (d) Switching between waveform frequencies.

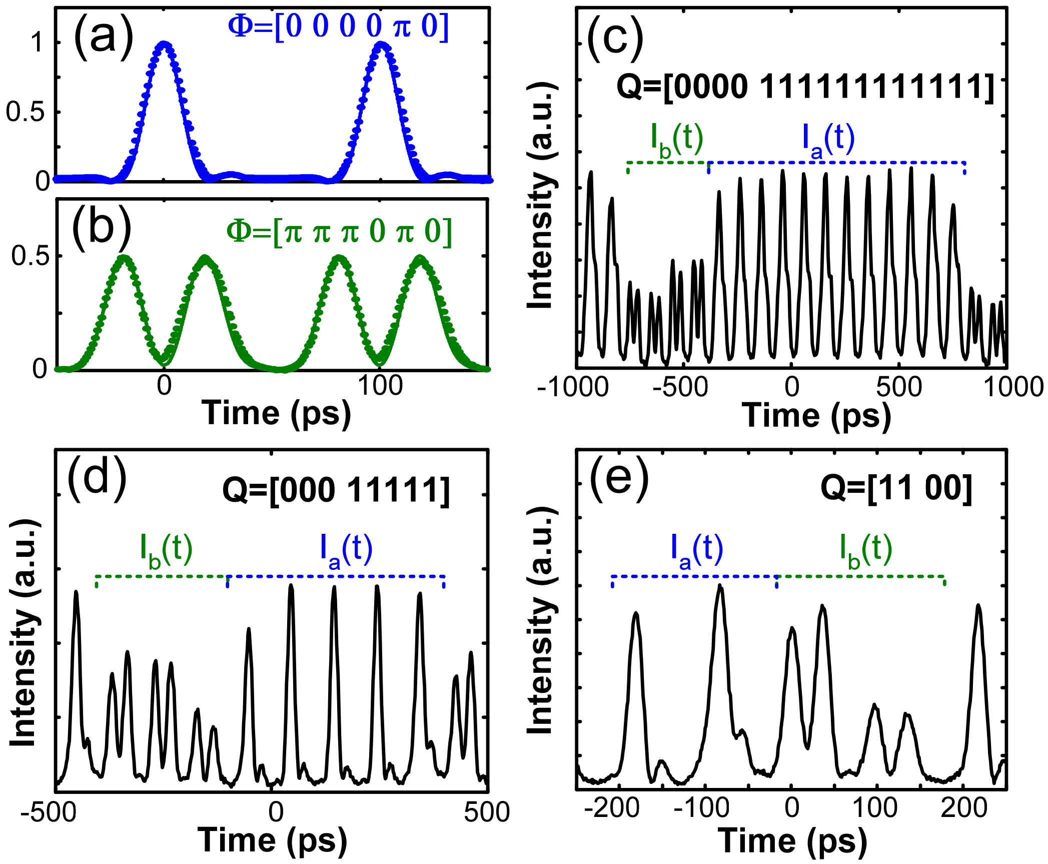

Fig. 3.3. Sampling scope traces of RF-AWG using six comb lines. (a) π-phase applied to λ_a comb line {1} for transform-limited pulses. (b) π-phase applied to λ_b comb lines {-3 to -1 and 1}, resulting in optical odd-pulses. (c-e) RF-AWG updates results. (c) Q=[0000 111111111111]. (d) Q=[000 11111]. (e) Q=[11 00].

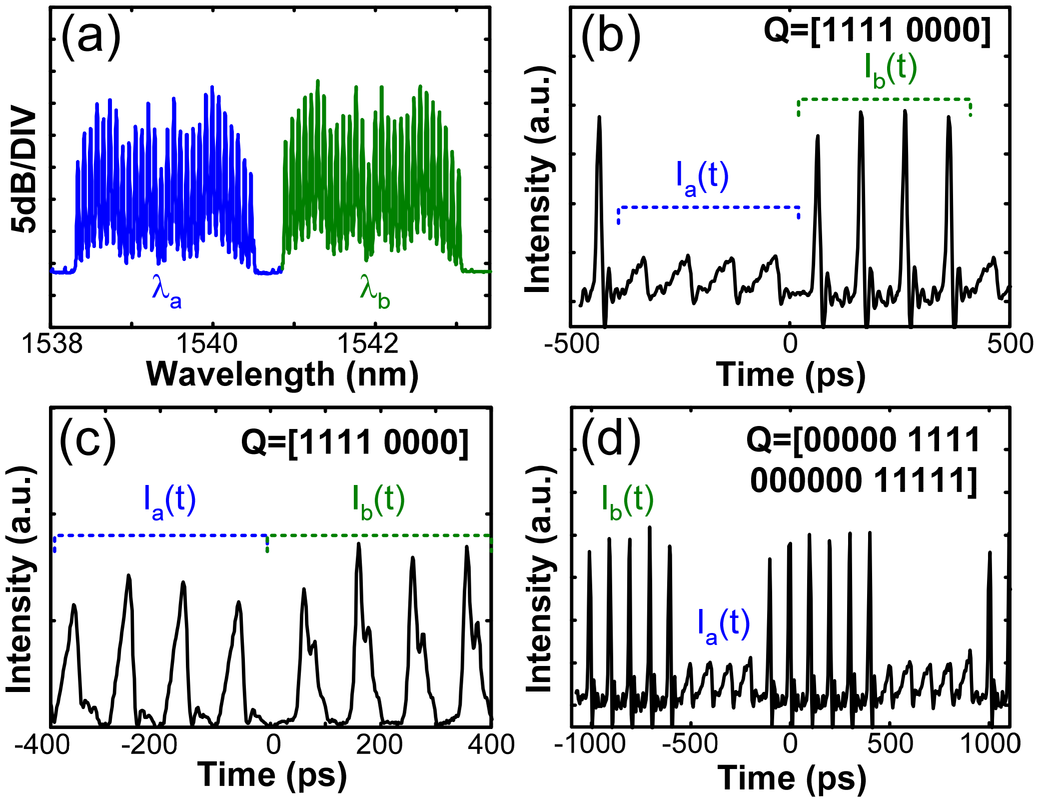

Fig. 3.4. (a) 28-line PMCW combs used for triangular RF waveforms. (b) Switching between triangular and transform-limited pulses. (c) Switching between triangular waves with opposite (fast, slow) trailing edges. (d) Waveform switching using a more complicated data pattern.

4. NONLINEARLY BROADENED PHASE-MODULATED CONTINUOUS-WAVE LASER FREQUENCY COMBS CHARACTERIZED USING DPSK DECODING

In this chapter, two nonlinearly broadened optical frequency combs are generated from phase-modulated continuous-wave (PMCW) laser seed pulses by using both normally and anomalous dispersive media. These broadened combs are characterized using DPSK decoding [40]. Our results point to combs spectrally broadened using normal dispersive fiber as a promising source for short pulse coherent communications.

4.1 Introduction

Coherent communications have been extensively studied in the 1980s and early 1990s in optical fiber communication systems [41,42]. Among various data encoding formats, differential-phase-shifted-keying (DPSK) is an optical phase-only data modulation format in which the optical phase changes between adjacent bits are used for data decoding [43,44]. Using balanced detection, DPSK has the advantage of a 3-dB lower optical signal-to-noise-ratio requirement as compared to the conventional ON-OFF-keying approach [44,45]. The 3-dB sensitivity advantage enables DPSK systems with longer fiber reach and with lower transmitted power, being less susceptible to fiber nonlinearities. Recently, interest in coherent ultrashort pulse communications (especially employing phase shift keying) has reemerged as a means for achieving extremely high bit-rate systems (ranging from a few hundreds of Gb/s to over 1Tb/s) over long fiber transfer links [46-48]. In such high rate demonstrations, the approach is to start with pulse generators at a base repetition rate (10~40Gbit/s) followed by subsequent optical time-domain multiplexing (OTDM) to obtain the multiplied transmission rate. As a result, it is crucial that the pulse sources provide stable repetition rate and wavelength, pulse-width significantly shorter than the multiplexed bit period, high pulse energy extinction ratio, and timing jitter much less than the pulse width. Careful characterizations of the pulse sources are thus required.

Conventionally, 10~40 GHz optical pulse trains have been derived from mode-locked lasers (therefore generating optical frequency combs, with comb lines spaced apart by the pulse repetition frequency). However, significant effort is needed to stabilize lasers with multi-GHz-mode-locked repetition rates typically achieved via harmonic mode-locking [49,50]. To obtain shorter pulses for Tb/s OTDM systems, ps-duration pulses directly obtained through mode-locked frequency combs are subsequently sent through nonlinear fiber propagation for spectral broadening. Such nonlinearly broadened combs have been widely explored [51-56]. Typically, comb properties have been characterized using spectral slicing followed by measurements on an electrical spectrum analyzer (ESA) [51,54 -56], on-off keying [52], or a scanning Fabry-Perot filter [51]. Such characterization techniques are sensitive predominantly to intensity noise and timing jitter. Phase conservation in the comb broadening process has been examined through binary phase encoding the time-multiplexed seed pulses which are decoded and characterized subsequent to nonlinear propagation [53]. Laser linewidth measurements using direct heterodyne beating or delayed self-{homodyne, heterodyne} are also well developed techniques [57].

More recently, much interest have been focused on optical frequency comb generation using externally-modulated continuous-wave lasers [12,13,58]. In contrast to harmonically mode-locked lasers, no frequency stabilization mechanisms are required for the externally-modulated scheme. This results in substantial flexibility for tuning line spacing, center wavelength, and optical bandwidth, which is useful for many applications [6,16,25,30,59].

In this chapter, we discuss 10-GHz pulse sources, potentially useful for short pulse coherent communications, generated using 2.5ps transform-limited phase-modulated continuous-wave (PMCW) seed pulses followed by subsequent nonlinear spectral broadening using either normal or anomalous dispersion fibers. The pulses spectrally broadened in normal dispersion fiber shows substantially better DPSK performance compared to the anomalous dispersion fiber. These differences are related to data obtained using other comb characterization methods, primarily those based on radio frequency spectrum analysis. Our results show that DPSK encoding/decoding is a useful addition to the suite of comb characterization tools, since comb coherence, intensity noise, and timing jitter are all accounted for in the DPSK decoding process.

4.2 Experimental setup

Figure 4.1(a) shows a schematic diagram of our experimental setup. PMCW seed pulses are sent to a nonlinear medium for spectral broadening. Two nonlinear media are considered within this chapter: (1) A commercially available dispersion decreasing fiber

(DDF) of 2 km for adiabatic soliton compression [60], with linearly decreasing dispersion values of 10 to 1.5 ps/nm/km from the input to the output. (2) A normal group velocity dispersion highly nonlinear fiber (HNLF) of 247 m, in which self-phase modulation is exploited as the broadening mechanism. The nonlinear coefficient of the HNLF is 10.5 $(\mathrm{W\ km})^{-1}$, the dispersion and the dispersion slope are -1.88 ps/nm/km and 0.016 $\mathrm{ps/nm^2/km}$ respectively. After the nonlinear media, a grating based shaper is used to perform spectral slicing of the broadened combs. The spectrally sliced pulses are temporally phase-encoded with $\{0 \text{ or } \pi\}$ using a pseudo-random bit stream of length $2^{23}-1$ by a lithium niobate phase-modulator. The DPSK decoder is a commercial Michelson interferometer implemented in micro-optics, with delay τ_0 tuned exactly equal to one period of the PMCW pulse train. The DPSK decoder is operated single-ended; a single output is sent to a photo-detector (7.5 GHz bandwidth), followed by a limiting amplifier and measured using a bit-error-rate (BER) test set.

The setup for generating the 2.52 ps transform-limited PMCW seed pulse train at repetition rate f_{rep}=9.953 GHz is illustrated in Fig. 4.1(b). A CW laser (Koheras Adjustik: 1542 nm) with 1 kHz linewidth is sent to a dual-modulation comb generator, where a low-V_π phase modulator is driven at $2f_{rep}$ to obtain a wider comb bandwidth, and a subsequent intensity modulator is driven at f_{rep} to fill in the f_{rep} comb lines. A Fourier-Transform based spectral line-by-line pulse shaper is used to correct the phases of each spectral line of the PMCW comb using an automated process [6,25]. The resulting comb spectrum and the intensity autocorrelation of the pulse are shown in Fig. 4.1(c, d), respectively. In Fig. 4.1(d), the calculated trace is obtained from Fig. 4.1(c) assuming a flat spectral phase, from which a de-convolved pulse duration of 2.52 ps is derived. The experimental trace coincides with the calculated trace, demonstrating high fidelity line-by-line phase shaping capability. A low noise erbium-doped fiber amplifier (EDFA 1) is used to amplify the signal after the pulse shaper to 12 dBm (input -18 dBm), and subsequently a high gain EDFA (EDFA 2, Pritel FP-400) with 20.5 dBm maximum output power is used after the line-by-line shaper followed by an optical band-pass filter with 4 nm bandwidth for elimination of optical amplified spontaneous noise (ASE).

For nonlinear processes, it is critical to acquire the knowledge about the optical signal to noise ratio (OSNR) of the seed comb. From Fig. 4.1(c), a rough estimate of 26 dB OSNR of our PMCW comb can be deduced directly by comparing the ratio of the comb line peak and the level between two lines. However, we believe this is an underestimated value limited by the OSA resolution of 1.25 GHz. The procedure in making a better estimation over the OSNR is shown in Fig. 4.2. To properly assess the

ASE noise level, Fig. 4.2(a) shows three optical spectra after the band-pass filter: when no comb (dotted, by blocking off the beams within the shaper), a 10 GHz PMCW comb (dashed) and a 20 GHz PMCW comb (solid, by turning the modulation signal driving the intensity modulator off) is output from the shaper and amplified by the two EDFAs, respectively. ASE noise levels for the three cases are plotted in Fig. 4.2(b) away from the combs (for example, at 1538.5 nm). It can be easily deduced that when a 10 GHz PMCW comb is transmitted through the shaper, the ASE noise level is suppressed by 4.8 dB, and 8.9 dB for the 20 GHz comb case due to the presence of larger input signal power.

To examine the limitation of the OSA resolution, Fig. 4.2(c) shows the 20 GHz comb (solid), ASE noise level (dotted, beams blocked within shaper), and the same ASE noise level (dotted), but artificially shifted down by 8.9 dB (dash-dotted) centered at 1542 nm. The small bumps showing at the comb spacing for the lower two curves are attributed to minute back-reflection of the comb power into and amplified by the EDFA. Even though now the comb spacing is increased to 20 GHz so the OSA can better resolve the lines, we can see that directly from the 20 GHz comb trace, the noise levels between two lines are still ~3 dB higher than the ASE level artificially shifted down according to the suppression obtained in Fig. 4.2(b). This confirms that the line-shape from the OSA trace is the main limiting factor for our OSNR reading in Fig. 4.1(c). For the 20 GHz comb, we estimate an OSNR of greater than 37 dB. Fig. 4.2(d) shows the 10 GHz comb (dashed), ASE noise level (dotted, no input), and ASE noise level artificially shifted down by 4.8 dB (dash-dotted). For our 10 GHz seed comb, the OSNR can therefore be deduce in two approaches: 34 dB by subtracting 4.1 dB off the OSNR obtained for the 20 GHz comb, or a greater than 30 dB OSNR by the ratio of the comb leaks to the shifted ASE as shown in Fig. 4.2(d). From this procedure, we have confirmed the OSNR of our 10 GHz PMCW seed comb is greater than 30 dB.

4.3 Results and discussions

Figure 4.3(a) shows the nonlinearly broadened comb spectra after the DDF and HNLF with average seed pulse power of 18 dBm for both cases. This input power is sufficient to place our PMCW seed pulses into adiabatic soliton compression regime. Both combs provide ~8 nm optical bandwidth within -10 dB off the peak with the optical spectrum analyzer set for 0.01nm (1.25GHz) resolution. The PMCW comb is also included for comparison. DDF and HNLF comb portions at 1538 nm are magnified within the inset. Experimental (solid) and calculated (dashed) intensity autocorrelations of the corresponding pulses are given in Fig. 4.3(b). The calculated curves are obtained using the measured optical power spectrum, with the assumption of flat spectral phase. For the HNLF-broadened comb, a coarse resolution pulse shaper with phase value of $\Phi(\omega) = (-9.1\pi)\left(\frac{\omega - \omega_0}{64 \cdot 2\pi \cdot f_{rep}}\right)^2 + (3.2\pi)\left(\frac{\omega - \omega_0}{64 \cdot 2\pi \cdot f_{rep}}\right)^3$ (where f_{rep}=9.953 GHz) applied to the LCM is used to compensate the dispersion of the HNLF fiber. The quadratic phase applied is equivalent to 24.5m worth of single mode fiber. De-convolved pulse widths of 415 and 526 fs are obtained for DDF and HNLF, respectively. Such short pulse widths are desirable for ultrafast optical time-division multiplexed communications.

To assess compatibility with short pulse coherent communications, phase-coding and DPSK decoding are performed on both comb outputs. Figures 4.4(a) and 4.4(b) show DPSK decoded BER data (symbols) and fitting curves (lines) for the DDF comb, for various optical power levels (up to -12.0 dBm) at the receiver, and for the HNLF comb, respectively. BER results for the PMCW comb are also plotted in both figures for comparison. Considering Fig. 4.3(a), the DPSK performance suffers a power penalty of ~ 5 dB as compared to the PMCW comb when the entire DDF comb is used (All, diamond). Intuitively, different spectral portions may exhibit different comb qualities, and increased degradation is expected further into the wings. Spectral slicing (2 nm per different spectral regions of interest) is now performed to examine the spectral dependence of the comb quality. BER results show that the portion of the broadened spectrum coincident with the original PMCW comb (DDF 1542 nm) has better performance than using the whole comb, but still suffers a ~3 dB power penalty as compared to PMCW comb. DDF spectral slices centered at 1546 and 1538 nm have an evident larger power penalty.

Figure 4.4(b) shows DPSK BER results for the HNLF comb. Excellent DPSK performance is obtained using either the entire HNLF comb (All, solid diamond) or any of the spectral slices, with less than 0.7 dB power penalties as compared to the PMCW comb results. We attribute this pronounced difference to the fact that modulational instability does not exist in the normal group velocity dispersion HNLF, in contrast to the comb broadened in the anomalous dispersion DDF.

Various mechanisms may have contributed to the differences in DPSK performance between the two nonlinearly broadened combs having comparable optical bandwidth. In order to gain further insight, conventional comb diagnostic methods used within Refs. [51,54-56] are also performed. First, the optical linewidths of different comb portions are measured via heterodyne beating with a reference CW laser with 15 MHz linewidth. For all the DDF and HNLF comb spectral portions, comb linewidths are determined to be narrower than this 15 MHz instrumental limit. Figure 4.5 shows the heterodyne beating results for the HNLF 1542nm and 1538 nm portion, DDF 1542 nm and 1538 nm portion and the PMCW comb. ESA resolution bandwidth is 300 kHz and the data are acquired using maximum hold function after one minute for the HNLF comb portions and 30 seconds for other comb portions. This method only allows a rough estimate on the upper bound of the potential linewidth broadening during the nonlinear processes. For precise knowledge over the linewidth values, procedures outline in Ref. [57] should be followed. Ref. [61] reports that 75 MHz laser linewidth results in ~1 dB power penalty at BER=10^{-9} for a 10 GHz DPSK system. Since the upper bound for our linewidths are well below this 75 MHz figure, we attribute the degradation of the DDF comb under DPSK operation to other mechanisms.

Secondly, relative intensity noise of the comb spectral slices is measured using an electrical spectrum analyzer. Figure 4.4(c) shows intensity noise power spectral densities for PMCW, DDF comb spectral slices, and the system noise floor, plotted against offset frequency ranging from {-5 to 5} MHz relative to 9.953 GHz (resolution bandwidth=3 kHz). For all comb portions considered, optical powers of -3 dBm are fed to a 60 GHz bandwidth photo-detector. For the PMCW comb, only slight low-frequency noise is observed. All spectrally sliced portions of the DDF comb show both increased low-frequency noise and a white noise floor. Such noise measurement data have been previously interpreted in terms of slow variation in overall pulse energy (due to low frequency technical noise) and fast pulse structure variations (from white high frequency noise) [55,56]. Figure 4.4(d) shows intensity noise power spectral densities for HNLF comb spectral slices. HNLF comb low frequency noise pedestals are magnified in the inset of Fig. 4.4(d), along with the PMCW result (dashed trace) to facilitate comparison. No white noise backgrounds are observed, and only slight low-frequency noise pedestals are observed for 1538 and 1546 nm spectral slices. These observations qualitatively agree with the comb optical spectral measurements, where degradation in OSNR is observed for the DDF comb as compared to the HNLF comb. Taking the 1538 nm spectral slice for example (inset, Fig. 4.3(a)), the optical extinction ratio is about 20 dB for the DDF comb but 23 dB for the HNLF comb, as measured using OSA setting in 1.25GHz resolution. Increased RF noise from ESA measurements may be in part due to the beating of optical comb lines with the optical noise between the lines. From the inset of Fig. 4.4(d), the 1546 nm and 1538 nm slices have increased low frequency noise (roughly 6 dB) as compared to the 1542 nm and PMCW comb. This is consistent with the slight power penalties for the 1546 nm and 1538 nm spectral slides (by roughly 0.3 dB), which are apparent in the expanded BER curves plotted in Fig. 4.4(e).

Our third concern is timing jitter. Unlike non-return-to-zero coherent communications with long pulses, precise time alignment in the DPSK decoder is of critical importance for short pulse communication systems. Hence short pulse coherent communications is expected to be highly sensitive to timing jitter. High-precision timing jitter values can be obtained by physically separating intensity noise from pure phase noise and has been well documented [62]. This approach requires two photo-diode pairs, one pair biased precisely in phase and the other precisely biased in quadrature, making a complete system implementation complex.

Here we adopt another approach. Table 4.1 shows the integrated single-side noise power spectral density for different comb portions within offset frequency range {100 Hz ~ 1 MHz} for each of the first four RF harmonics. These values are obtained using the built-in function of our ESA termed as "PHASE-NOISE UTILITY". Although named "phase-noise," what our ESA does is simply integrating the single-sided noise power spectral density (intensity and phase noise inseparable), in unit of radian. We can then extract the timing jitter value using the well known relation that the timing jitter may be identified as the contribution to the integrated noise density which depends quadratically with harmonic number [63], while intensity noise is independent of harmonic number. We simply express the integrated total noise power spectral density with certain frequency offset range $N_T(f)$ as for the kth RF harmonic as

$$N_T(f) = N_{Int}(f) + k^2 N_{Phase}(f) \tag{4.1}$$

where $N_{Int}(f)$ denotes the contribution of harmonic-independent intensity noise, and $N_{Phase}(f)$ denotes the phase noise contribution that depends quadratically on harmonic number k within the measured offset frequency range. Root-mean-square (rms) timing jitter value can then be obtained by extracting $N_{Phase}(f)$ and divided by $2\pi f_{rep}$ (in our case f_{rep}= 9.953 GHz).

Extracted $N_{Int}(f)$ and rms timing jitter values using this approach are shown in Table 4.2 for different portions of the comb. The measured timing jitter values are qualitatively consistent with the DPSK BER results: both the full DDF comb and the various spectral slices of the comb have significantly increased jitter compared to the initial PMCW comb (63.13 fs) as well as significantly degraded BER performance. This suggests that increased timing jitter for the DDF comb is a key factor impacting BER performance. In contrast, the various HNLF splices all retain low timing jitter similar to the initial PMCW comb, which is consistent with their excellent BER performance under DPSK decoding. The retrieved timing jitter values have a nominal 25% error, the reasons are discussed in the next paragraph.

We attribute our hindered timing jitter measurement precision to the following reasons: (1) Only four observable harmonics limited by the bandwidth of our ESA and our high repetition rate. In the ideal case, one would prefer to have more harmonics for better precision. Another simply approach would be a direct measure of the single-sided noise power spectral density for a very high RF harmonics (say, twentieth, so the effect of intensity noise is some 1/400 as compared to that arising from timing jitter), and treat all the noise contributions as from timing jitter. (2) Limited optical input power into the photo-detector. Since we are exciting the photo-detector with short pulses, one should be concerned about the instantaneous peak photo-current generated. (3) Limited frequency range. The lowest offset frequency allowed by our "phase-noise" utility is 10 Hz while the upper bound is 100 MHz. (4) The repeatability of the integrated noise power spectral density measurement is not very good (about 15% error). And the repeatability is worse for higher RF harmonics. This point is most evident in the DDF comb portions. Giving one example, the integrated noise power spectral density value for DDF 1542 nm at $4f_{rep}$ can vary between 0.2603 to 0.423 in radian. The measurement repeatability for PMCW and HNLF comb portions are better (within 15%), and in certain extent can be viewed as another manifestation of the better comb quality over the DDF comb. For future improvements in obtaining timing jitter values with higher precision, we should consider either constructing the systems outlined in Ref. [62]. An alternative is acquiring commercialized systems from vendors such as Agilent Intensity/Phase noise measurement system E5504A/B.

It is interesting to note that our DDF results are in apparent contrast to those reported by Refs. [47] and [51], where DDF have been successfully used to generate pulses for transmission experiments at greater than 1 Tb/s and where DDF-generated supercontinuum was reported to exhibit favorable noise properties, respectively. Although the reasons for this discrepancy are not known, we would like to point out three reasons that may contribute to the resolution of these differences:

(1) Dispersion tailoring of the DDFs may play a critical role in the spectrally broadened comb properties. In Ref. [51], specially engineered anomalous dispersive DDF with varying core shapes were fabricated during drawing; while in Ref. [64], dispersion-flattened DDFs with W-shaped core were used to generate a broad output spectrum. Such special DDFs are not generally available. The conclusion of Ref. [51] was the DDF

resulted in supercontinuum with much lower noise compared to a normal dispersion fiber with dispersion value of almost zero. However, it has also been demonstrated by working in a larger normal dispersion value regime (similar to the case for our HNLF) that supercontinuum can be generated both with well preserved phase coherence and with low amplified incoherent noise and low intensity fluctuations [52,53].

(2) The requirements on the OSNR of the seed comb may be more demanding for DDF than for HNLF. In Ref. [51], it was shown that a 30 dB OSNR at the input to the DDF generated a high quality output comb from the DDF, but when the OSNR was intentionally lowered to 23 dB the output comb was seriously degraded. The OSNR of our seed PMCW comb (~30 dB) is comparable to the condition described in Ref. [51]. Therefore, OSNR would not appear to explain the difference between our results and that of [11], unless OSNR requirements vary significantly with details of the DDF dispersion profile.

(3) For adiabatic soliton compression, the shape of the input seed pulse may also be an important factor. Ideally, adiabatic soliton compression works for pulses showing sech temporal field profile. In the prior studies using DDF, seed pulses have been generally obtained from mode-locked laser outputs, where the pulses generally show high extinction ratio and are either sech or Gaussian in shape. PMCW seed pulses, however, owing to the comb spectral profile, are expected to have a different shape with larger pulse pedestals. This deviation from the soliton profile may also contribute to the degraded coherence and increased background noise observed in our DDF compressed comb. On the other hand, normally dispersive HNLF does not have an inherent requirement on the input seed pulse shape.

In any case, clarification of the conditions needed to preserve low noise in compression using DDF remains an important open research question. Further investigations would be especially interesting for seed pulses generated from the PMCW combs.

Frequency comb with DDF and subsequent nonlinear optical loop mirror (NOLM) for pulse pedestal removal (using the same setup as shown in Fig. 2.5 and output pulse as shown in Fig. 2.7(e)) is also studied using DPSK decoding process. Fig. 4.6(a) shows the resulting optical comb spectrum after the NOLM. First we noticed the OSNR is much degraded (less than 15 dB), as shown within the inset. For such a small OSNR, DPSK decoding was not possible. Fig. 4.6(b) shows a typical eye diagram where no eye opening can be obtained for any spectral portion. 1542 nm spectral sliced intensity noise power spectral density of the NOLM, DDF and PMCW combs are plotted in Fig. 4.6(c). The

NOLM comb show larger intensity noise as compared to the DDF comb. From these evidence, we can infer noise generated as a results from the DDF comb are further amplified within the NOLM.

In summary, we have characterized mainly two different frequency combs, generated via phase modulation of a continuous-wave laser and spectrally broadened in either dispersion-decreasing fiber or normal dispersion highly nonlinear fiber, via a variety of methods. Our results show that the BER performance of the dispersion-decreasing fiber version in a simple DPSK system is severely compromised, while the BER characteristics of the comb broadened using normal dispersion fiber are essentially unaffected. An important point is that these experiments with DDF and with HNLF were performed with identical input. These observations are consistent with measurements of intensity noise and timing jitter based on radio-frequency spectral analysis. Although it may be possible to obtain better results with DDF under different conditions, as reported in the literature, our results point to PMCW combs spectrally broadened using normal dispersion fiber (and subsequently compressed) as a promising and robust source for ultrashort pulse coherent communications. At the same time, our work shows that DPSK decoding, which accounts for intensity noise, timing jitter, and linewidth degradations within one single process, may be a valuable addition to the suite of tools available for characterization of optical comb sources.

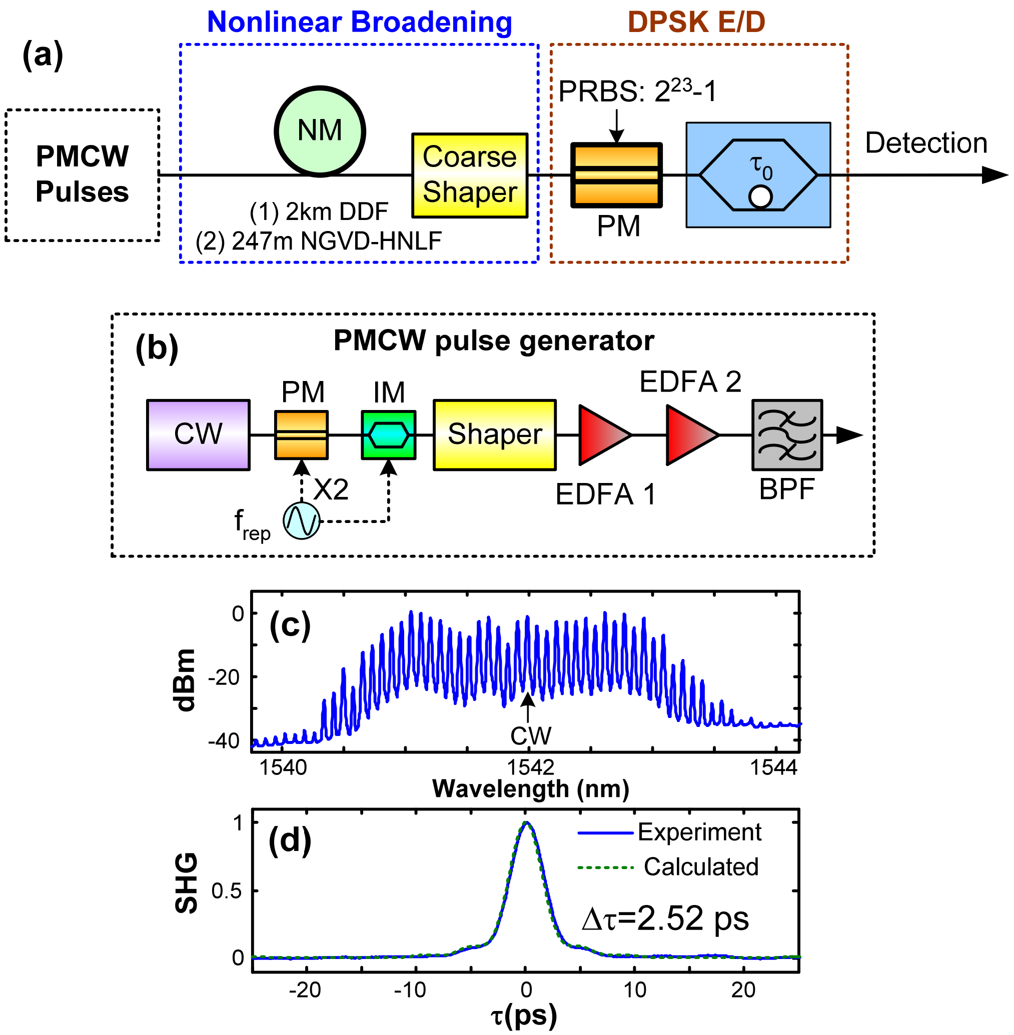

Fig. 4.1. Schematic of experimental setup. NM: nonlinear media; E/D: encoder/decoder. (b) PMCW pulse generation using a line-by-line shaper. PM: phase modulator; IM: intensity modulator; f_{rep}: comb spacing. (c) PMCW comb power spectrum. (d) Experimental (solid) and calculated (dash) intensity autocorrelation of the PMCW pulses.

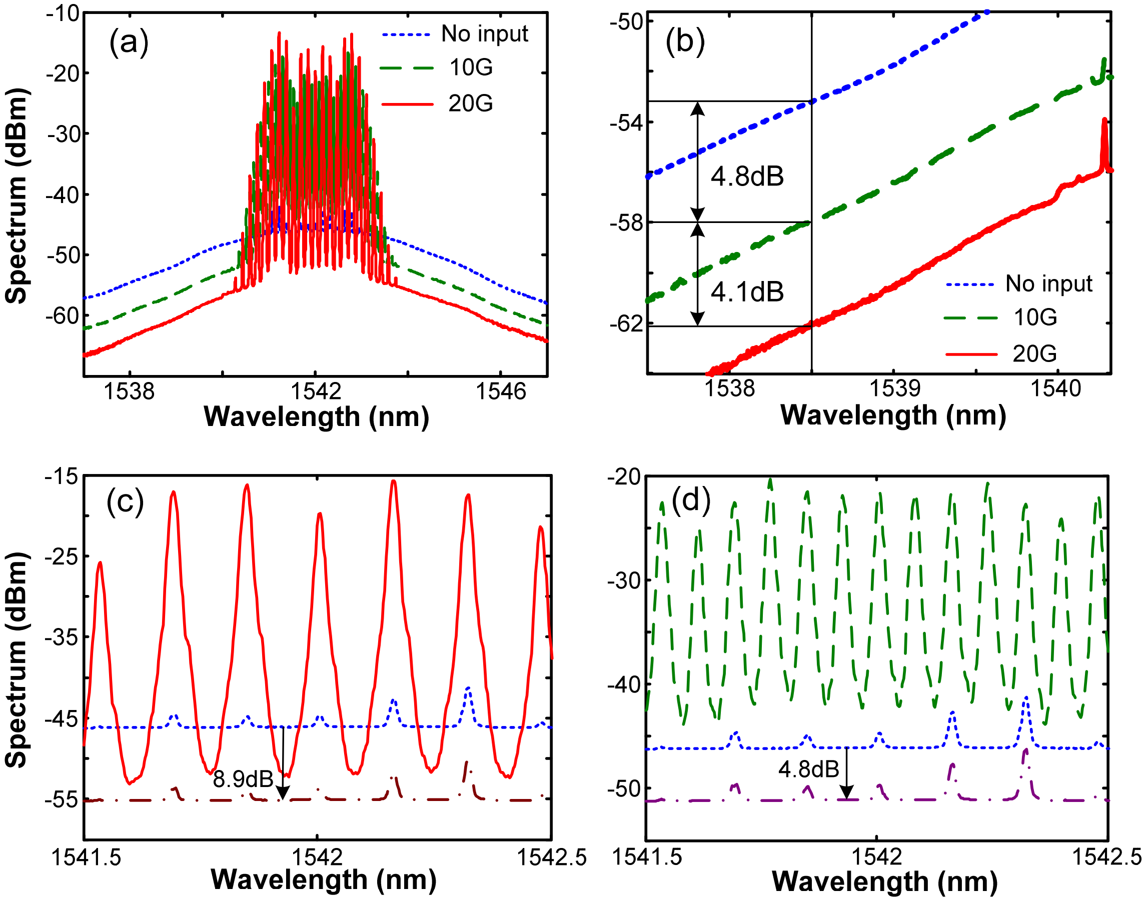

Fig. 4.2. Process for determining the OSNR of the PMCW send comb. (a) Spectra after the band-pass filter when no optical input (dotted), 10 GHz PMCW comb (dashed) and 20 GHz PMCW comb (solid) are sent into the shaper. (b) ASE noise level for the three cases. (c) 20 GHz comb (solid), ASE noise level (dotted, no input), and ASE noise level shifted down by 8.9 dB (dash-dotted). (d) 10 GHz comb (dashed), ASE noise level (dotted, no input), and ASE noise level shifted down by 4.8 dB (dash-dotted).

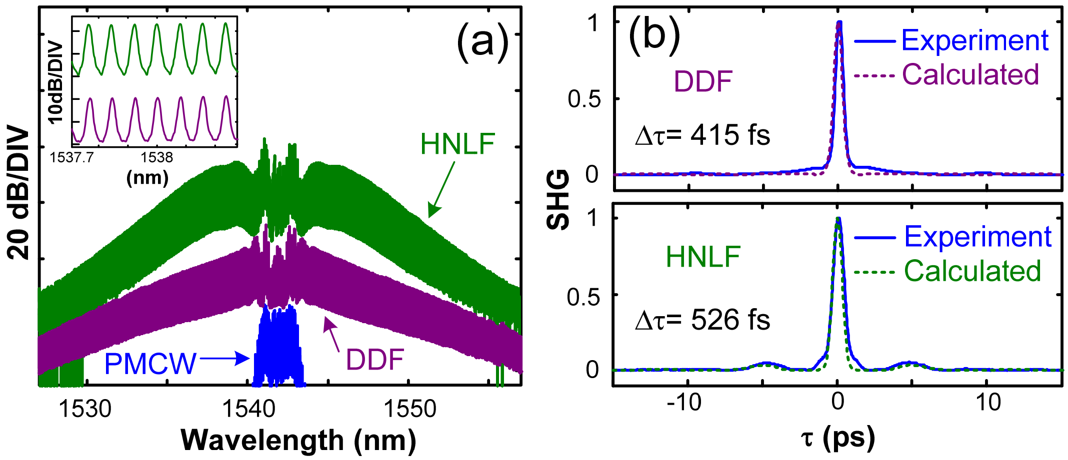

Fig. 4.3. (a) Nonlinearly broadened comb spectra. (b) Intensity autocorrelations of the DDF and HNLF pulses.

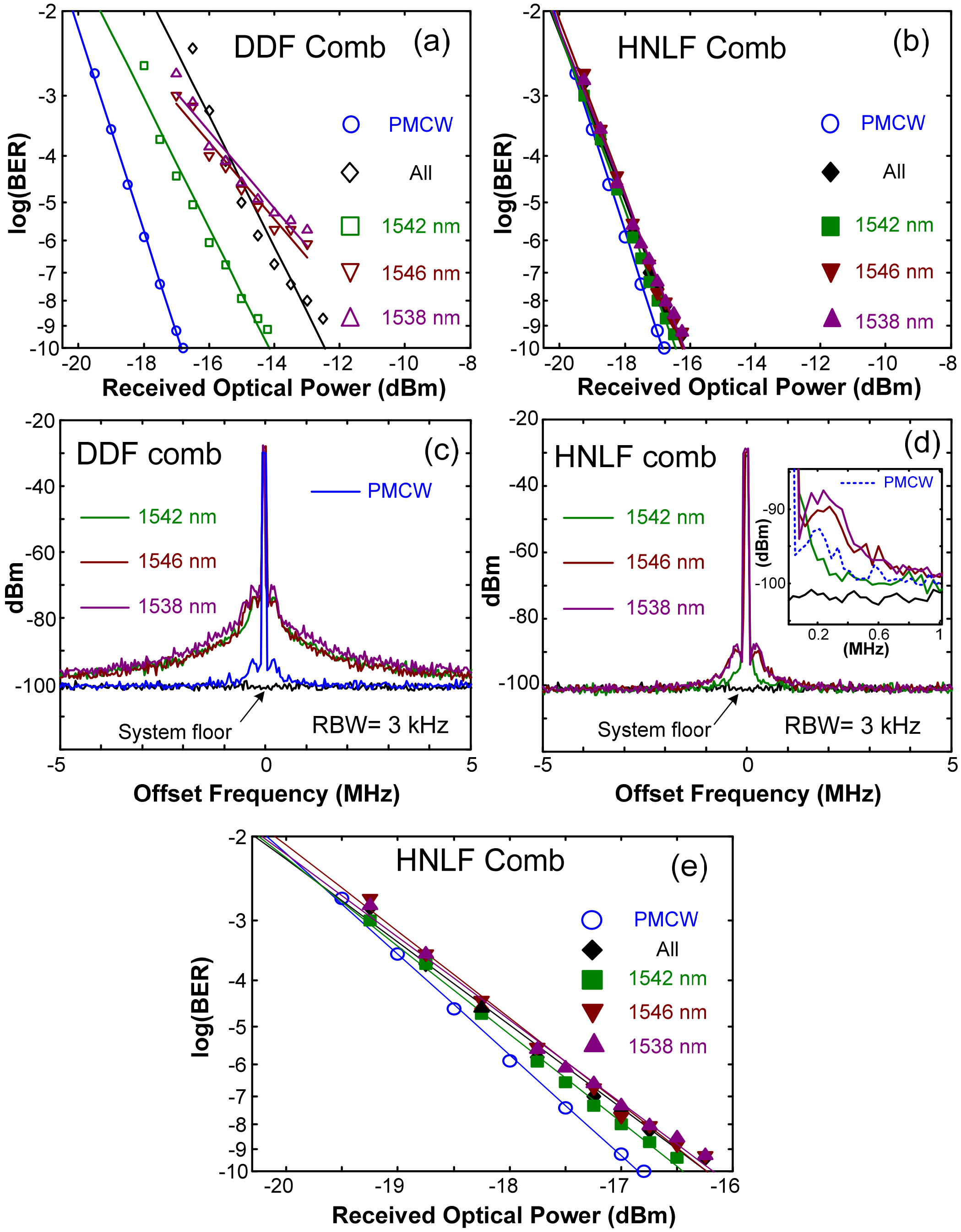

Fig. 4.4. DPSK decoded BER results of (a) PMCW and DDF combs; (b) HNLF comb. In (a, b), data are denoted by symbols and lines the fitted BER curve. Intensity noise measurements of different comb portions for: (c) PMCW and DDF comb and (d) HNLF comb and PMCW (inset). (e) Magnified view of the HNLF comb BER results.

Table 4.1. Integrated single-sided noise power spectral density for different RF harmonics. Integration are performed between offset frequencies of 100 Hz to 1 MHz.

	f_{rep} (rad)	$2f_{rep}$ (rad)	$3f_{rep}$ (rad)	$4f_{rep}$ (rad)
PMCW	0.0120	0.0283	0.0357	0.0474
DDF All	0.0227	0.0429	0.0656	0.1223
DDF 1542 nm	0.0208	0.0422	0.0622	0.0965
DDF 1546 nm	0.0222	0.0453	0.0935	0.2236
DDF 1538 nm	0.0259	0.0499	0.0992	0.2603
HNLF All	0.0139	0.0342	0.0446	0.0633
HNLF 1542 nm	0.0099	0.0230	0.0371	0.0472
HNLF 1546 nm	0.0144	0.0318	0.0370	0.0648
HNLF 1538 nm	0.0151	0.0314	0.0469	0.0676

Table 4.2. Extracted intensity noise ($N_{int}(f)$) and rms timing jitter values for different comb portions integrated from 100 Hz to 1 MHz for different comb portions. Nominal errors in timing jitter values are around 25%.

Comb Portion	$N_{int}(f)$ (rad)	Time jitter (fs)
PMCW	0.0126	63.13
DDF All	0.0193	116.00
DDF 1542 nm	0.0185	109.99
DDF 1546 nm	0.0115	165.34
DDF 1538 nm	0.0150	175.42
HNLF All	0.0143	78.87
HNLF 1542 nm	0.0117	65.60
HNLF 1546 nm	0.0159	65.43
HNLF 1538 nm	0.0152	82.93

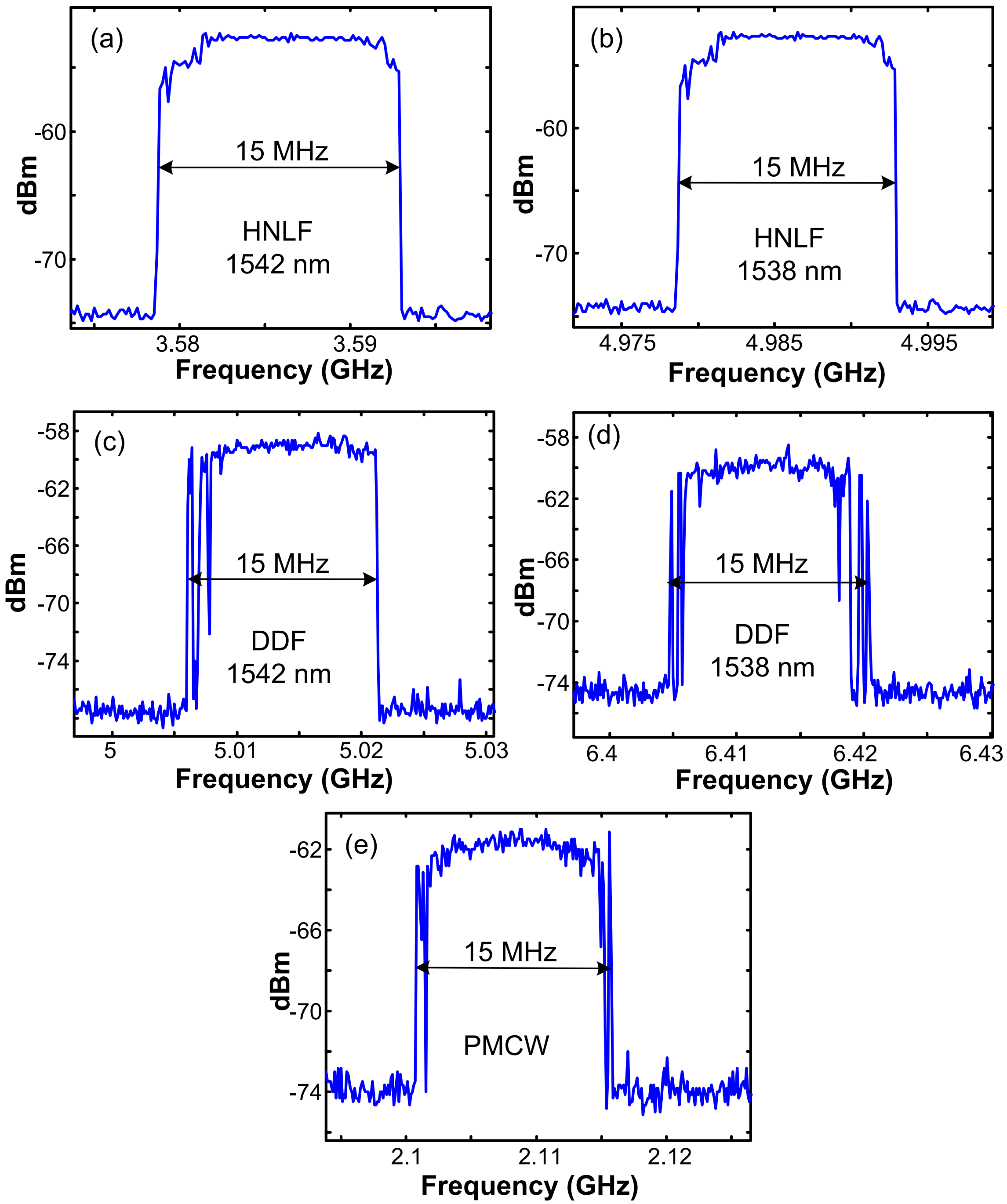

Fig. 4.5. Heterodyne beating results of (a) HNLF 1542 nm; (b) HNLF 1538 nm; (c) DDF 1542 nm; (d) DDF 1538 nm; and (e) PMCW comb with a 15 MHz linewidth tunable CW laser. Resolution bandwidth is 300 kHz, maximum hold for greater than 30 seconds.

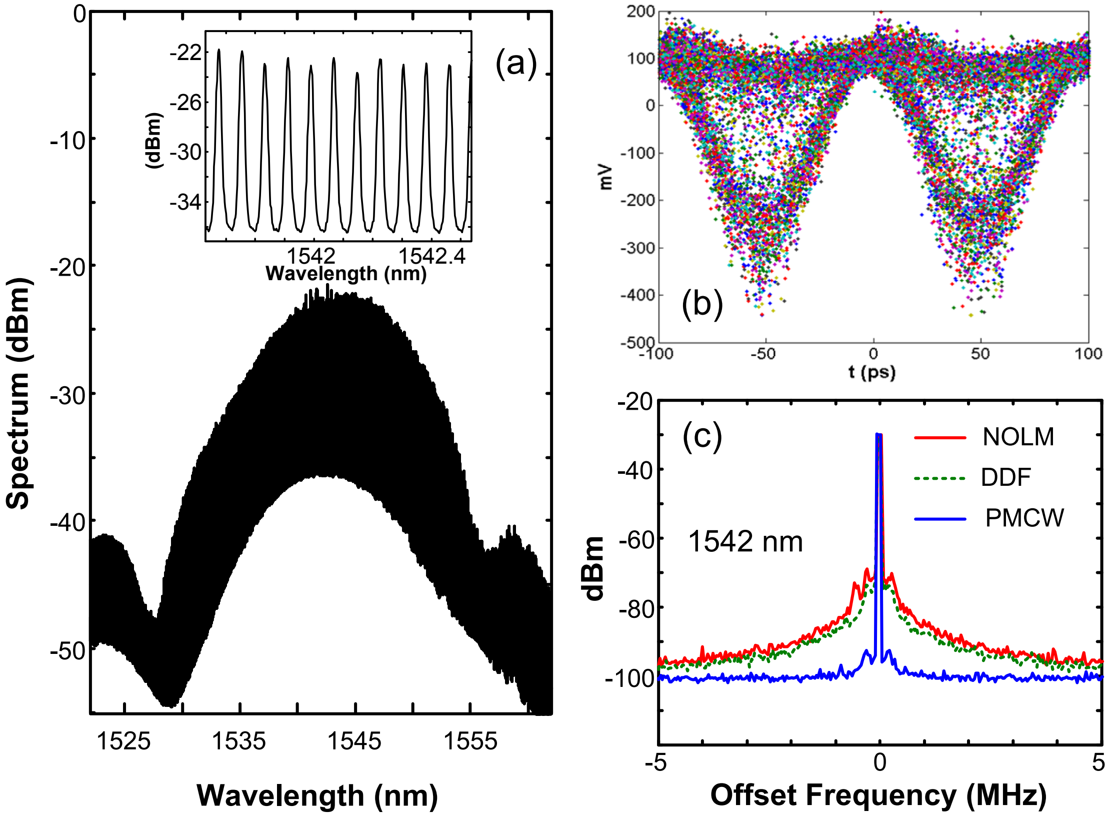

Fig. 4.6. Comb diagnostics for DDF output sent to a nonlinear loop mirror. (a) Optical power spectrum; (b) eye-diagram of the DPSK decoded signal; (c) 1542 nm intensity noise power spectral density of the NOLM, DDF and PMCW combs.

5. THE IMPACT OF OPTICAL COMB FREQUENCY STABILITY ON WAVEFORMS GENERATED VIA SPECTRAL LINE-BY-LINE PULSE SHAPING

In this chapter we systematically investigate the impact of static optical comb frequency shift on the line-by-line shaped waveform intensity [10]. A frequency domain model is developed and justified experimentally.

5.1 Introduction and problem description

Optical combs are comprised of spectral lines that are evenly spaced and determined by the source repetition frequency and with well defined phase relations between the lines [65]. Optical pulse shaping techniques, in which phase and amplitude manipulation of optical spectral components allow synthesis of user-specified ultrashort pulse fields according to a Fourier-Transform relationship, have been developed and widely adopted [7]. Previous pulse shapers, however, have generally manipulated groups of spectral lines rather than individual lines due to difficulty in building a pulse shaper capable of resolving each spectral line at typical repetition frequencies (≤1 GHz) for practical optical combs generated by mode-locked lasers. This results in waveform bursts that are separated in time with low duty factor and that are insensitive to the variation of the frequency offset of the comb lines. However, the phase and amplitude of each individual comb line should be independently controlled in order to approach true optical arbitrary waveform generation (O-AWG) [8]. A pulse shaper capable of implementing line-by-line control can generate shaped waveforms spanning the full time period (T) between the initial mode-locked pulses (100% duty factor). From a time-domain perspective, in the line-by-line regime waveform contributions arising from adjacent pulses in the mode-locked train overlap and interfere. The effect of the interference depends on the relative phase between adjacent mode-locked pulses, which is proportional to the comb offset frequency. Consequently, frequency fluctuations of the mode-locked comb translate into time-dependent waveform noise in line-by-line pulse shaping. This effect fundamentally links the field of pulse shaping with the field of frequency-stabilized mode-locked lasers (combs).

The first observation of such waveform noise in line-by-line pulse shaping was reported in [9] by selecting two comb lines from a harmonically mode-locked fiber laser without active frequency stabilization. The laser was operated at ~10 GHz repetition rate, which made it possible to resolve individual lines using a carefully designed pulse shaper. Selecting only two spectral lines from the broader input spectrum yields a cosine waveform in the time-domain. The relative delay of the peaks of the cosine can be tuned by using the pulse shaper to control the phase (Φ) of one of the selected lines. The pulses are shifted by T/2 (half of the pulse period) if $\Phi=\pi$ is applied to a single line. The experiments in [9] showed that waveform noise related to optical frequency fluctuations was much larger for the $\Phi=\pi$ case than for the $\Phi=0$ case. This difference was understood by observing that largest waveform noise is expected at temporal positions where adjacent input pulses provide equal contributions and hence largest interference, which occurs exactly between the original pulses (at T/2). This time-domain picture provides a successful qualitative explanation of the experimental observations.

In this chapter, we present the first quantitative investigation of the impact of optical comb frequency offsets on the time-domain intensity waveforms generated via spectral line-by-line pulse shaping. Instead of a harmonically mode-locked laser, we employ an optical comb generated by a phase-modulated CW (PMCW) laser. By shifting the center wavelength of the CW laser, the wavelength of the entire comb can be shifted accordingly, while leaving the relative powers, spacing and phases of the lines unchanged. PMCW combs are simple in configuration, stable even at the high repetition rates of interest here, and provide much more flexible tuning over repetition rate and comb offset frequency compared to harmonically mode-locked lasers. Broad PMCW combs have seen significant recent progress [12,13,25,58]. Further, line-by-line shaping on a PMCW comb has been reported previously [15], demonstrating the comb stability necessary for optical waveform processing. Together these attributes of the PMCW laser enable quantitative study of the linkage between variations in comb frequency and pulse shaper output.

Figure 5.1(a) shows the schematic experimental setup. A tunable CW laser is phase-modulated using a lithium niobate phase modulator (12.5 GHz bandwidth, V_π ~5V at 10 GHz) driven at f_{rep}=9 GHz (~1.6 V_π peak to peak) to obtain an optical comb with lines spaced by 9 GHz as shown in Fig. 5.1(b). The frequencies are defined relative to the CW laser frequency. The comb spectrum is observed using an optical spectrum analyzer (OSA) with 0.01 nm resolution. Lines at frequencies higher than the CW laser are all in phase as measured using the method reported in [17]. An expanded view of a few lines is shown in the inset on a linear scale and normalized to line {1}. Using the pulse shaper to select the two lines marked {1, 2} and detuning the center wavelength of the CW laser while the modulation frequency f_{rep} is fixed, we are able to emulate the effects of the frequency offsets in the mode-locked laser of [9].

Figure 5.2 shows experimental results where only two lines, {1, 2}, are transmitted through the line-by-line shaper. Figure 5.2(a, c) show the spectra obtained by detuning the PMCW comb with frequency offset values of {0, 7, 14, 21, 28, 35, 42, and 49}% with either $\Phi=0$ or $\Phi=\pi$ applied to line {1}, respectively. The arrows in Fig. 5.2 indicate the initial line positions (zero offset) and the direction of detuning as the frequency offset is applied. Figure 5.2(b, d) show time-domain intensity waveforms corresponding to the frequency offsets. Intensity waveforms are obtained by sending shaped spectral lines to a 60 GHz photo-detector whose output is measured by a sampling scope with 50 GHz bandwidth. The vertical arrows indicate the evolution of the intensity as the optical frequency offset increases. Throughout this chapter, intensity waveforms are normalized to the peak value measured with zero frequency offset. The temporal delay of intensity waveforms comprised of two frequency lines as a function of the relative phase setting is related through:

$$\tau(\Phi) = \frac{\Phi}{2\pi}\mathrm{T} \tag{5.1}$$

where $T=1/f_{rep}$ is the waveform periodicity and Φ is the phase applied to one line. $\tau(\Phi)$ due to the phase settings ($\Phi=0,\pi$) are shown with dashed lines

With the same value of optical frequency offset, peak intensities of the waveforms of Fig. 5.2(d) ($\Phi=\pi$) change much more strongly with optical frequency variations than those of Fig. 5.2(c) ($\Phi=0$). This finding is consistent with the results obtained in [9] using a non-stabilized harmonically mode-locked laser. The implication is that the phase control in pulse shaping is the primary reason for this difference. In addition, dramatic changes in waveform shape are observed in the $\Phi=\pi$ case which do not occur for $\Phi=0$. In this chapter we will develop a frequency-domain model that allows quantitative prediction of the results of the experiments shown in Fig. 5.2, as well as a series of related experiments.

It is worth noting that relatively large offsets are intentionally introduced in this chapter, so that the impact of frequency instability on time-domain waveform generation can easily be observed with a sampling scope. However, similar time-domain noise effects are expected to be observable even for smaller frequency fluctuations (offsets), provided that more sensitive diagnostic tools are available.

5.2 Theoretical modeling

In the examples shown in Fig. 5.2, it is apparent that the observed time-domain waveform variations are linked to phase manipulation in the pulse shaping process. We now present a model which explains these observations in the frequency-domain.

For a grating based free-space pulse shaper, the effective frequency-domain filter function H(ω) that characterizes its response as a linear filter can be obtained by convolving the programmable spatial masking function M(x) defined by the liquid crystal modulator (LCM) with the Gaussian intensity profile of a single optical frequency beam:

$$H(\omega) = (\frac{2}{\pi w_0^2})^{1/2} \int M(x) e^{\frac{-2(x-\alpha\omega)^2}{w_0^2}} dx \tag{5.2}$$

where w_0 is the Gaussian beam radius (half-width at $1/e^2$ of intensity) and α is the spatial dispersion with units cm $(\mathrm{rad/s})^{-1}$ [7]. In the experiment the frequency lines have a 9 GHz spacing, with each line having a Gaussian spatial profile of radius w_0=75 μm. Each LCM pixel has a 100 μm width and a corresponding frequency span of 4.5 GHz; therefore frequency lines are centered on every second LCM pixel. Our line-by-line shaper has α=3.54e-13 cm $(\mathrm{rad/s})^{-1}$ and a full-width at half maximum spectral resolution of 5.31GHz. The spectral resolution is limited here by the width of turning on one single LCM pixel. This obtained resolution ensures observation of temporal overlapping contributions from adjacent pulses. The output fields of the linear filter $E_{out}(\omega)$ is the product of the input field $E_{in}(\omega)$ and the filter function H(ω):

$$E_{out}(\omega) = E_{in}(\omega) H(\omega) \tag{5.3}$$

Finally, the time-domain envelope function $e_{out}(t)$ is obtained by Fourier transforming the output field:

$$e_{out}(t) = \frac{1}{2\pi} \int E_{out}(\omega) e^{j\omega t} d\omega \tag{5.4}$$

In Fig. 5.3(a), a schematic representation of the optical comb lines in absolute position (black solid) and with an initial frequency offset ε_0 (blue dash) are both depicted as arrows. The comb line positions can be described as [65]:

$$f_m = m f_{rep} + \varepsilon \tag{5.5}$$

where f_{rep} is the repetition frequency, m is a large integer, and ε is the absolute frequency comb offset. For our purpose, however, we note that the pulse shaper acts as a frequency filter (schematically shown in red solid), whose center frequency provides a frequency reference, which we denote as f_s (red dash). To optimally select two comb lines via pulse shaping, the comb frequencies $\{f_m, f_{m+1}\}$ are aligned symmetrically about f_s by fine tuning the LCM position. This means that line frequencies referenced to f_s are:

$$\tilde{f}_m = (m - \frac{1}{2}) f_{rep} \tag{5.6}$$

regardless of the actual offset frequency ε. Figure 5.3(b) shows the two lines (blue dash) with the filter function magnified and plotted against $\tilde{f} \equiv f - f_s$. After alignment, if the comb offset varies from its initial value to ε'=ε+ δε (green solid), what is observed by the pulse shaper is only the frequency offset change δε. Nonzero values of δε will eventually induce power loss as the lines approach the edges of the filter function, and this will transform into waveform variations in the time-domain. It is important to emphasize that only the relative frequency offset is important in line-by-line pulse shaping, not the absolute offset.

In Fig. 5.3(c) we show M(x) defined as a four-pixel pass-band filter (blue solid); 4 pixels are turned on with constant phase across the aperture. Recall that 4 pixels in our setup correspond to 2 comb lines. The effect of convolving a finite Gaussian beam (green dash) with a rectangular-like mask function will smear out the abrupt amplitude transitions at the pixel edges resulting in a non-rectangular |H(ω)|, as shown in Fig. 5.3(d). Filter functions on a logarithmic vertical scale obtained experimentally by sweeping the wavelength of a CW laser (blue solid) and by simulation (green dash) are shown for comparison. The two selected spectral lines are indicated by red arrows.

In Fig. 5.3(e), the lower frequency line (two left pixels) has an applied π phase shift, resulting in a negative mask field. Figure 5.3(f) shows the resulting experimental (blue solid) and simulated (green dash) |H(ω)| spectra in log scale - both reveal an obvious spectral dip. This dip can be understood as the field interference due to an abrupt spatial (π-0) phase transition; this results in diffraction of energy out of the main beam, which is eventually eliminated while coupling back into a single-mode optical fiber at the output of the pulse shaper.

In Fig. 5.3(f), the applied phase control induces a frequency-dependent transmission dip at the center of the pass-band. This dip functions as a frequency discriminator that is not present in the four-pixel pass-band filter with constant phase. This is the essential point used to explain the observed time-domain waveform instability shown in Fig. 5.2(d) when spectral phase control is applied. Under line-by-line phase control, H(ω) is no longer flat in the frequency-domain; thus a relative frequency offset ε_r in the optical comb will effectively be transferred to an extra energy loss by the central frequency discriminator. This loss viewed in the frequency-domain will result in large peak intensity variation in the time domain.

5.3 Data fitting and discussion

In Fig. 5.4, a fit is shown to the experimental data presented in Fig. 5.2 using the frequency-domain model presented above. Figure 5.4(a, c) show the normalized optical spectral line amplitudes in linear scale with experimental frequency offset values. The 4-pixel bandwidth filter functions are included (shown in red dash) for Φ=0 (a) and Φ=π (c) applied to line {1}. Relative line amplitudes of the 0, 1, 2 and 3 lines are determined from the spectrum shown in Fig. 5.1(b). The necessity of using 4 comb lines is to reflect the fact that although only lines {1, 2} are selected at zero offset, additional lines from either side of the comb may participate in shaping for a large frequency offset (lines {0 or 3}, depending on the direction of frequency offset). Arrows indicate the initial line positions and the direction of increasing frequency offsets. Figure 5.4(b, d) show time-domain intensity waveforms corresponding to the various frequency offsets for Φ=0 (b) and Φ=π (d). The arrows indicate the evolution of amplitudes according to the change in frequency offset. The temporal delays of the waveforms (τ) as a result of the phase manipulation are also shown (dashed lines).

Comparing theoretical calculations shown in Fig. 5.4 and experimental results shown in Fig. 5.2 demonstrate excellent agreement. Several key features for discussion are: (i) For the Φ=0 case (Fig. 5.2(a) and Fig. 5.4(a)), only the amplitude of line {1} is attenuated. The amplitude of line {2} is not attenuated due to a change in frequency offset since the filter function is flat. The corresponding time-domain intensities (Fig. 5.2(b) and Fig. 5.4(b)) are therefore relatively insensitive to frequency offsets. Less than 35% variation in peak intensity occurs even for a 49% frequency offset. (ii) For the Φ=π case (Fig. 5.2(c) and Fig. 5.4(c), τ(π)=T/2), the amplitudes of both lines {1 and 2} are attenuated monotonically due to the increasing frequency offsets, due to the central transmission dip. The corresponding time-domain intensities (Fig. 5.2(d) and Fig. 5.4(d)) are therefore much more sensitive to change in frequency offset. For a 49% frequency offset, the change in I(τ(Φ)) is in excess of 95%. These two examples demonstrate the utility of the frequency-domain model, and provide a link with the time-domain picture provided in [9]. In particular, the time-domain picture predicts maximum intensity variation happens at odd multiples of T/2 (the temporal position centered between the original pulses), where contributions from adjacent pulses overlap and interact most strongly. With a phase step of $\Phi=\pi$ between adjacent spectral lines, the peak intensities are delayed to exactly odd multiples of T/2, therefore producing a large intensity variation.

Examination of the $\Phi=\pi$ amplitude variation (Fig. 5.2(d) and Fig 5.4(d)) shows that the periodicity of the waveforms gradually evolves to T/2 as the frequency offset increases. The origin of this repetition rate doubling is explored in Fig. 5.5. In Fig. 5.5(a), comb lines (arrows) and the filter function (red dash) are schematically sketched against relative frequency. The blue solid arrows show the initial comb line positions and the green dashed arrows show the comb with a frequency offset $\delta\varepsilon$, while keeping line amplitudes fixed. The lines are spaced apart by f_{rep}. When one of the spectral lines has an applied π phase shift relative to the other line, the field of the filtered comb is depicted in Fig. 5.5(b), with one line having negative amplitude. The corresponding time-domain intensity is shown as the blue solid trace in Fig. 5.5(d), a cosine function having period of T with delay $\tau(\Phi)=T/2$. Figure 5.5(c) shows the resulting filtered comb with offset $\delta\varepsilon$, constituting three lines denoted as {i, ii, iii}. Note that the amplitudes of all the lines are affected by the frequency-dependent transmission of the filter, while the signs read {+,+,-}, respectively. The corresponding time-domain intensity for the lines with this particular phase sequence, shown as the green dashed trace in Fig. 5.5(d), yields a shifted cosine function now with periodicity of T/2. This phenomenon can be understood from the beating between each two lines: the 9 GHz beating of lines {i, ii} almost cancels with that from {ii, iii}; what is left is the remaining 18 GHz beating between lines {i, iii}. The ability to predict subtle details of the experiment, such as the evolution of the intensity periodicity from T to T/2, again demonstrates the power of our frequency-domain treatment.

5.4 Correlating frequency and time-domain pictures: intermediate phases

Thus far phase steps between adjacent optical frequency comb lines have been limited to $\Phi=0$ and π. This means the intensity waveform is shifted from 0 (temporal position with least impact to comb offset) to T/2 (position which is most vulnerable to offset) according to temporal delay $\tau(\Phi)$ defined in Eqn. (1). In this section we examine other phase steps in order to investigate the dependence of the maximum peak amplitude variation on both frequency offset and delay.

Experimental and calculation results together with Φ=0 and π cases demonstrated previously are shown in Fig. 5.6. Figure 5.6(a) shows experimental (symbols), and calculated (lines), intensity values $I(\tau(\Phi))$ at $\delta\varepsilon$ of {0, 7, 14, 21, 28, 35, 42 and 49}%. Phase controls Φ are applied between 0 and π in $\pi/4$ increments to line {1}. The magnitudes of intensity variation increase with increasing $\tau(\Phi)$ (in the direction of the black vertical arrow). Figure 5.6(b) shows $I(\tau(\Phi))$ at $\delta\varepsilon$=49% for different Φ values using a PMCW comb (blue circle: experimental; blue solid line: calculation). $\tau(\Phi)$ is also included within the figure: experimental (diamonds) and calculation (dotted line). The perfect linearity of the trace indicates excellent control over phase settings to individual lines. In all calculations, the optical comb line amplitudes follow the experimental spectrum as shown in Fig. 5.1(b). Results show errors of less than 10% between experimental data and calculations. Together, Fig. 5.6(a) and 5.6(b) indicates that the amplitude change of $I(\tau(\Phi))$ increases monotonically both with frequency offset and temporal delay, in agreement with the time-domain view presented previously.

As a further example, calculated results of $I(\tau(\Phi))$ at $\delta\varepsilon$=49% assuming an ideal comb comprised of equal amplitude lines (red square) are plotted against $\cos^2(\Phi/2)$ (red dashed line) in Fig. 5.6(b). Using the linear dependence of $\tau(\Phi)$ on Φ, we infer that for an ideal comb, the range of intensity variation with frequency offset follows a temporal mask of the form $\cos^2(\pi f_{rep}\tau)$. We will use this empirical observation as an aid to interpret some of our later results.

Please note that the form of this relation may depend on pulse shaper resolution. In the current experiments, our pulse shaper spectral resolution is 1.7 times finer than the line spacing, which leads to a regime where the waveform interference in the time-domain is dominated by contributions from only nearest neighbor pulses. This corresponds most closely to the simple time-domain model put forth in [9].

5.5 Waveforms for comb frequency offset monitoring: design approach

As discussed above, phase manipulation of one spectral line for a two-line cosine time-domain waveform is sensitive to spectral frequency shifts. We can therefore ask the question: can line-by-line pulse shaping be used to monitor variations in the comb offset frequency, at least in the large frequency fluctuation regime? For the purpose of frequency fluctuation monitoring, it would be useful to design waveforms that not only exhibit temporal positions that are sensitive to frequency fluctuation, but also have stable reference points. The existence of a reference point that is insensitive to optical frequency fluctuations would allow one to distinguish waveform changes arising from pure frequency fluctuations from the effects of laser intensity fluctuations. This should also increase the sensitivity of such a scheme for monitoring optical comb frequency fluctuations.

Based on the previous discussions, one simple choice of target waveform would be a time-domain cosine generated by selecting two spectral comb lines. In general, one can select any two spectral lines separated by Nf_{rep}, where N is an integer. For the N=1 example discussed above, we have shown that there is significant sensitivity to frequency fluctuations at time positions equal to odd multiples of T/2 but not at multiples of T. Let us assume that this behavior applies also for N>1, which is justified by the results given below. Then any two lines spaced apart by $2f_{rep}$ or greater will exhibit waveform positions both sensitive and insensitive to comb fluctuations, since there will be peaks situated at multiples of T/N. Furthermore, applying a phase shift onto one of the two lines allows us to finely shift the positions of the peaks for optimum sensitivity.

To illustrate this argument, Fig. 5.7 shows simulation results using the frequency-domain model. For simplicity, an ideal comb of f_{rep}=9 GHz spacing (T=111.1 ps) is assumed with spectral comb lines of equal amplitudes. Figure 5.7(a) shows a filter designed to select two lines spaced by $2f_{rep}$ (N=2) which removes the intermediate line. Optical frequency comb offsets of {0-50}% with 10% per step are indicated. The corresponding time-domain waveforms are shown in Fig. 5.7(b). I(0) is invariant while I(T/2) is sensitive to frequency fluctuations. The $\cos^2(\pi f_{rep} t)$ is plotted (green dashed line) to emphasize the temporal intensity variation relation discussed in the previous section. The ratio of I(T/2) to I(0) offers a clear indication of frequency offsets, especially for large offsets. Figure 5.7(c) shows the semi-log plot of the contrast ratio with various offset values. The scenario is different if one of the lines is π-shifted, shown in Fig. 5.7(d). Since the waveforms are delayed by T/4, all the peaks encounter the same amount of intensity variation. One interesting observation is how the $\cos^2(\pi f_{rep} t)$ function nicely cuts the intensity waveform at 50% offset. This once again supports our conclusion drawn from the previous section.

5.6 Waveforms for comb frequency offset monitoring: experimental results

A broader and flatter optical comb is favored for this experiment to better approach the ideal comb (equal intensities for the comb lines). A low V_π lithium niobate phase modulator (20GHz bandwidth, V_π of ~2.8V at 1 GHz) is modulated at f_{rep}=9GHz with a driving voltage of ~2.6 V_π peak to peak to obtain the spectrum shown in Fig. 5.8(a). Relative phases of the lines are measured for lines {-6 to 5}. Lines {1, 0, -3, and -5} are π out of phase with the rest, which agree with calculation using a Bessel series [5]. Figure 5.8(b) shows an expanded portion of the comb on a linear scale with line powers normalized to line {3}. Lines {2 and 4} are selected to pass through the pulse shaper while the others are blocked by applying amplitude control to the line-by-line shaper to obtain two spectral lines spaced by $2f_{rep}$.

Figure 5.9 shows experimental and calculated results for this waveform. Figure 3.9(a, b) show the experimental spectra and line amplitudes used in the calculation with $\delta\varepsilon$ of {0, 7, 14, 21, 28, 35, 42, and 49}%, both in linear scale. In both figures, the horizontal arrows indicate the initial line positions and the direction of detuning. In Fig. 5.9(b), the amplitudes of the spectral lines reflect the experimental spectrum shown in Fig. 5.8(b). Figure 5.9(c-e) show resulting time-domain profiles for the various shifts of the frequency comb with phase Φ={0, π/2, and π} applied to line {2}, respectively. Figure 5.9(f-h) show the corresponding calculated intensities reflecting the experimental conditions. In Fig. 5.9(c-h), vertical arrows indicate intensity variations as the optical frequency offset increases for different temporal positions; zero delay and T/2 positions are marked as an aid to the eye.

Again the agreement between data and theory is excellent. Even the detailed features observed at large frequency offsets show excellent correspondence. For example, both Fig. 5.9(c) and 5.9(f) show the repetition period changing from T to T/2; both Fig. 5.9(d) and 5.9(g) show temporal shifts in the peak near T/2; and both Fig. 5.9(e) and 5.9(h) show symmetric waveform shifts about t=0. In the end, it is the waveform with $\Phi=0$ (c and f) that is of primary interest for monitoring of optical comb frequency shifts. In contrast to Fig. 5.7(b), where intensity values at I(0) are invariant to frequency offsets, I(0) in Fig. 5.9(c ,f) increases slightly with increasing frequency offset. This results in an enhanced sensitivity to frequency shifts and is attributed to the unevenness of the PMCW line powers in Fig. 5.8(b). Under large frequency offset, the strong central line {3} that is initially blocked contributes to pulse shaping and accelerates the variation in the intensity waveforms.

5.7 Waveforms for comb frequency offset monitoring: larger N values

One may extend the spacing between the two selected lines to achieve similar results. Figure 5.10 shows simulation results for an ideal (equal amplitude) comb for N=3 (a-d) and N=4 (e-h). Note how well the frequency-offset intensities correspond to the $\cos^2(\pi f_{rep} t)$ function. The time-domain picture is clearly illustrated: frequency sensitivity of waveforms generated via line-by-line pulse shaping in the 100% duty cycle regime is least noticeable at time positions equal to 0 (or integral multiple of the repetition period T) and increasingly noticeable for increasing time offsets. Maximum intensity variations with frequency offsets occur for time positions of T/2 and its odd multiples.

In summary, the impact of frequency comb shifts on time-domain waveforms generated through line-by-line shaping has been quantitatively investigated. The influence of frequency offset on generated waveforms is explained from both time and frequency-domain perspectives. A quantitative frequency-domain model is provided starting from pulse shaper theory. Time-domain intensity variations that have previously been observed in pulse shaping due to an unstable mode-locked frequency comb are experimentally emulated using a wavelength detuned phase-modulated CW laser, which allows quantitative analysis. The experimental data are in excellent agreement with the predictions of our frequency-domain model. Finally, we propose and model pulse shaper waveforms that should be useful for monitoring the optical frequency fluctuations of the input comb.

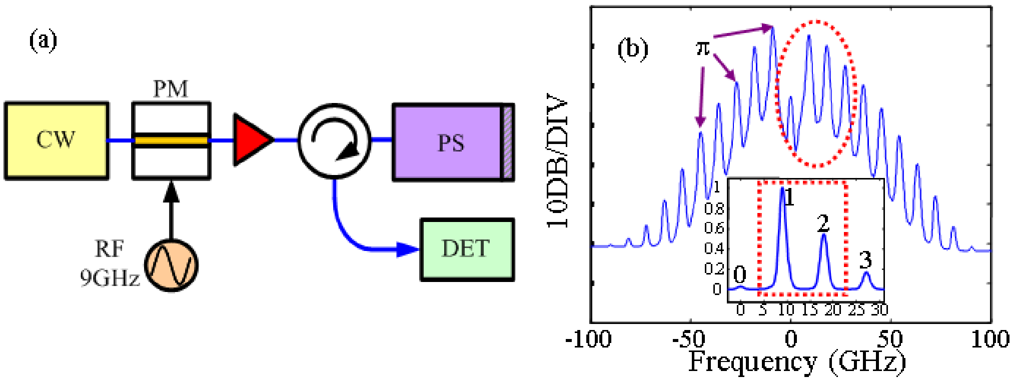

Fig. 5.1. (a) Schematic of experimental setup. PM: phase modulator; PS: reflective line-by-line pulse shaper; DET: to OSA or sampling scope. (b) Optical spectrum of the phase-modulated CW laser frequency scale relative to the CW line. The frequency lines are separated by 9GHz. Inset: lines circled are expanded and plotted on a linear scale. Lines {1, 2} are selected by the line-by-line shaper.

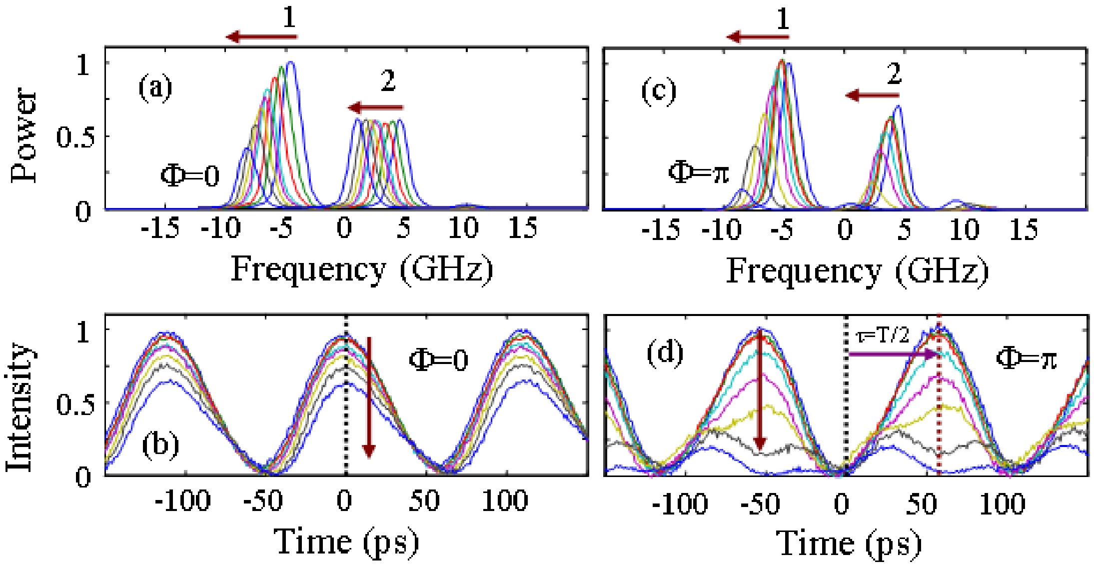

Fig. 5.2. Experimental results by detuning the PMCW comb with relative frequency offsets of {0, 7, 14, 21, 28, 35, 42 and 49}%. (a, c) Spectra (linear scale in relative frequency) for Φ=0 and Φ=π, respectively. The horizontal arrows indicate the initial line positions and the direction of detuning. (b, d) Time-domain intensities for corresponding frequency offsets for Φ=0 and Φ=π, respectively. The vertical arrows indicate intensity peak variations as the optical frequency offset increases. Zero delay positions are marked by dashed lines.

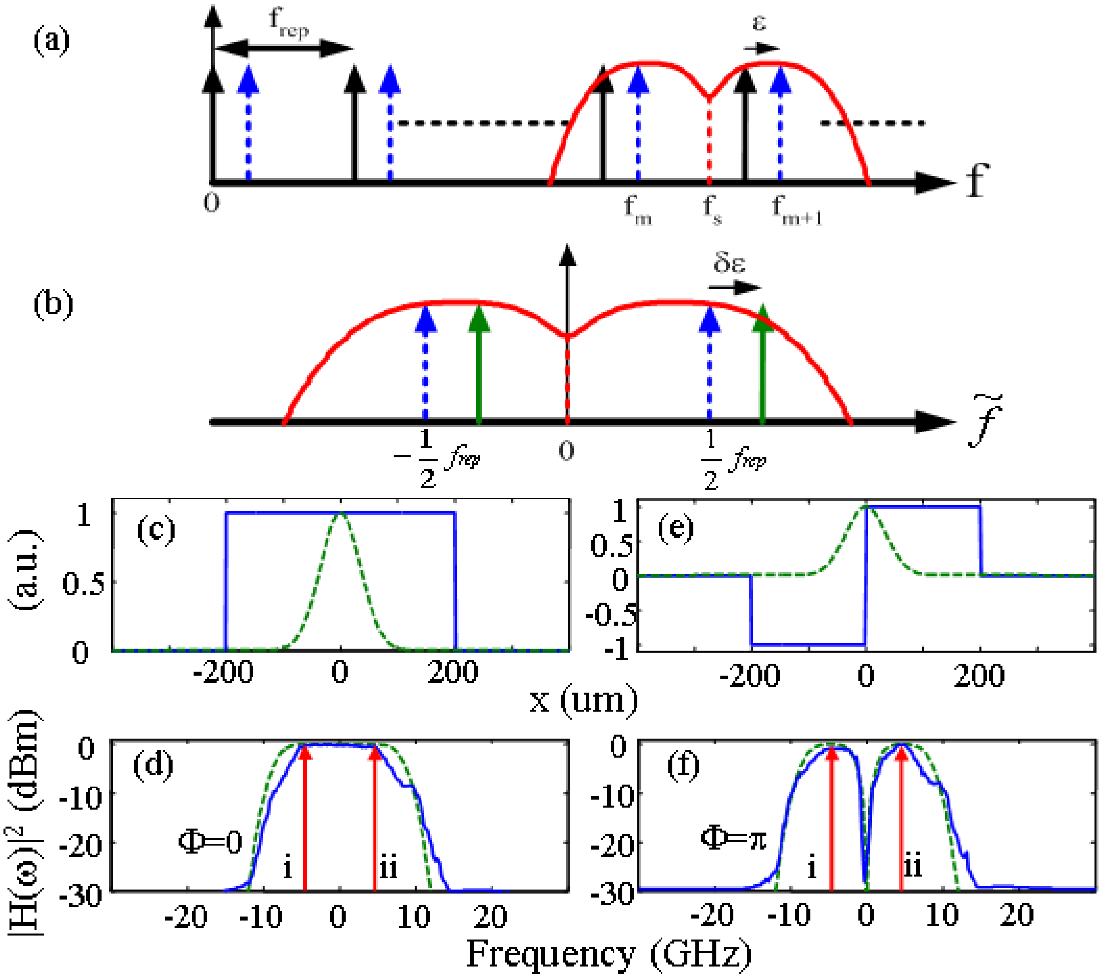

Fig. 5.3. (a) Optical comb in absolute frequency position (black solid arrows) and having an offset ε (blue dashed arrows). The schematic filter function is shown in red. (b) Two spectral lines selected by the pulse shaper are plotted against relative frequency after aligning the LCM (no additional offset: blue dash; with additional offset of δε: green solid). Mask function (solid line) and Gaussian intensity profile with radius w_0=75um (dashed line) for Φ=0 (c) for both lines and for Φ=π (e) to one line. Resulting 4-pixel pass-band filter function $|H(\omega)|^2$: (d) experimental (solid line) result by sweeping the wavelength of a CW laser and simulated (dashed line) for Φ=0; (f) experimental (solid line) and simulated (dashed line) for Φ=π. The arrows schematically indicate the comb line positions.

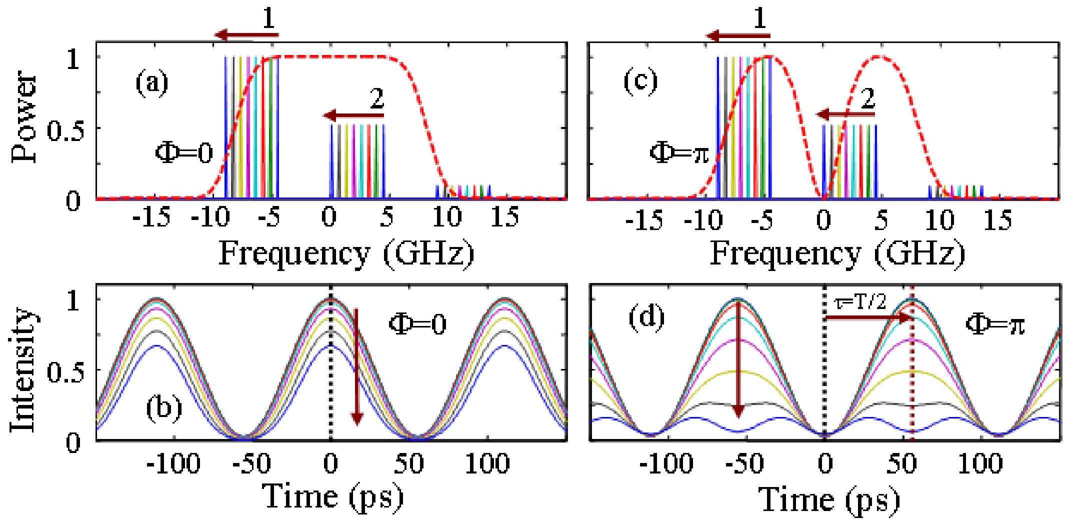

Fig. 5.4. Fit to Fig. 2 using the frequency-domain model. (a, c) Spectra fit (linear scale) for δε of {0, 7, 14, 21, 28, 35, 42 and 49}%. The arrows indicate the initial line positions and the direction of detuning. Experimental time-domain traces for corresponding frequency offsets are shown for Φ=0 (b) and Φ=π (d). The arrows indicate intensity peak variations associated with these frequency offsets. Delay positions are marked by dashed lines.

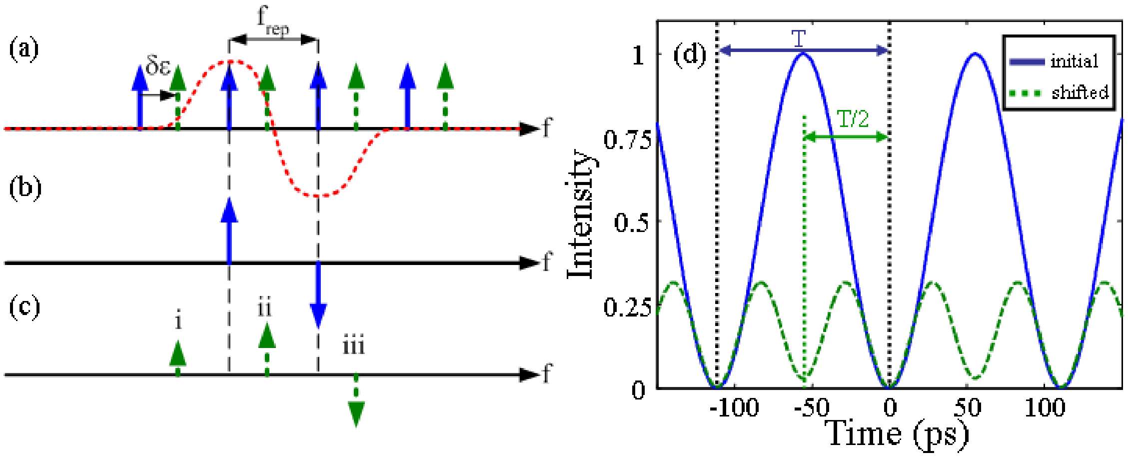

Fig. 5.5. Schematic of the concept of periodicity conversion due to shifting of the optical frequency comb when a phase shift is applied to one comb line. (a) Initial and the shifted frequency comb with fixed line amplitudes depicted by 4 arrows (solid: initial; dashed: shifted). The filter function is shown in red dashed line. (b) Filtered comb without frequency shift. (c) Filtered comb with a large frequency shift. (d) Simulated time-domain results showing periodicity conversion: from initial comb without frequency shift (solid) and the shifted comb (dash).

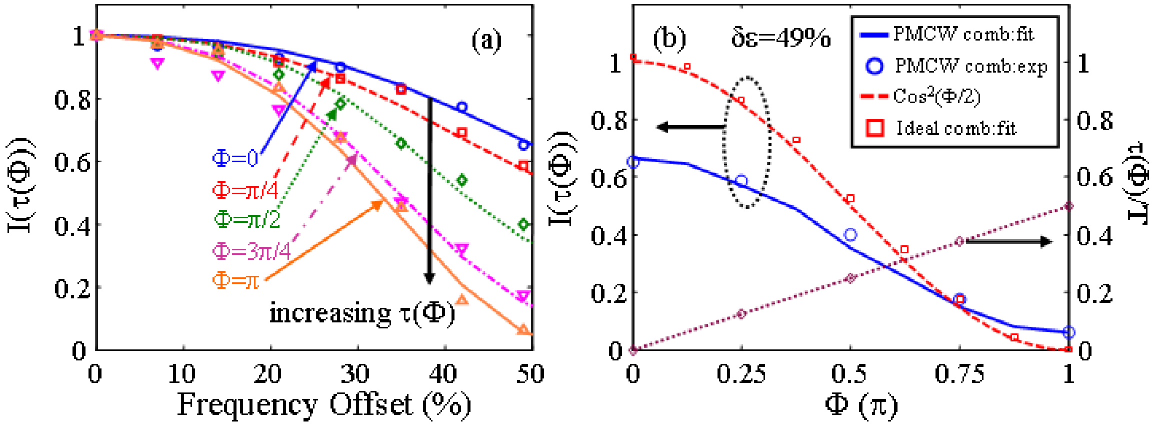

Fig. 5.6. (a) Experimental (symbols: Φ= {0, π/4, π/2, 3π/4 and π}) and calculated (lines: Φ= 0 to π in π/4 increments) waveform amplitudes at corresponding τ(Φ) for δε of {0, 7, 14, 21, 28, 35, 42 and 49}%. (b) Intensity values for 49% frequency offset at corresponding τ(Φ) for different Φ values using phase-modulated CW comb (blue circle: experimental; blue solid line: calculation). Calculated (dotted line) and experimental (diamonds) τ(Φ) is also included. Intensity values assuming ideal comb lines (red square) is plotted with $\cos^2(\Phi/2)$ (red dashed line).

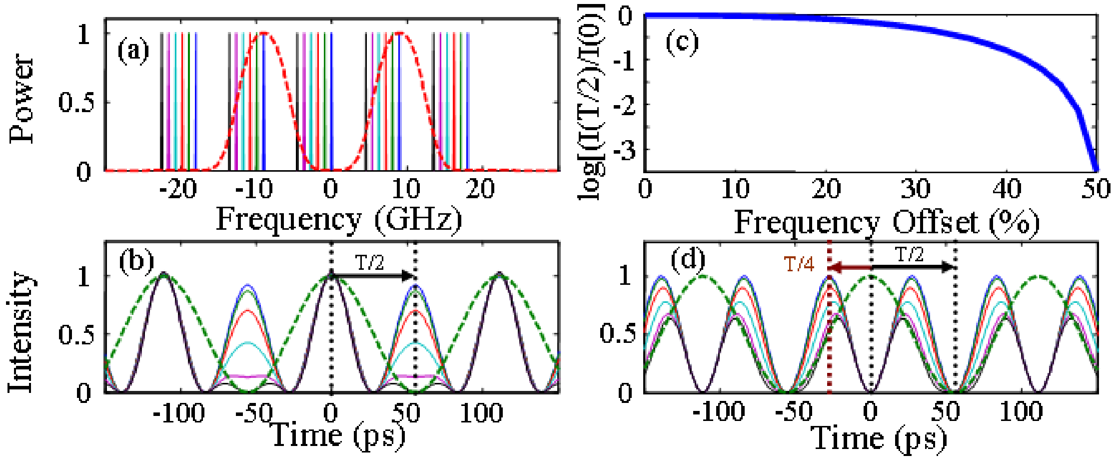

Fig. 5.7. Two lines selected at $2f_{rep}$ by blocking the center line. (a) Ideal comb lines shifted with δε {0-50}% in 10% increment with no phase control. (b) Resulting time-domain intensity: peak at time zero is stable while peak at time T/2 is sensitive to offsets. (c) Semi-log plot of I(T/2)/I(0). (d) Ideal comb lines shifted with offsets {0-50}% in 10% increment with Φ=π to one line. In (b, d), green dashed lines depict $\cos^2(\pi f_{rep} t)$.

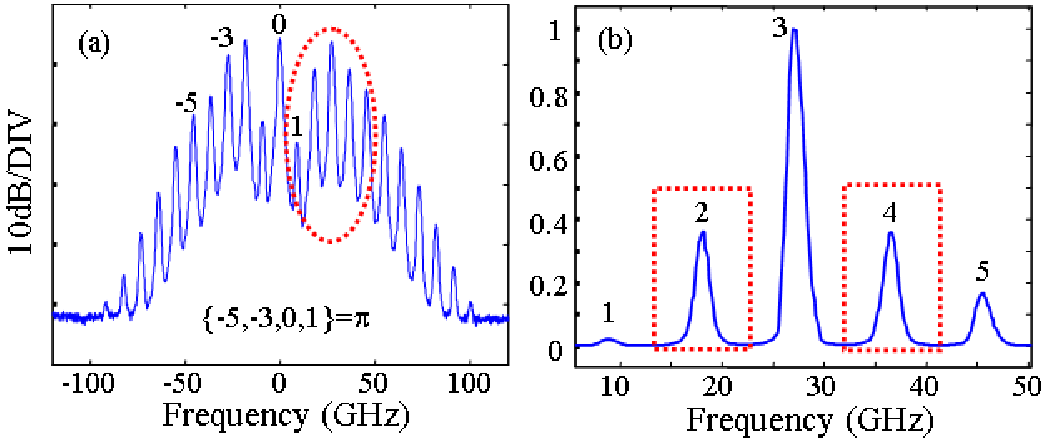

Fig. 5.8. (a) Spectrum obtained from a low V_π phase modulator. Circled spectral portion is expanded in (b), in linear scale and normalized to line {3}. Lines {2, 4} are selected by the line-by-line shaper while the others are suppressed.

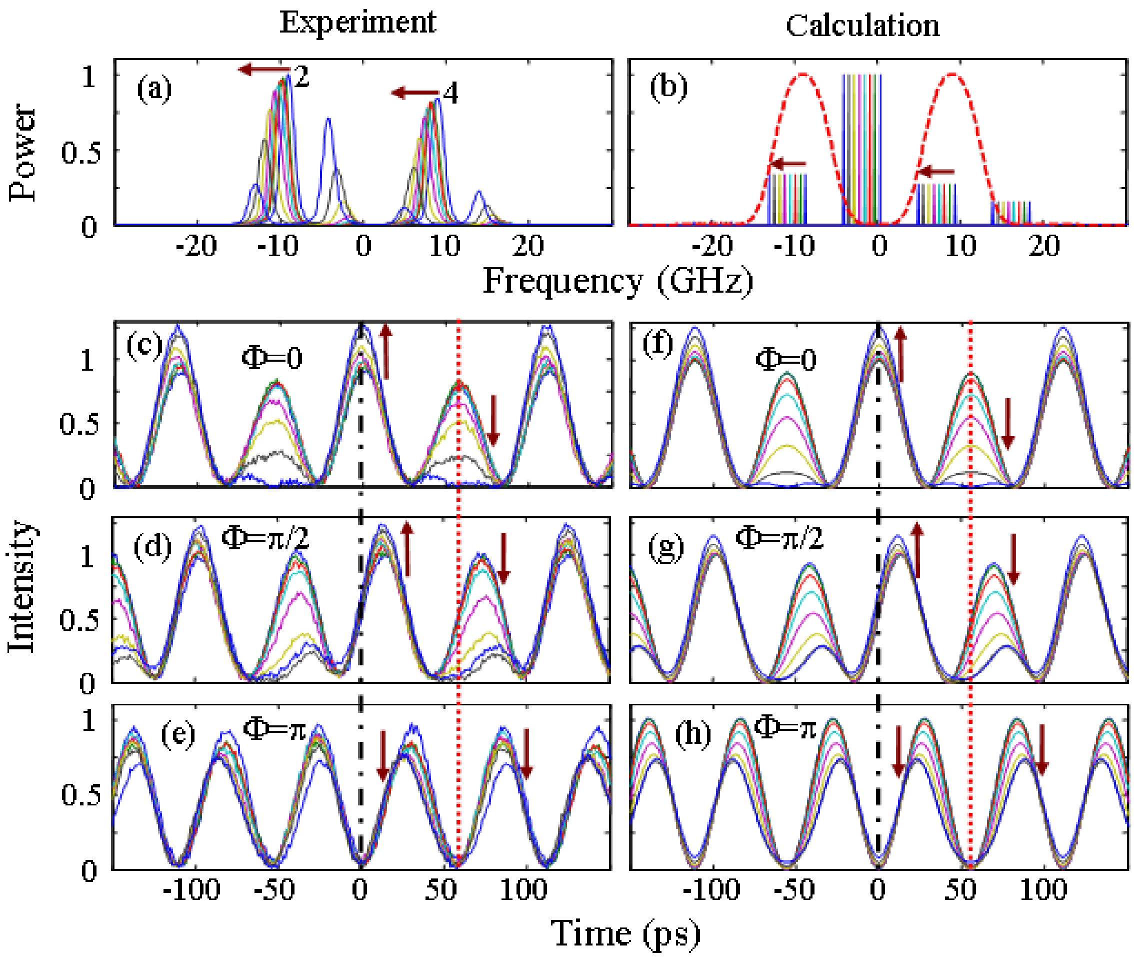

Fig. 5.9. (a, b) Experimental spectra and the lines used for calculation (linear scale) for two lines with spacing of 2f_{rep} with δε of {0, 7, 14, 21, 28, 35, 42, and 49}%. The horizontal arrows indicate the initial line positions and the direction of detuning. (c-e) Experimental time-domain waveforms for Φ={0, π/2, and π}, respectively. (f-h) Calculated time-domain waveforms for Φ={0, π/2, and π}, respectively. The vertical arrows indicate intensity variations as the optical frequency offset increases for different temporal positions. Temporal positions: dash-dot: zero delay; dashed: T/2.

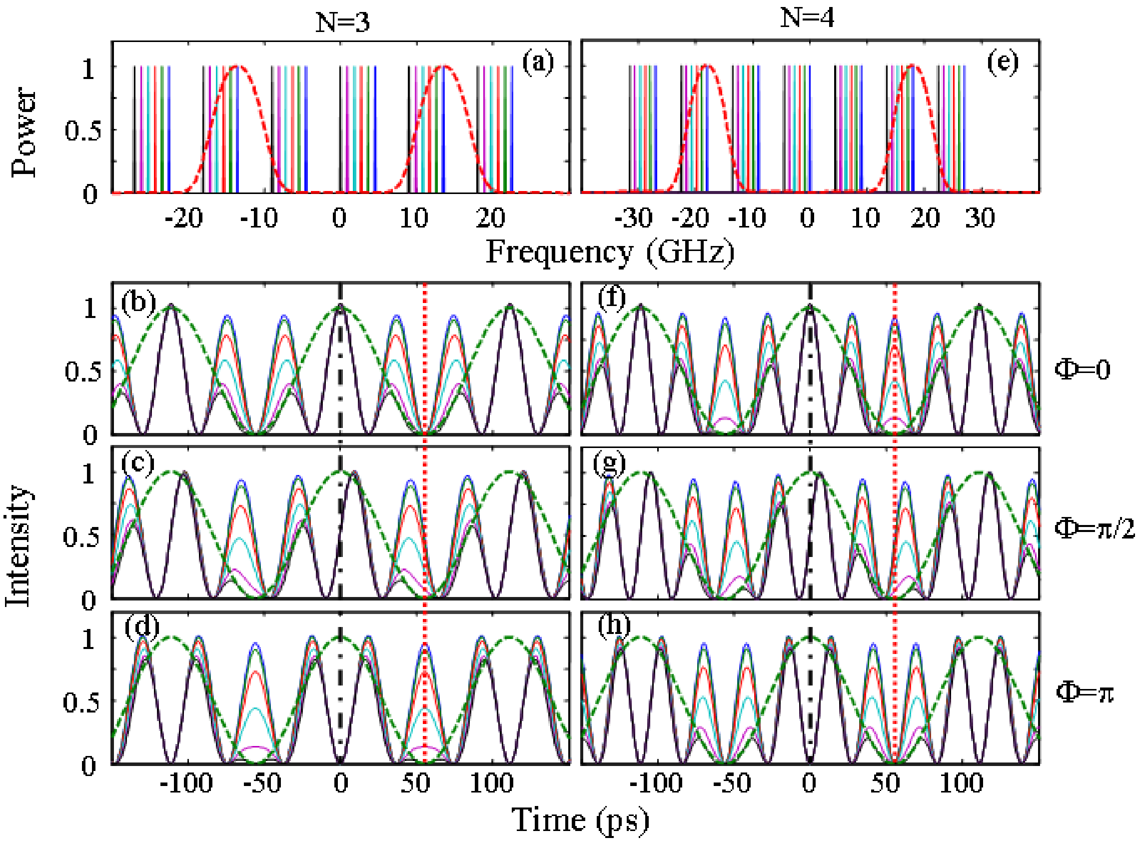

Fig. 5.10. Simulation spectra for two lines with N=3 (a) and N=4 (e) with δε of {0-50}% in 10% increments. Resulting time-domain waveforms are given for N=3 (b-d) and N=4 (f-h) with phase shifts applied to one line Φ={0, π/2, π}, respectively. Green dashed lines depict $\cos^2(\pi f_{rep} t)$. Temporal positions: dash-dot: zero delay; dashed: T/2.

6. QUANTITATIVE STUDY OF OPTICAL FREQUENCY NOISE TO INTENSITY NOISE CONVERSION IN LINE-BY-LINE PULSE SHAPING

In this chapter, the impact of time-varying optical comb frequency variation on line-by-line shaped waveforms is investigated. Time-varying optical comb frequency drift (which can be viewed as effective frequency comb linewidth broadening) is experimentally accomplished by providing a sinusoidal dithering to the continuous-wave laser wavelength, which is then sent to a optical phase modulator. Optical comb frequency noise to waveform intensity noise conversion is examined using an electrical spectrum analyzer. A theoretical model is developed. An effective numerical algorithm is explained. Two simple line-by-line shaping examples are investigated in detail. In one case, only a single line is selected and in the other case, two lines are selected by skipping one intermediate line. Experimental results are in good agreements to our theoretical predictions. The effect of pulse shaper parameters in intensity noise generation under offset frequency variation is also discussed.

6.1 Introduction

In line-by-line shaping, the spectral resolution of a shaper is made finer than the repetition frequency, leading to shaped waveforms extending throughout the full time period between initial input pulses. As a consequence of line-by-line shaping, waveform contributions from overlapping adjacent pulses interfere coherently, resulting in a new source of time-domain waveform noise sensitive to variations in the comb offset frequency [9,10].

Mode-locked lasers generating combs of stabilized frequency lines have resulted in revolutionary advances in optical frequency metrology [2] and optical carrier-envelope phase control [1,65]. However, these self-referenced mode-locked lasers typically operate at repetitions rates of ~1 GHz and below, with line spacing too narrow for most pulse shapers to cleanly resolve. Frequency combs from high repetition rate sources such as harmonically mode-locked lasers often suffer from frequency instabilities, which lead to serious pulse shaping noise in line-by-line pulse shaping [9,10]. Frequency combs generated via phase modulation of a continuous-wave laser [5,13,66] have also been employed in line-by-line pulse shaping experiments [6,15,16,30,67]. Usually such phase-modulated continuous-wave (PMCW) combs offer offset frequency stability intermediate between that of self-referenced mode-locked lasers and harmonically mode-locked lasers. In general, characterization of waveform noise induced due to fluctuations of the comb offset frequency, and understanding of the resulting requirements for the frequency stability of the source, become important issues in line-by-line pulse shaping.

In the previous chapter, we performed a quantitative investigation of waveform changes in line-by-line pulse shaping induced due to *static* shifts of the optical comb frequency offset [10]. Relatively large static frequency offsets (up to 50%) were intentionally introduced, so the impact on the generated time-domain waveforms could be clearly observed using a sampling oscilloscope. Our results showed that the amplitude of waveform changes due to optical frequency shifts at the input to a line-by-line shaper depends on the temporal position within the output waveform.

Here we perform a quantitative study of noise induced in line-by-line pulse shaping in response to ***time-varying*** or ***dynami****c* changes in the comb frequency offset. In particular, we dither the comb offset frequency to controllably broaden the bandwidths of comb lines to values between 0.1% and 10% of the comb spacing. In this scheme the frequency variations of different comb lines are completely correlated. This situation is relevant for lasers that are locked in repetition rate but not in offset frequency, such as most harmonically mode-locked lasers. The effect of such dynamic optical frequency shifts is characterized by measuring the resulting RF spectra via an electrical spectrum analyzer (ESA). We also develop a computational methodology which reliably and quantitatively predicts the observed RF spectra as a function of synthesized optical linewidth. Our work provides a link between the variance of the comb offset frequency and the resulting variance introduced in the time-domain waveforms after line-by-line pulse shaping.

The remainder of this chapter is organized as follows. In Section II, we discuss two very simple line-by-line pulse shaping examples that will be studied in our frequency dithering experiments. In Section III, we describe our experimental setup and measurement system limitations. Section IV presents a simple theoretical model for the RF power spectrum induced by optical frequency fluctuations and describes a numerical method whereby RF spectra may be computed quantitatively. In Section V experimental RF spectra are presented and compared to the calculations. This section includes some discussion of the effect of the pulse shaper spectral resolution on the induced waveform noise.

6.2 Test waveforms

Two simple line-by-line pulse shaping operations sensitive to the frequency comb offsets are illustrated in Fig. 6.1 [10,15]. Figure 6.1(a) schematically depicts filtering of a single line from an optical frequency comb with lines spaced by repetition frequency f_{rep}, while Fig. 6.1(b) depicts selection of two lines with one intermediate line blocked and with an adjustable relative phase Φ applied to one of the selected lines. The frequency positions of the comb lines can be expressed as [65]

$$f_m = mf_{rep} + \varepsilon + \delta\varepsilon(t) \tag{6.1}$$

where m are large integers, ε denotes a static comb frequency offset, and $\delta\varepsilon(t)$ is an additional time-varying offset frequency introduced in our experiments. As explained in [17], only the relative frequency offset relative to the features of the pulse shaping mask will be important for this investigation. In Fig. 6.1(a, b), the corresponding shaper filter functions are shown as the dotted traces. The center frequency f_s (dashed line) of the filter function serves as a frequency reference. Figures 6.1(c, d) show calculated time-domain intensity waveforms for single-line and two-line filtering (Φ=0) cases, respectively, with static comb offsets of {0-20}% in 10% per increment. The calculation method will be described in Section III and is also reported in detail within Ref. [10].

For single-line filtering shown in Fig. 6.1(a, c), the waveforms evolve from a constant intensity CW signal to a strongly modulated waveform under comb frequency offset. For the two-line filtering at $2f_{rep}$ case shown in Fig. 6.1(b, d), the waveform initially consists of two equal intensity peaks per f_{rep} period (it is periodic at 2 f_{rep}), but under increasing frequency offset one of the two pulses per period loses intensity. The phase of one of the lines can be shifted by a controllable amount Φ to allow further investigations on noise contributed through pulse shaping. In both cases the waveforms vary most strongly at temporal positions where adjacent input pulses provide equal contributions and hence interference most effectively. This occurs exactly between the original pulses (at ±T/2), consistent with previous experimental observations [9]. Note that ideally both optical intensity waveforms should have no corresponding f_{rep} frequency component in their RF spectra when the frequency offset is zero. Hence one may expect the RF spectra in the vicinity of f_{rep} to respond sensitively to either static frequency offsets or a time-varying frequency dither introduced in our experiments. In practice, both finite extinction ratio and finite spectral resolution in the pulse shaper lead to a finite amplitude for the f_{rep} harmonic in the RF spectrum even without frequency offset or dither. Nevertheless, investigation of these simple waveforms will provide new and quantitative insight into time-dependent pulse shaping noise introduced through fluctuations of the comb offset frequency.

6.3 Experimental setup

Figure 6.2(a) shows the schematic experimental setup. A 1 kHz linewidth CW laser (Koheras Adjustik) with intra-cavity PZT is phase-modulated by a lithium niobate phase modulator (PM: 12.5 GHz bandwidth, V_π ~5V at 10 GHz) driven at repetition frequency f_{rep}=9.15 GHz (~0.91 V_π peak to peak) by the clock signal from a bit-error-rate test (BERT: Agilent N4901B). The driving frequency is set to precisely map the spectral line spacing of the resultant frequency comb to the pixel spacing of the pulse shaper. A sinusoidal signal is used to provide controllable comb linewidth broadening $\delta\varepsilon(t)$ with dithering frequency f_d=10 kHz. The resulting PMCW comb is sent to a reflective 9.15 GHz line-by-line shaper, much as described in detail within Ref. [15]. Discrete comb lines are diffracted by the grating and focused by a lens with 1000 mm focal length. A 2×128 pixel liquid crystal modulator (LCM) array is placed just before the lens focal plane to independently control both amplitude and phase of individual spectral lines. A mirror is placed at the minimum focusing plane, leading to double-pass geometry, with all the spectral lines recombined into a single fiber and separated from the input via an optical circulator. Amplitude manipulation is realized by LCM control and the polarization extinction of the polarization beam splitter (PBS) in the recombination path back into the collimator.

For a grating based free-space pulse shaper, the effective frequency-domain filter function $H(\omega)$ that characterizes its response as a linear filter can be obtained by convolving the programmable spatial masking function $M(x)$ defined by the LCM with the Gaussian intensity profile of a single optical frequency beam

$$H(\omega)=\left(\frac{2}{\pi w_0^2}\right)^{1/2}\int M(x)e^{\frac{-2(x-\alpha\omega)^2}{w_0^2}}dx \tag{6.2}$$

where w_0 is the Gaussian beam radius (half-width at $1/e^2$ of intensity) and α is the spatial dispersion with units cm $(\text{rad/s})^{-1}$ [7]. In the experiment the frequency lines have a 9.15 GHz spacing, with each line having a Gaussian spatial profile of radius w_0=95 μm. Each LCM pixel has a 100 μm width and a corresponding frequency span of 4.575 GHz; therefore frequency lines are centered on every second LCM pixel. Our line-by-line shaper has α=3.60e-13 cm $(\text{rad/s})^{-1}$ and a full-width at half maximum spectral resolution of 5.31GHz. The spectral resolution is limited here by the width of turning on one single

LCM pixel. Such resolution ensures observation of temporal overlapping contributions from adjacent pulses. After pulse shaping, optical intensity is converted to photo-current by a 20 GHz photo-detector and measured using a 50 GHz bandwidth sampling scope and an electrical spectral analyzer

Figures 6.2(b-d) show optical spectra obtained without frequency dithering using an optical spectrum analyzer (OSA: Ando 6317B) with 0.01 nm resolution. Fig. 6.2(b) shows the resulting PMCW comb spectrum without any intensity/phase control from the shaper. The comb lines used in this chapter are highlighted by the dashed square and numbered from -2 through 2. Comb line frequencies are defined relative to the CW laser frequency, marked by the arrow. All the lines between -2 and 2 are in phase, except for line [-1] which is shifted by π, as measured using the method reported in Ref. [17]. Filtered comb lines are shown using bold traces in Fig. 6.2(c, d). $|H(\omega)|^2$ (dotted traces) are experimentally acquired using an amplified spontaneous emission (ASE) source as input to the shaper. Fits to $|H(\omega)|^2$ to (solid traces) based on Eqn. (6.2) are also plotted for both cases. Figure 6.2(c) shows the experimental spectrum of single-line filtering (only line [1] selected). Fig. 6.2(d) shows the two-line filtering at $2f_{rep}$ case, where lines [-1] and [1] are selected by the shaper and with line [0] suppressed. In Fig. 6.2(c, d), the small imperfectly suppressed lines are due to the finite power extinction ratio (~20 dB). In our experiments, two razor blades are used to block the deselected spectral portions from both ends for improved power extinction ratio (> 30dB). Finite power extinction ratio is governed by two main parameters: w_0 and the polarization extinction ratio of the shaper. This is more apparent in Fig. 6.2(d), where the suppression of line [0] is limited by 20 dB. In fitting for experimental $|H(\omega)|^2$, finite extinction ratio is taken into account by making M(x)=0.1 (-20 dB in power) for pixels controlling line [0]. The effects of these unsuppressed peaks on our waveform measurements will be discussed in later sections.

The effective width broadening of the comb lines in our experiments are achieved by applying an amplified sinusoidal signal from a function generator at f_d=10 kHz dithering frequency to the intra-cavity PZT of the CW laser. We controllably broaden the comb lines through the relation

$$\delta\varepsilon(V,t) = A_d(V)\sin(2\pi f_d t) \tag{6.3}$$

where A_d is the maximum frequency dithering amplitude, V is the root-mean-square voltage of the applied sinusoidal signal in volts, controlled through varying the gain of a linear electrical amplifier. Measurement of the linewidth broadening is performed using a conventional heterodyne beating setup [57]. The dithered CW laser field is combined through an optical coupler with a second CW laser field (HP 81680A, linewidth of 16 MHz). Beat signals are detected using a 20 GHz bandwidth photo-detector (DET) and measured with an electrical spectrum analyzer (ESA: Agilent 8565EC with 30Hz-50GHz) in maximum-hold function for 30 seconds. Figure 6.3(a) shows the heterodyne beating results for 6 and 30 volts (rms) applied to the PZT of CW1, resulting in total linewidth broadening ($2A_d$) of 0.21 and 1.08 GHz, respectively. The $A_d(V)$ relation determined from the heterodyne beatings with CW2 is plotted in Fig. 6.3(b). The heterodyne results show a linear response; the effective comb linewidth broadening is determined through

$$A_d(V) = 0.018V(GHz) \tag{6.4}$$

Thus, by frequency dithering laser CW1 and then feeding it into the phase modulation setup, we are capable of controllably and simultaneously broadening all the comb lines for a PMCW comb.

As an example of time-dependent intensity noise introduced through frequency fluctuations (dither), Fig. 6.4 shows data acquired using the fast oscilloscope. In this example two-line filtering (lines [-1, 1] selected) is applied with a phase shift of either $\Phi=0$ or $\Phi=\pi$ applied to line [-1]. The figure consists of 50 overlaid sampling scope traces with frequency dither amplitudes of either 10% or 3%, relative to the 9.15 GHz comb spacing. Temporal delays are referenced to the cosine waveform peaks obtained by first selecting only lines [0, 1]. Ripple in the intensity of different peaks is caused by imperfect suppression of deselected lines. Note that line [-1] as generated via the phase modulation already has a π phase shift. Thus, programming the LCM $\Phi=\pi$, as in Fig. 6.4(b), corrects the phase and brings the waveform peaks to zero delay. Fig. 6.4(b) with 10% dither amplitude clearly illustrates our expectation that larger intensity noise is observed at T/2 (marked by the dashed lines) than at zero time position. As for Fig. 6.4(a), since all peaks are equally spaced from T/2 and zero, they have the same noise amplitude. Time-domain intensity noise clearly decreases when the dithering amplitude is reduced. However, reduction in noise amplitude is difficult to assess from the scope traces for dithering amplitudes less than 6%. Therefore, for more sensitive characterization of waveform noise induced through frequency dithering, in the rest of the chapter we use an ESA as our preferred diagnostic tool.

To be capable of distinguishing the optical frequency-modulation to amplitude modulation (FM-AM) noise induced through pulse shaping, one needs to know whether the laser itself generates FM-AM noise. Therefore, we calibrate our measurement system and provide direct comparisons using the following two setups: In configuration 1, the

CW laser is measured directly on an ESA after the photo-detector with variable optical attenuator in between; while in configuration 2, the CW laser is sent to the shaper with single-line filter as shown in Fig. 6.2(c) and measured. Optical power into the photo-detector is 3.5 dBm for both configurations.

Figure 6.5 shows the ESA measurements centered at dithering frequency f_d=10 kHz. Figures 6.5(a, b) show ESA traces with a dithering amplitude A_d/f_{rep}= {10, 2 and 0}%, relative to the 9.15 GHz comb spacing, for configuration 1 and 2, respectively. The system noise floor, determined with no input power into the photo-detector, is also plotted within the dithering off figures. As expected, the laser intrinsically generates FM-AM noise peaks (Fig. 6.5(a)). However in both figures, noise peaks at f_d are evidently higher for configuration 2, revealing extra noise attributed to pulse shaping effects. For closer examinations, Fig. 6.5(c) shows the noise peak values for configuration 1 (triangle) and configuration 2 (dot) along with linear fitting curves for various dither amplitudes. For dithering amplitudes of {0.4-10}%, configuration 2 gives a roughly 7.5 dB extra noise peak for all dithering amplitudes. We attribute the extra intensity peaks to the shaper filter function. To confirm this is a filtering effect, we verified the noise peak values reduce to the values of configuration 1 when no shaping is applied (unity transmission for all pixels). Data fitting reveals a 20dB/decade relation, which will be explored in the following subsections. For dithering amplitudes smaller than 0.4%, noise peaks depart from the fitting curve for both configurations. We attribute the broadening of lower parts of peaks for configuration 2 but not configuration 1 to low frequency vibrations of the mechanical parts that affect the optical coupling within our pulse shaper.

6.4 Theoretical model and numerical method

6.4.1 Theoretical model

Here we present a theoretical derivation to characterize comb frequency dither-induced noise of line-by-line shaped waveforms using an ESA. In the spirit of Ref. [63], we first define the waveform intensity as

$$P(t) = P_0(t) + P_\nu(t)\nu(t) + \delta P(t) \tag{6.5}$$

where $P_0(t)$ denotes the ideal, fluctuation-free pulse train. $P_\nu(t)$ denotes the first derivative of the waveform after the line-by-line shaper with respect to frequency fluctuation $\nu(t)$. $\delta P(t)$ denotes waveform variations due to other noise mechanisms. Here we first note that both $P_0(t)$ and $P_\nu(t)$ are periodic waveforms with a same periodicity of $T=1/f_{rep}$.

When waveform variations due to amplitude and timing jitters are also taken into account, we can express the waveform as

$$P(t) = [1 + A(t)][P_0(t - \delta T(t)) + P_\nu(t - \delta T(t))\nu(t)] \tag{6.6}$$

where $A(t)$ and $\delta T(t)$ denote the amplitude and timing jitter terms, respectively. The output detector current is obtained by convolving the waveform intensity with the impulse response function $g_{PD}(t)$ of the photo-detector

$$I_{PD}(t) = g_{PD}(t) \otimes P(t) \tag{6.7}$$

Under the assumption of a small timing jitter and when $A(t)$, $\delta T(t)$ and $\nu(t)$ are uncorrelated, zero mean functions, we can express the power correlation function of the optical waveform as

$$\begin{aligned} \langle P(t)P(t-\tau)\rangle &= [1 + \langle A(t)A(t-\tau)\rangle] \cdot [\langle P_0(t)P_0(t-\tau)\rangle + \\ &\langle P_\nu(t)P_\nu(t-\tau)\rangle\langle \nu(t)\nu(t-\tau)\rangle + \langle \dot{P}_0(t)\dot{P}_0(t-\tau)\rangle\langle \delta T(t)\delta T(t-\tau)\rangle + \\ &\langle \dot{P}_\nu(t)\dot{P}_\nu(t-\tau)\rangle\langle \nu(t)\nu(t-\tau)\rangle\langle \delta T(t)\delta T(t-\tau)\rangle] \end{aligned} \tag{6.8}$$

where the (·) represents the derivative with respect to time.

The current power spectrum with frequency dithering measured on an ESA is therefore expressed as [63]

$$\begin{aligned} \left|\tilde{I}(\omega)\right|^2 &= \left|\tilde{G}_{PD}(\omega)\right|^2 \cdot [\delta(\omega) + \left|\tilde{A}(\omega)\right|^2] \otimes [\left|\tilde{P}_0(\omega)\right|^2 + \left|\tilde{P}_\nu(\omega)\right|^2 \otimes \left|\tilde{\nu}(\omega)\right|^2] \\ &\otimes [\delta(\omega) + \omega^2\left|\delta\tilde{T}(\omega)\right|^2] \end{aligned} \tag{6.9}$$

Here $\otimes$ denotes convolution. $\tilde{G}_{PD}(\omega)$, $\tilde{P}_0(\omega)$, $\tilde{P}_\nu(\omega)$, $\tilde{\nu}(\omega)$ and $\delta\tilde{T}(\omega)$ denote the base-band frequency response of $G_{PD}(t)$, $P_0(t)$, $P_\nu(t)$, $\nu(t)$ and $\delta T(t)$ obtained through the Fourier-Transform relation, respectively.

Disregarding the term with the products of $\left|\tilde{A}(\omega)\right|^2$ and $\left|\delta T(\omega)\right|^2$, we obtain

$$\begin{aligned} \left|\tilde{I}(\omega)\right|^2 &= \left|\tilde{G}_{PD}(\omega)\right|^2 \cdot \{\left|\tilde{P}_0(\omega)\right|^2 + \left|\tilde{P}_\nu(\omega)\right|^2 \otimes \left|\tilde{\nu}(\omega)\right|^2\} \\ &\otimes \{\delta(\omega) + \left|\tilde{A}(\omega)\right|^2 + \omega^2\left|\delta\tilde{T}(\omega)\right|^2\} \end{aligned} \tag{6.10}$$

At this point we provide several comments related to Eqn. (6.10):

(a) Both $\left|\tilde{P}_0(\omega)\right|^2$ and $\left|\tilde{P}_\nu(\omega)\right|^2$ consist of a sequence of RF harmonics at frequencies $\omega_k = k(2\pi f_{rep})$.

(b) The frequency dithering terms grow as $\left|\tilde{\nu}(\omega)\right|^2$ and thus follow a 20dB/decade scaling relation with respect to the amplitude of the frequency dithering function.

(c) Our analysis applies to a general dithering function ν(t). However, in our experiment, the frequency dithering is applied using a time-domain sinusoidal function (frequency f_d), and thus $\left|\tilde{\nu}(\omega)\right|^2$ consists of delta functions at $\omega=\pm 2\pi f_d$. Hence the frequency dithering introduces new peaks into the measured ESA spectrum at $\pm f_d$ with respect to the harmonics at kf_{rep}.

(d) We can thus quantify the waveform fluctuation due to frequency offset variation by introducing the normalized variance as

$$\frac{\left\langle [P_\nu(t)\nu(t)]^2 \right\rangle}{\left\langle P_0^2(t) \right\rangle} = \frac{\int \left|\tilde{P}_\nu(\omega) \otimes \tilde{\nu}(\omega)\right|^2 d\omega}{\int \left|\tilde{P}_0(\omega)\right|^2 d\omega} \tag{6.11}$$

Assuming negligible (or separable) amplitude and timing jitter, the normalized variance can be obtained through the photocurrent power spectrum by the following notation

$$\frac{\left\langle [P_\nu(t)\nu(t)]^2 \right\rangle}{\left\langle P_0^2(t) \right\rangle} = \frac{\sum_k [\int_{\omega_k-\delta\omega_{\max}}^{\omega_k-\delta\omega_{\min}} + \int_{\omega_k+\delta\omega_{\min}}^{\omega_k+\delta\omega_{\max}}]\left|\tilde{I}(\omega)\right|^2 d\omega}{\sum_k \int_{\omega_k-\Delta\omega_{RB}}^{\omega_k+\Delta\omega_{RB}} \left|\tilde{I}(\omega)\right|^2 d\omega} = \frac{\sum_k \mathrm{E}_{noise,k}}{\sum_k \mathrm{E}_{0,k}} \tag{6.12}$$

Here the power of the unperturbed harmonic peaks ($\mathrm{E}_{0,k}$) are integrated over the ESA resolution bandwidth ($\Delta\omega_{RB}$) for each harmonic, while the contribution to the noise power ($\mathrm{E}_{noise,k}$) are integrated over a specified frequency range between $\delta\omega_{\min}$ and $\delta\omega_{\max}$ for all harmonics. Evidently one would require $\delta\omega_{\min} \geqq \Delta\omega_{RB}$; the value of $\delta\omega_{\max}$ will depend on the highest frequency content of the dithering signal, but is evidently less than πf_{rep}. Since the waveform may change in a complicated way with offset frequency variation, we may obtain more information by looking at contributions to normalized variance from a particular harmonic (single k value at a time). In this manner we may obtain an estimate of the quantity

$$\eta_{k,p} \equiv \frac{\mathrm{E}_{noise,k}}{\mathrm{E}_{0,p} \cdot \int \left|\tilde{\nu}(\omega)\right|^2 d\omega} \tag{6.13}$$

The frequency dither induced noise associated with the kth harmonic ($E_{noise,k}$) is normalized to a desired pth (where $p \geqq 1$) harmonic peak of the unperturbed signal ($E_{0,p}$) and the variance of the offset frequency fluctuation. Thus the factor $\eta_{k,p}$ (with unit of dBc/Hz) gives the proportionality constant linking the output intensity waveform variation of the kth RF harmonic to the variance of the offset frequency, normalized to the pth RF harmonic of the shaped intensity waveform without frequency noise. This constant is actually independent of the form of the power spectral density of the frequency offset fluctuations, but does depend on harmonic number and the line-by-line shaper filter function. In the following sections we compute this constant for the special case of a sinusoidal frequency offset dithering and confirm our computations by experiments.

(e) From Eqn. (6.10), it is noted that both the harmonics of the unperturbed waveform as well as those associated with waveform derivatives with respect to frequency offset fluctuations are affected by amplitude and timing jitters in a similar way. For our special case of a single tone dithering signal, the harmonics at kf_{rep} and the dither terms arising at $kf_{rep} \pm f_d$ have the same line shape, as will be presented in Section V.

(f) Higher order terms not included in the current analysis can lead to additional noise peaks in the RF spectrum, e.g., at frequencies $kf_{rep} \pm 2f_d$, which follow a 40dB/decade scaling relation with respect to frequency dithering amplitude and so forth.

6.4.2 Numerical method

Here we explain our numerical method for calculating the ESA current power spectrum under frequency dithering. The flow of the method is outlined in Fig. 6.6(a). Our numerical approach is capable of obtaining the higher-order terms described in the previous section. First, we define two time variables: a fast time variable t (with its corresponding fast frequency denoted as ω) on the scale of pulse repetition, and a slow time variable t' (with its corresponding slow frequency denoted as ω') on the time scale of frequency dithering. Next, frequency variations within one dithering period ($T_d=1/f_d$) are numerically sampled using N+1 evenly spaced temporal points with time interval given by $\Delta t'=T_d/N$

$$\varepsilon(t'_j) \equiv A_d \sin(2\pi f_d t'_j),\ j=1,2,\ldots,N+1 \tag{6.14}$$

where $\varepsilon(t'_j)$ denotes the jth static comb frequency offset value at time $t'_j=(j-1)\Delta t'$.

Using the comb line amplitudes and filter functions obtained through fittings in Fig. 6.2(b), corresponding output fields $E_{out}(t'_j, \omega)$ for the j^{th} sampling point are derived through the relation [10]

$$E_{out}(t'_j,\omega) = E_{in}(\omega + \varepsilon(t'_j)) \cdot H(\omega) \tag{6.15}$$

The corresponding output time-domain envelope function is obtained by inverse Fourier-transforming the output field with respect to the fast frequency scale ω

$$a(t'_j,t) = \frac{1}{2\pi}\int E_{out}(t'_j,\omega)e^{j\omega t}d\omega \tag{6.16}$$

Waveform intensities are obtained by equating $I(t'_j,t)=\left|a(t'_j,t)\right|^2$. The intensities are similar to what are shown in Fig. 6.1(c, d) for each static frequency offset value ε(t'$_j$). For each $I(t'_j,t)$, Fourier-series coefficients are calculated (for the fast frequency scale) using the waveform within one period (T=1/f$_{rep}$, as shown within the dashed rectangle in Fig. 6.1(c, d)) to obtain the complex RF spectrum $\widetilde{R}(t'_j,\omega)$.

From $\widetilde{R}(t'_j,\omega)$, the complex amplitudes of each RF spectral component of interest are extracted and stored in a (N+1)xM matrix $\widetilde{V}(t',\omega)$, in such a way that the first column of $\widetilde{V}(t',\omega)$ records the DC values, the second column corresponds to f$_{rep}$, the third column corresponds to 2f$_{rep}$ and so forth. In this critical step, we physically separate the two time scales, so that the N+1 values of each column of $\widetilde{V}(t',\omega)$ thus represent the time-domain evolution of the complex amplitude of the mth harmonic of f$_{rep}$ within one dithering cycle, in the slow dithering time scale t'. Now by performing a Fourier-transform on $\widetilde{V}(t',\omega)$ with respect to t' and taking the absolute value squared, we arrive at the final current power spectrum array $|\widetilde{V}(\omega',\omega)|^2$

$$\left|\widetilde{V}(\omega',\omega)\right|^2=\left|\int\widetilde{V}(t',\omega)e^{-j\omega't'}dt'\right|^2 \tag{6.17}$$

Along the mth column, the jth value denotes the noise peak of the ESA current power spectrum separated by j(f$_d$) from m(f$_{rep}$). In order to obtain accurate results, N should be made large enough so that $I(t'_j,t)$ and $I(t'_{j+1},t)$ do not change abruptly from one to the next. Comparison among results reveal that N greater than 100 is sufficient, making our method computationally efficient and tractable. Note that our numerical method is also applicable when multiple dithering tones are present simultaneously.

Resulting calculated beat signals from {DC~2f$_d$} and {f$_{rep}$~ f$_{rep}$+2f$_d$} are shown in Fig. 6.6(b) for the single-line filtering case (experimental condition as shown in Fig. 6.2(c)) with a 10% sinusoidal dithering amplitude. Power peak values at frequencies of {f$_d$, f$_{rep}$, f$_{rep}$+f$_d$} are denoted here as {P(f$_d$), P(f$_{rep}$), P(f$_{rep}$+f$_d$)} and throughout the rest of this Chapter, respectively. The powers are normalized to P(f$_{rep}$) (p=1 in Eqn. (6.13)) and are in unit of dBc. For the ideal single-line filtering case with infinite shaper spectral resolution, the time-domain waveform should consist of a constant intensity waveform. In the current power spectrum, there should be no observable beat signals at f$_{rep}$. However due to finite power extinction of the line-by-line shaper in practice, e.g. due to finite spectral resolution, one must take the unsuppressed intensity peaks into account, resulting in a 34 dB contrast between the DC and f$_{rep}$ beat. By observation, the beat signal at 2f$_d$ is almost as large as P(f$_d$). This is not surprising: in the ideal case where comb line amplitudes and filter function are perfectly symmetric (even function) about the filter frequency center f_s, the first derivative term in Eqn. (6.8) vanishes, resulting in peaks only at even multiples of f_d. However, asymmetry caused by intrinsic variations in the line-to-line phase/amplitude of PMCW combs introduces the odd multiples of f_d experimentally. Δ_1=11.93 dB denotes the power ratio between $P(f_{rep})$ and $P(f_{rep}+ f_d)$ with a 10% dither amplitude. Figure 6.6(c) shows the simulation results of $P(f_{rep}+ f_d)$ and $P(f_{rep})$ against different dithering amplitudes, normalized to $P(f_{rep})$ value with 10% dither amplitude. $P(f_{rep})$ remains nearly constant. The prediction of a 20dB/decade variation in $P(f_{rep}+ f_d)$ from our theoretical model and experimental results in Fig. 6.5(c) are confirmed. From this 20dB/decade relation, we can find the factor $\eta_{1,1}$ for this shaping example by using the relation $\eta_{1,1} = -\Delta_1 - 20 \cdot \log(915 MHz)$ and obtain a value of -191.16(dBc/Hz).

These simulations are carried out using our current experimental pulse shaper parameters. We note here that specific values obtained for the dither-induced noise peaks will depend on the pulse shaper parameters, namely LCM pixel spacing and the spectral resolution. If desired, our model can be applied to predict other pulse shaper settings by simply changing the masking function and spectral resolution as defined in Eqn. (6.2).

6.5 Experimental results and discussions

6.5.1 Single-line filtering

We first examine the validity of our numerical model with only line [1] selected. Figure 6.7 shows the results with dithering amplitude of 10%, and average optical power of -1.5 dBm into the photo-detector. ESA measurements of $P(f_d)$, $P(f_{rep})$ and $P(f_{rep}+ f_d)$ are shown in Fig 6.7(a) and Fig. 6.7(b), respectively. Calculated noise peak values shown in Fig. 6.6(b) are normalized to experimental $P(f_{rep})$ value. Experimental and calculated noise peak values are given within the figures and are in good agreement. Experimentally, a Δ_1 (ratio between $P(f_{rep})$ and $P(f_{rep}+ f_d)$) value of 10.64 dB is obtained, in close agreement to the calculated value of 11.93 dB. The slight discrepancy can be attributed to the non-symmetry of the experimental filter function.

Comparing Fig. 6.7(a) with Fig. 6.7(b), a clean spectrum is obtained in Fig. 6.7(a), while there are numerous extra noise peaks observed in Fig. 6.7(b). Fig. 6.7(c) shows maximum hold traces with 10% dithering amplitude, dithering turned off, and the system noise floor. The trace with dithering off reveals the extra noise pedestals are due to amplitude and timing jitter, which we attribute to the BERT driving the phase modulator. As derived in Eqn. (6.10) and following the discussion point (e) therein, one should thus expect the dithering noise peak $f_{rep}+f_d$ to show the same line shape as the f_{rep} beat. This point is indeed justified within both Figs. 6.7(b, c).

Figure 6.8 shows the experimental results (symbols) of $P(f_d)$, $P(f_{rep})$ and $P(f_{rep}+ f_d)$ values for various dithering amplitudes along with calculated results (lines) using our numerical method. For these data, the span of the ESA is 300 Hz with RBW of 3Hz. Noise peak values are averaged from 20 acquisitions, each with a sweep time of 10 seconds. Experimental results are in nice agreement to our calculations. We first note that $P(f_{rep})$ remain nearly a constant throughout, thus Δ_1 provides a direct measure of comb frequency dither amplitude. From the results of $P(f_d)$ and $P(f_{rep}+ f_d)$, experimental data are consistent with the 20 dB/decade relation, as anticipated for A_d/f_{rep} above 0.4%. In our experiment, the effect of the comb frequency dithering can be directly discerned down to 36.6 MHz (0.4%) dither amplitude. From the 20 dB/decade relation, we may extrapolate to predict the noise contribution from smaller frequency variations.

6.5.2 Two-line filtering at $2f_{rep}$

In contrast to the single-line filtering case, where only intensity control is applied by the shaper, here we extend our investigation to the impact of frequency-dithering on line-by-line {intensity + phase} shaped waveforms. In this part we show our experimental results with lines [-1 and 1] selected. In different experiments, the phase of line [-1] is controlled by the line-by-line shaper with values $\Phi=\{\pi, \pi/2, 0\}$. Measurement settings are the same as for the single-line filtering case, but with an input average optical power of 1.0 dBm into the photo-detector. To better prove the validity of our theoretical model, Table I summarizes the experimental and calculated noise peak values, with dithering amplitude of 10%. Calculated peak values are normalized to the experimental peak value at $2f_{rep}$. Excellent agreements are reached between the three experimental and calculation data sets. The peaks at frequencies $\{f_d, f_{rep}, f_{rep}+f_d, 2f_{rep}$, and $2f_{rep}+f_d\}$ are given. Δ_1, and Δ_2 denote the contrast ratios between the peaks at f_{rep} to $f_{rep}+f_d$ and $2f_{rep}$ to $2f_{rep}+f_d$, respectively.

Using the results shown in Table 6.1, we observe the following: From the contrast ratios $\{\Delta_1, \Delta_2\}$, one can grasp how susceptible the waveforms are to frequency dithering and to a good extent how the waveforms evolve. The larger the noise peaks and the smaller the contrast, the greater the impact the frequency dither has on that particular RF frequency component. For example, for all three phase values, Δ_2 is greater than 35dB, while Δ_1 values are on the order of 13~18 dB. The actual noise peak values at $f_{rep}+f_d$ varies by 12.30 dB as phase control value Φ is changed from π to 0. This indicates that the waveforms tend to undergo a repetition rate change from the initial $2f_{rep}$ waveform to a f_{rep} waveform periodicity, with this tendency exhibited most strongly for $\Phi=\pi$ phase control. This can be attributed to the field contribution from line [0], which participates in the waveform generation with a weighting that depends on the frequency dithering amplitude. This finding is consistent with our previous report [10]. It is evident that the phase control has significant impact on the RF peaks at f_{rep} and $f_{rep}+f_d$, but not on the other peaks. This is highlighted using the bold frame within Table 6.1. These results are in good accord to the qualitative predictions provided by our time-domain picture in Ref. [9]. The linkage is elaborated in the following paragraph.

To support our arguments, Fig. 6.9 shows the experimental ESA measurements over frequency ranges $\{f_{rep} \sim f_{rep}+f_d\}$ with 10% dithering amplitude for the three phase control values. Corresponding calculated intensities and the magnified intensity peaks with {0 (solid), 10 (dotted)}% static frequency shifts are plotted. From our time-domain picture (static shift analysis), we anticipate greater intensity variations (waveform noise) showing up at T/2 points compared to 0 and T points. From the figures showing the magnified peaks, this point is indeed well taken. The $\Phi=\pi$ case (Fig. 6.9(a)) shows the decreased peaks at odd multiples of T/2 but stationary peaks at 0 and T, contributing to a stronger f_{rep} RF component when dithering is on. Thus the dithering result yields a largest noise peak value at $f_{rep}+f_d$, indicating that this waveform is most susceptible to frequency dither and the change in waveform is most sensitive in its f_{rep} RF component. For $\Phi=0$ case (Fig. 6.9(c)), calculated intensity with 10% static frequency shift show all the peaks are equally decreased, since the intensity peaks are displaced an equal distance between 0 and T/2. The f_{rep} RF harmonic of this waveform is therefore less prone to frequency dithering, so the noise peaks at $f_{rep}+f_d$ is 12.30 dB less as compared to the $\Phi=\pi$ case.

The relationships of $P(f_{rep}+f_d)$ against dithering amplitudes with different phase controls are conducted using the same method as for one-line filtering case, shown in Fig. 6.10(a). Experimental data are shown using symbols while calculated values are shown using lines. The experimental data for both $\Phi=\{\pi$ and $\pi/2\}$ fit the 20 dB/decade scaling all the way down to 0.2% dither and show ~3 dB difference caused by phase control. For $\Phi=0$, the experimental data adhere to the theoretical line only between {1-10}% with a ~13 dB difference compared to $\Phi=\pi$ case, but deviate from the ideal curve for smaller dithering amplitudes. This finding is confirmed with multiple attempts. Possible reason is that for $\Phi=0$ case, beat signals are much lower than the other two phase values, leading to more vulnerability to system limitations. For $\Phi=\pi$ and $\pi/2$ cases, the achieved sensitivity of 0.2% is better than the single-line filtering case. Note that the waveform design with $\Phi=\pi$ (corresponding to the proposed waveform shown in Fig. 6.1(d), with π intrinsic phase of line [-1] compensated by the shaper) is predicted to yield high sensitivity for monitoring of frequency fluctuation [10]. This is verified by our experiments. Using the definition in Eqn. (6.13) and our data values, we can obtain $\eta_{1,2}$ of {-205.02, -208.21, -217.22}(dBc/Hz) and $\eta_{2,2}$ of {-214.37, -214.55, -216.61}(dBc/Hz) for phase values $\Phi=\{\pi, \pi/2, 0\}$, respectively.

Now we investigate the effect when a static comb frequency bias ε_b is provided. Comb line frequencies relative to the filter function are now

$$\widetilde{f}_m = (m - m')f_{rep} + \varepsilon_b + \delta\varepsilon(t) \tag{6.18}$$

where $m'f_{rep}$ is the frequency of PMCW comb line [0] that is aligned to the center of the shaper filter function. In practice, ε_b is provided by mounting the LCM on a translational stage and shifting it (and thus the filter function) perpendicular to the optical axis.

Fig. 6.10(b) shows the relationship of $P(f_{rep}+f_d)$ against different A_d using two-line filtering with $\Phi=\pi$ applied to line [-1] as an example. Experimental data are shown with symbols for ε_b of {0, 20, and 30}% along with theoretical values shown using lines. All experimental data show a 20 dB/decade relation to varying A_d. $P(f_{rep}+f_d)$ is offset vertically by 5.5 dB and 9.6 dB for bias values of 20% and 30%, respectively, relative to the case of zero bias. With a 30% frequency bias, our data match the simulation results down to 0.12% frequency dither (10.98 MHz).

6.5.3 Effects of shaper parameters

Up to this point we have focused on results for a pulse shaper with pixel spacing corresponding to 4.575 GHz at a 2.6 GHz optics limited spectral resolution, corresponding to the parameters of our line-by-line pulse shaping experimental apparatus. It is worth noting that the amplitude of pulse shaping intensity noise induced by a certain level of offset frequency fluctuations depends on the specific pulse shaping filter function. This in turn depends both on the masking function programmed into the pulse shaper and the spectral resolution of the pulse shaper optics. In this part, we wish to provide further discussions on how shaper parameters affect the measurement results using our numerical method. The shaper parameters under concern are power extinction ratio and shaper spectral resolution. As shown in Eqn. (6.2), finite extinction ratio is incorporated through nonzero M(x); while shaper spectral resolution is dominated by two factors: (1) the width of the LCM pixel (w_p), which determines the discreteness of M(x); and (2) the minimum spot radius w_0 at the focal plane. Better spectral resolution is achieved by having smaller w_0 and w_p. Again we use two-line filtering with $\Phi=\pi$ case to accommodate our investigations.

Figure 6.11 shows the first case where w_p of 100 μm is kept fixed while w_0 is varied. Fig. 6.11(a) lists the peak values with 10% dithering amplitude relative to the comb spacing. Shaper parameters of w_0 ={95, 70 and 40} μm and an extinction ratios of {20, 40} dB for line [0] are listed. With a better extinction ratio (40dB), peak at f_{rep} is effectively suppressed by ~20dB, providing better waveform fidelity. For better spectral resolution (smaller w_0), dither-induce noise peaks at f_d, $f_{rep}+f_d$ and $2f_{rep}+f_d$ are effectively suppressed, leaving peaks at f_{rep} and $2f_{rep}$ unaltered. These aspects can be understood from the $|H(\omega)|^2$ for the three radii shown in Fig. 6.11(b-d): With a smaller w_0, the resulting $|H(\omega)|^2$ attain a better resemblance of the rectangular mask function M(x) defined by the LCM [10]. The resulting wider, flatter pass-band makes the shaped waveforms less prone to frequency dithering. Interestingly, the shaper transmission edge for a smaller w_0 introduces different noise peak power scaling to dithering amplitude. Fig. 6.11(e) shows noise peak $P(f_{rep}+f_d)$ against dithering amplitude for the three radii values. For w_0= {95 and 70}μm, $P(f_{rep}+f_d)$ adhere to the 20dB/decade relation. As for w_0=40μm, while increasing the dithering amplitude, one notes gradual change in slope from 20dB (<2.5%) to 40dB (2.5 to 5%) and to 60dB (>5%).

In order to provide a more general discussion, we also investigate the effects when w_p and w_0 are proportionally reduced. Fig. 6.12(a) lists the peak values with w_0 ={95, 70 and 40} μm and corresponding w_p = {100, 70 and 40} μm with a 10% dithering amplitude. Effects of extinction ratios are also included for comparison. For better resolution (smaller w_0 and w_p), dither-induce noise peaks at f_d, $f_{rep}+f_d$ and $2f_{rep}+f_d$ are greatly reduced as compared to the previous case. This means the waveform shape is better retained and less susceptible to frequency dithering. In contrast to the previous case, where the shapes of $|H(\omega)|^2$ change as w_0 are reduced, here the shapes of $|H(\omega)|^2$ remain the same, but with decreasing pass-band while w_0 and w_p are reduced proportionally, as shown in Fig. 6.12(b-d). This highlights the essence of this configuration: finer spectral control pixilation eliminates adjacent line in participating waveform generation under frequency dithering, and thus maintaining waveform fidelity. Fig. 6.12(e) shows $P(f_{rep}+f_d)$ against dithering amplitude for the three radii values. For (w_0, w_p)= 70 μm, $P(f_{rep}+f_d)$ still adhere to the 20dB/decade relation for dithering amplitude less ~4.5%, but shows a 40dB/decade relation for greater dithering amplitudes.

As for (w_0, w_p)=40μm, $P(f_{rep}+f_d)$ shows gradual change in slope from 20dB (<2%) to 40dB (2 to 5%) and to 60dB (>5%), similarly observed in the previous case.

These results reveal better extinction ratio and finer spectral resolution (especially finer spectral control pixilation) are favored in line-by-line shaping. Smaller beam radius and finer pixel size make line-by-line waveforms shapes more robust against frequency instability. In practice, shaper resolution can be improved by using grating and focusing lens with larger effective area. Finer spectral control pixilation can be achieved using other spatial light modulator technologies currently commercially available [68,69]. However, extinction ratio is a main limiting factor for waveform fidelity (provided if certain lines are to be suppressed), bounded by the spectral controlling elements. Under very demanding situations, multiple LCMs/shapers can be cascade to yield better extinction ratio at the expensive of higher loss and complexity.

In summary, we have demonstrated the first quantitative investigation of noise introduced by small time-varying optical comb frequency offsets into waveforms generated via line-by-line pulse shaping. Deterministic variations of the offset frequency are obtained by frequency dithering of a continuous-wave laser that is fed into a phase modulator. This results in a controllable effective linewidth broadening. An electrical spectrum analyzer is used to examine the current power spectra of time-domain intensity waveforms subject to frequency dithering of the input. A theoretical model predicting a 20dB/decade scaling relation between the fundamental dither-induced noise peak and the frequency dither amplitude is presented. A numerical simulation method capable of predicting the precise form of the RF power spectrum in the presence of optical frequency dithering is explained. Two specific simple examples of line-by-line shaping, where either a single line or a pair of lines are selected from the comb, are considered in detail. Experimental data are in excellent agreement with the simulated results down to frequency dithers of a few tenths of a percent (a few tens of MHz, since the comb line frequency spacing is 9.15 GHz). Furthermore, our results may be used to predict the contribution of offset frequency variations to pulse shaping noise even for frequency variations below the level that can be clearly measured with our current experimental sensitivity. Effects of shaper parameters over frequency dithering noise are discussed. For finer spectral resolution, dithering-induced noise peaks are effectively suppressed, while having varying power relation to dither amplitude.

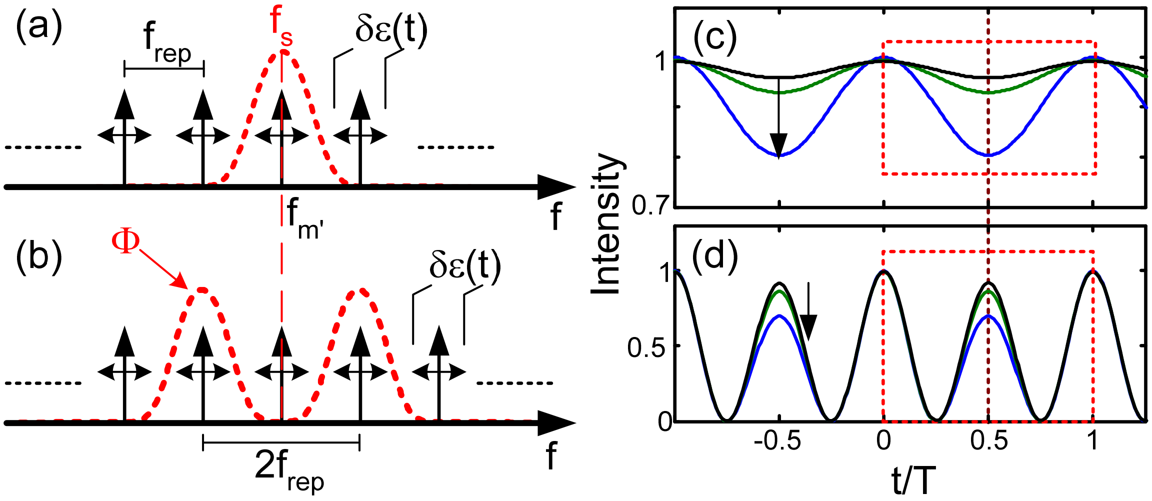

Fig. 6.1. Schematic of comb line filtering from an optical frequency comb with line spacing of f_{rep} and time-varying comb offset variation $\delta\varepsilon(t)$. (a) Single-line filtering case. (b) Two-line filtering with spacing of $2f_{rep}$. Effective shaper filter functions are shown as dotted traces. Filter center frequency f_s is denoted by the dashed line. Corresponding time-domain intensities for (c) single-line and (d) two-line with $\Phi=0$ filtering cases under static comb offsets of {0, 10 and 20}% are shown using method reported in Ref. [10]. In (c, d), the arrows indicate the waveform evolutions with increasing offsets. The dashed squares denote waveforms for one period $T=1/f_{rep}$. Initial pulse locations are at integer multiples of T. The dotted line denotes temporal position of T/2. Maximum time-domain intensity variations happen at temporal position of T/2, as explained using the time-domain point of view in Ref. [9].

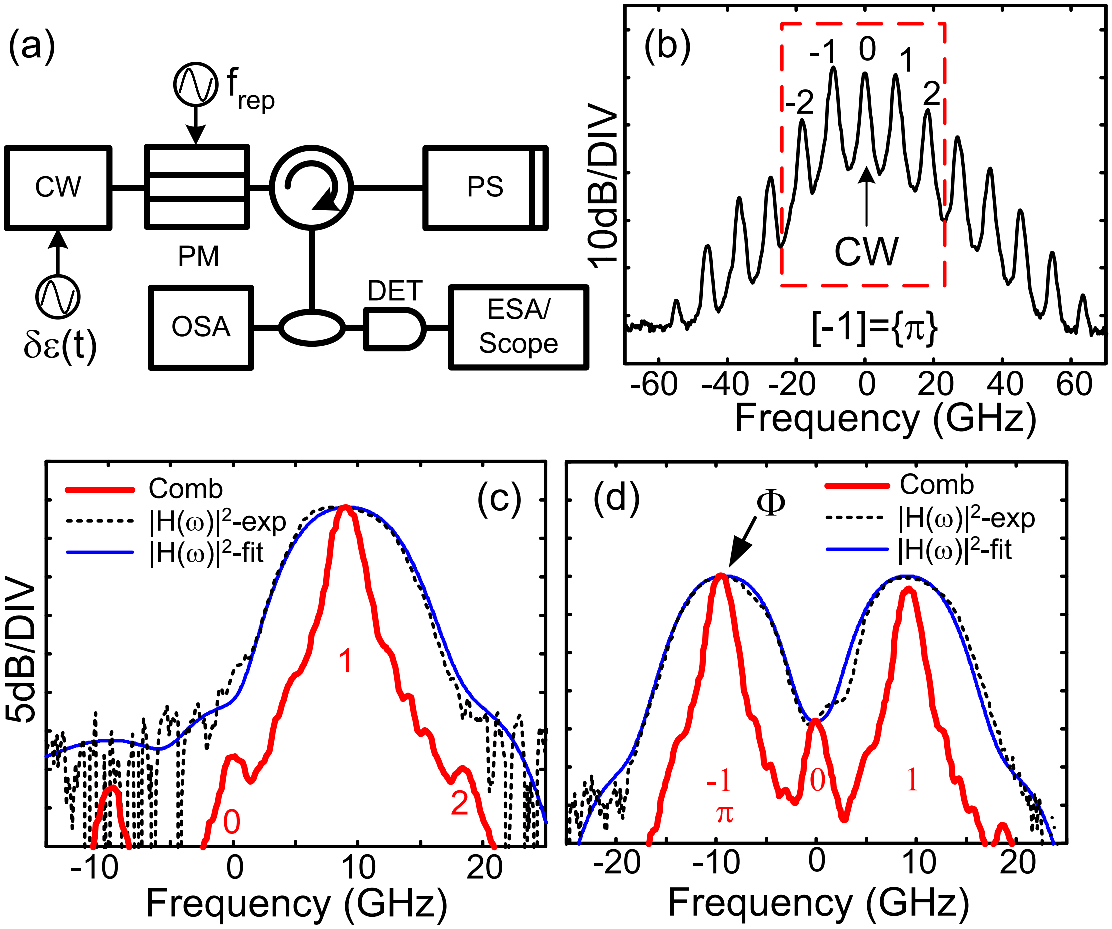

Fig. 6.2. (a) Experimental setup using a PMCW laser frequency comb with repetition frequency of f_{rep}. PM: phase modulator; ε(t): controllable comb line-width broadening; PS: pulse shaper; OSA: optical spectrum analyzer; Scope: 50-GHz bandwidth sampling scope. (b) Optical spectrum of the PMCW comb. Line numbered [0] denotes the CW laser frequency. Line [-1] is intrinsically π out of phase. (c) Single-line filtering after the shaper. (d) Two-line filtering with spacing $2f_{rep}$ after the shaper. Line [-1] is applied with phase control Φ to examine shaping effects. Φ=0 for the figure shown. In (c, d), filtered comb lines are shown using bold traces; experimental (dotted) and simulated (solid) filter functions are plotted for both cases.

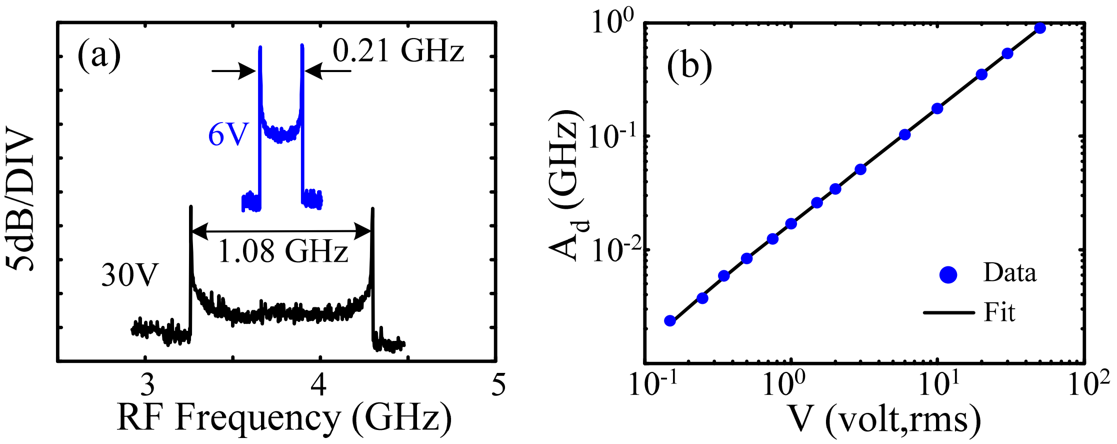

Fig. 6.3. (a) Heterodyne beating results for 6 and 30 volts (rms) applied to the PZT. (b) Relation between frequency dithering amplitudes (A_d) and applied rms voltage (V) to the PZT.

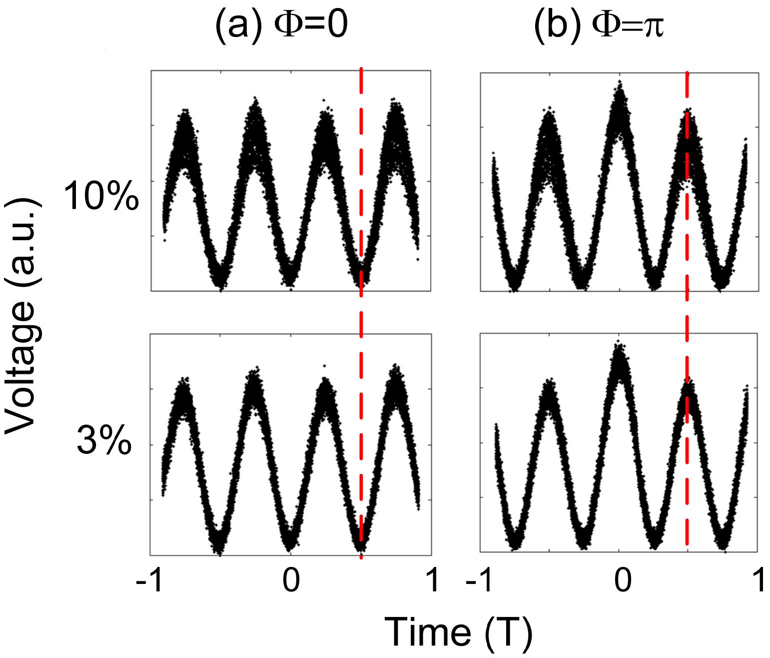

Fig. 6.4. 50 overlaid sampling scope traces with dithering amplitude of 10 and 3% for two-line filtering with phase control Φ={ 0 (a) and π (b)} applied to line [-1] shown in Fig. 3(d). T/2 positions are marked using the dashed lines.

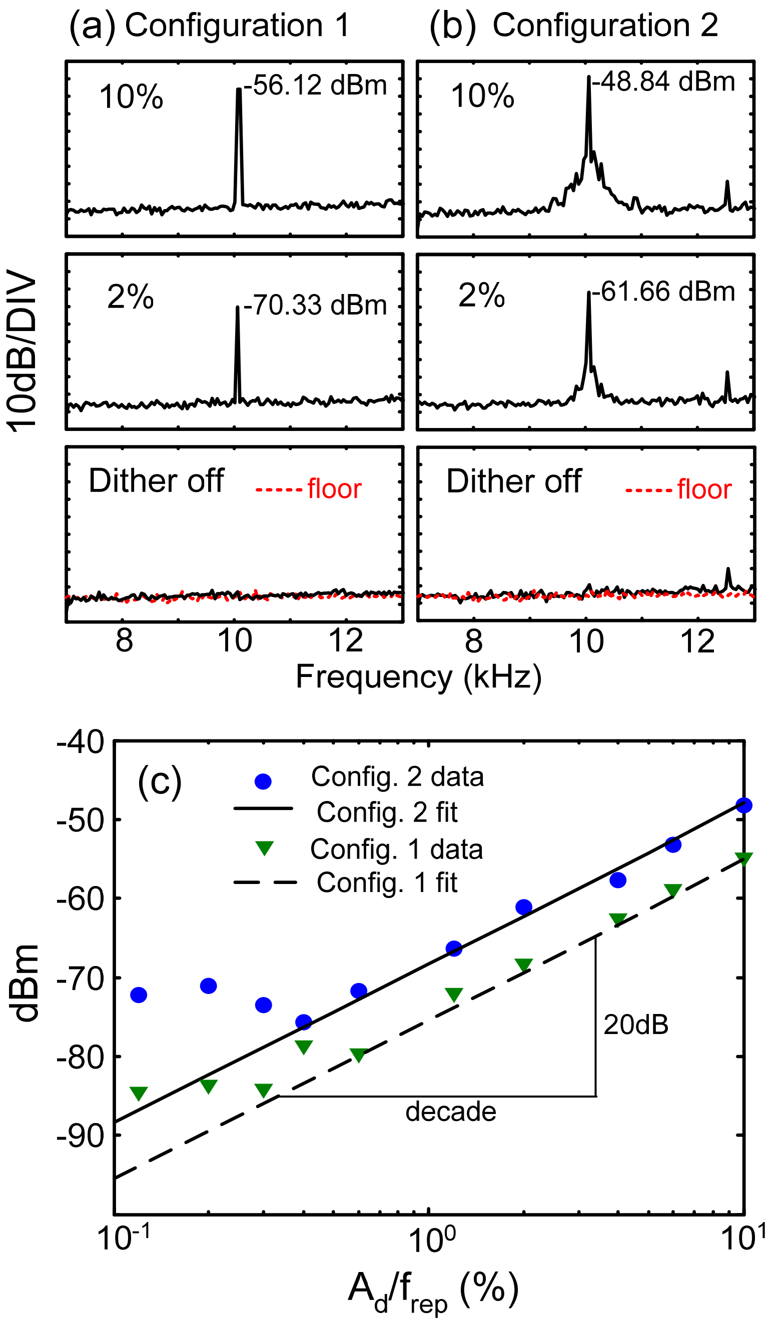

Fig. 6.5. ESA measurements centered at f_d =10 kHz with dithering amplitude A_d/f_{rep} = {10, 2 and 0}%, compared to the 9.15 GHz comb spacing, for configuration 1 (a) and 2 (b). System noise floor (dotted trace) is determined with no optical input power to the photo-detector. In both figures, the traces are obtained by maximum-holding the ESA for 5 minutes with resolution bandwidth of 3 Hz. Noise peaks values are indicated. (c) Noise peak values for configuration 1 (triangle) and 2 (dot) and fitting curves against dither amplitudes are plotted. Data fittings revealing a 20dB/decade relation.

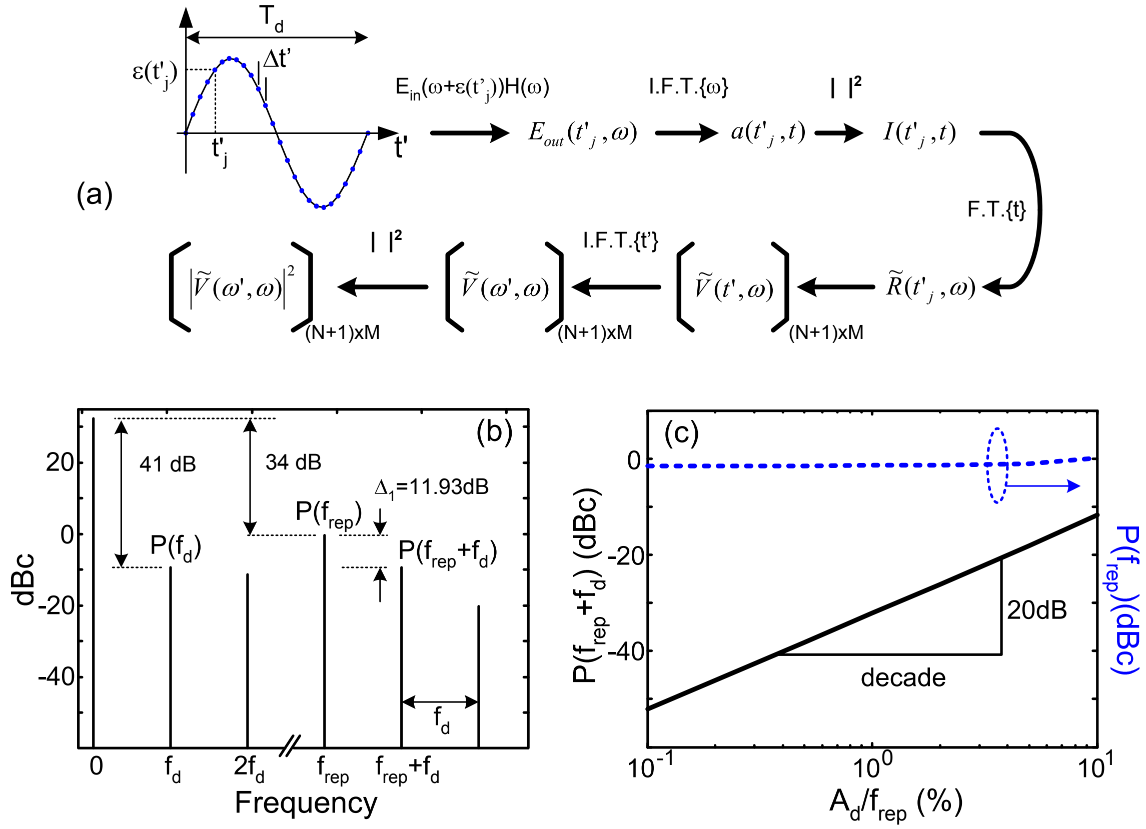

Fig. 6.6. (a) Flow chart of the numerical method. (b) Calculated current power spectrum for the single-line filtering case with 10% dithering amplitude, showing beats from DC to $2f_d$ and f_{rep} to $f_{rep}+2f_d$. Noise peak values at f_d, f_{rep} and $f_{rep}+ f_d$ are labeled $P(f_d)$, $P(f_{rep})$ and $P(f_{rep}+ f_d)$ respectively. Δ_1 denotes the power ratio between $P(f_{rep})$ and $P(f_{rep}+ f_d)$. (c) Simulated relationship of $P(f_{rep}+ f_d)$ and $P(f_{rep})$ to dithering amplitude.

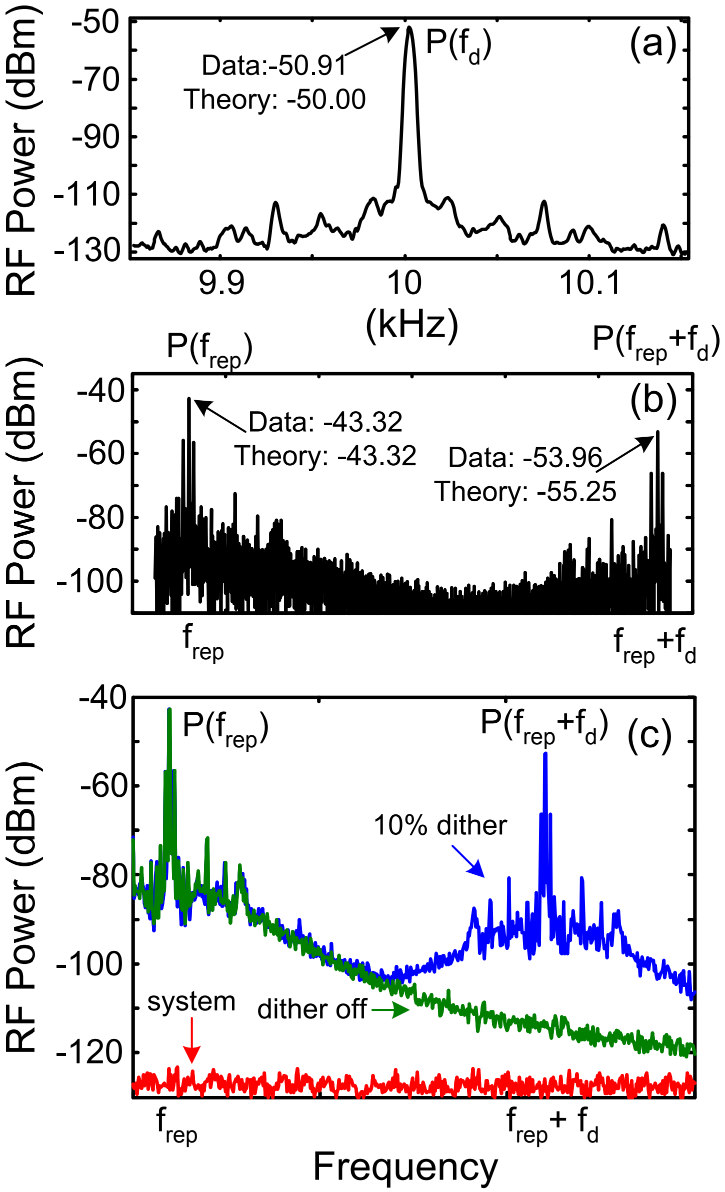

Fig. 6.7. Single-line filtering experimental results with A_d/f_{rep}=10%. (a) ESA measurement of P(f_d) with 300 Hz span. (b) ESA measurement of current power spectrum from frep to $f_{rep}+f_{d.}$ In (a, b), experimental P(f_{rep}) and P(f_{rep}+ f_d) values are compared to calculated results. (c) Maximum hold traces with 10% dithering and no dither, along with system noise floor. In all measurements, ESA resolution bandwidth of 3 Hz is used.

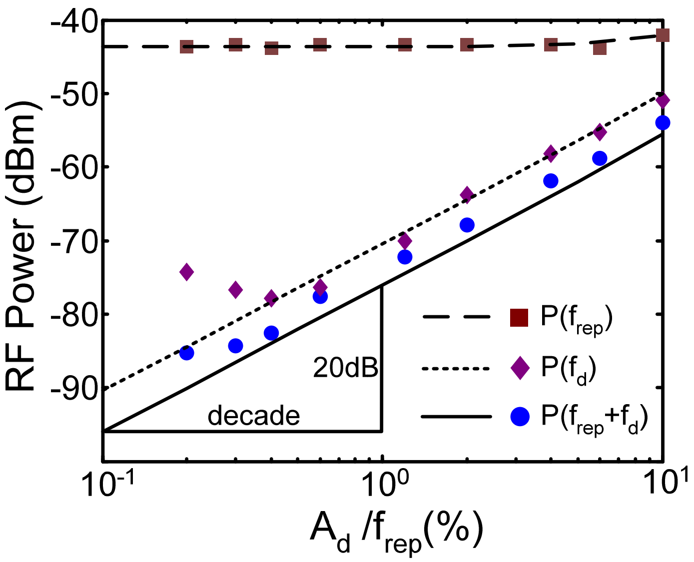

Fig. 6.8. Experimental (symbols) and theoretical (lines) values of $P(f_d)$, $P(f_{rep})$ and $P(f_{rep}+f_d)$ against A_d for single-line filtering.

Table 6.1. Experimental and calculated noise peak values for two-line filtering at $2f_{rep}$ with A_d/f_{rep}=10%. Phase control of Φ={ π, $\pi/2$, and 0} are applied to line [-1] for investigation of phase shaping contributed intensity noise. The calculated peak values are normalized to the experimental $2f_{rep}$ peak and given in dB. Experimental peaks are acquired using ESA resolution bandwidth of 3 Hz. Δ_1, and Δ_2 represent the contrast ratios between the peaks at f_{rep} to $f_{rep}+f_d$ and $2f_{rep}$ to $2f_{rep}+f_d$, respectively.

	Peak frequency	**f_d (dB)**	**f_{rep} (dB)**	**$f_{rep}+f_d$ (dB)**	**Δ_1 (dB)**	**$2f_{rep}$ (dB)**	**$2f_{rep}+f_d$ (dB)**	**Δ_2 (dB)**
$\Phi=\pi$	Data	-59.42	-39.51	-53.31	13.80	-27.52	-62.66	35.14
	Calculation	-59.80	-40.31	-54.45	14.14	-27.52	-63.21	35.69
$\Phi=\pi/2$	Data	-60.50	-40.33	-56.82	16.49	-27.83	-63.15	35.32
	Calculation	-61.09	-40.96	-57.67	16.71	-27.83	-63.95	36.12
$\Phi=0$	Data	-60.13	-48.66	-65.61	16.95	-27.62	-65.00	37.38
	Calculation	-60.74	-49.00	-66.65	17.65	-27.62	-65.31	37.69

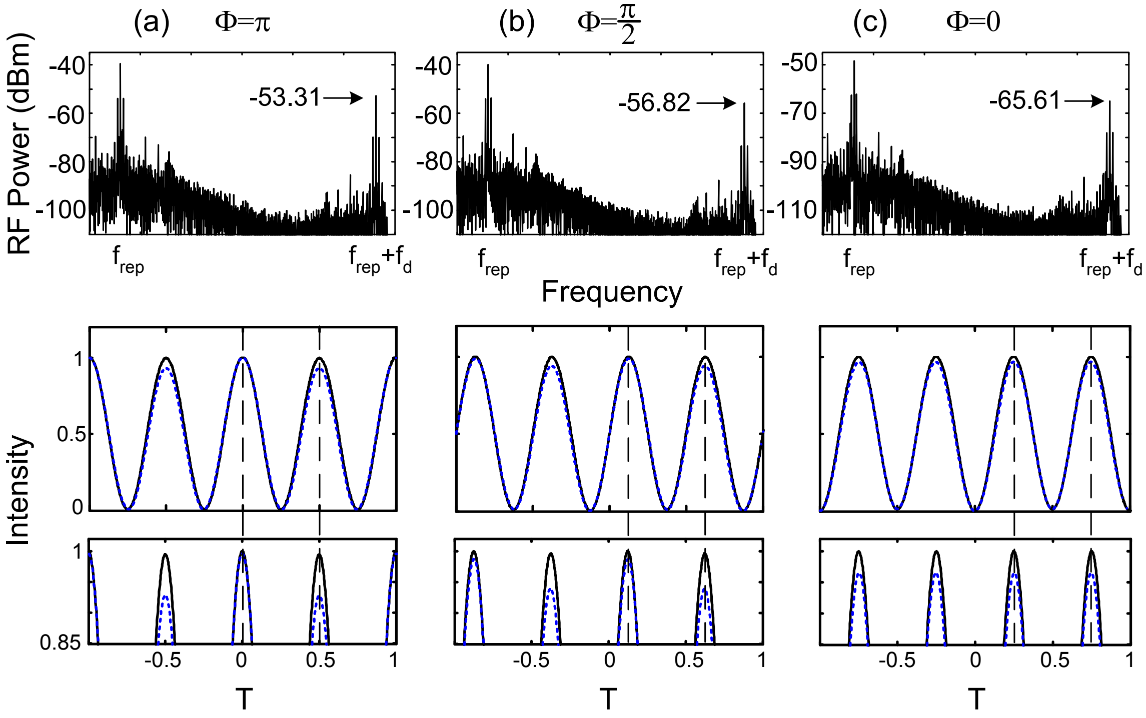

Fig. 6.9. Two-line filtering at $2f_{rep}$ with A_d/f_{rep}=10%: Experimental ESA traces from f_{rep} to $f_{rep}+f_d$ with resolution bandwidth of 3 Hz. Phase control of Φ={ π (a), π/2 (b), and 0 (c)} are applied to line [-1] for investigation of shaper contributed intensity noise. Corresponding intensities with {0 (solid), 10 (dotted)}% static frequency shift and the expanded view on the intensity peaks are shown. As an aid to the eye, dashed lines denote the temporal positions of peaks in the intensity waveforms.

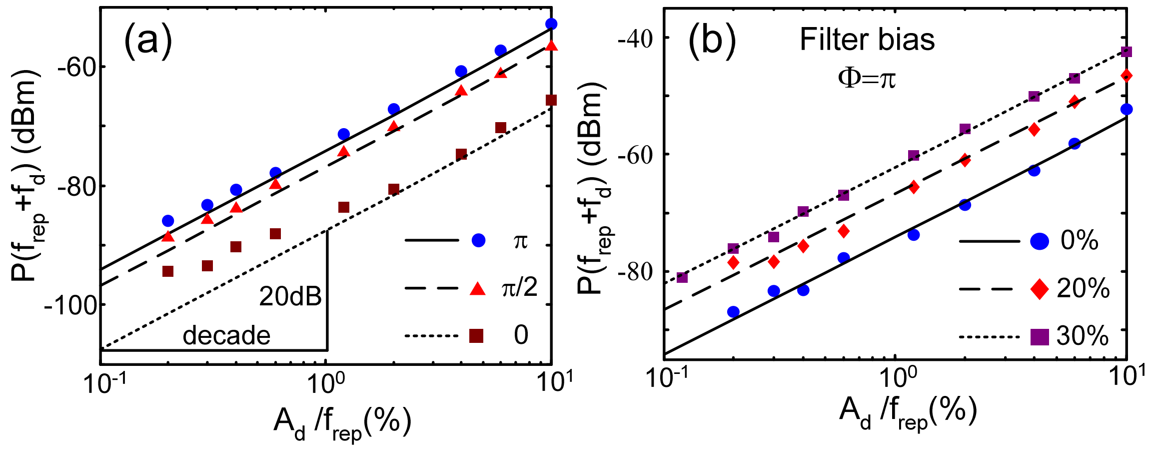

Fig. 6.10. Experimental results of $P(f_{rep}+f_d)$ against A_d for two-line filtering at $2f_{rep}$. (a) Data are shown with symbols for phase control values $\Phi=\{\pi, \pi/2, \text{and } 0\}$ along with theoretical values shown using lines. (b) Filter frequency bias results with $\Phi=\pi$. Experimental data are shown with symbols for bias positions of {0%, 20%, and 30%} along with theoretical results shown using lines.

(a)

w_0 (μm)	ER (dB)	$P(f_d)$	$P(f_{rep})$	$P(f_{rep}+f_d)$	$P(2f_{rep})$	$P(2f_{rep}+f_d)$
95	20	-59.80	-40.31	-54.45	-27.52	-63.21
	40	-71.94	-59.41	-54.35	-27.48	-86.39
70	20	-74.53	-40.26	-67.87	-27.44	-76.40
	40	-92.48	-60.14	-67.82	-27.38	-96.81
40	20	-128.24	-40.21	-121.04	-27.32	-129.54
	40	-148.23	-60.21	-120.99	-27.31	-149.54

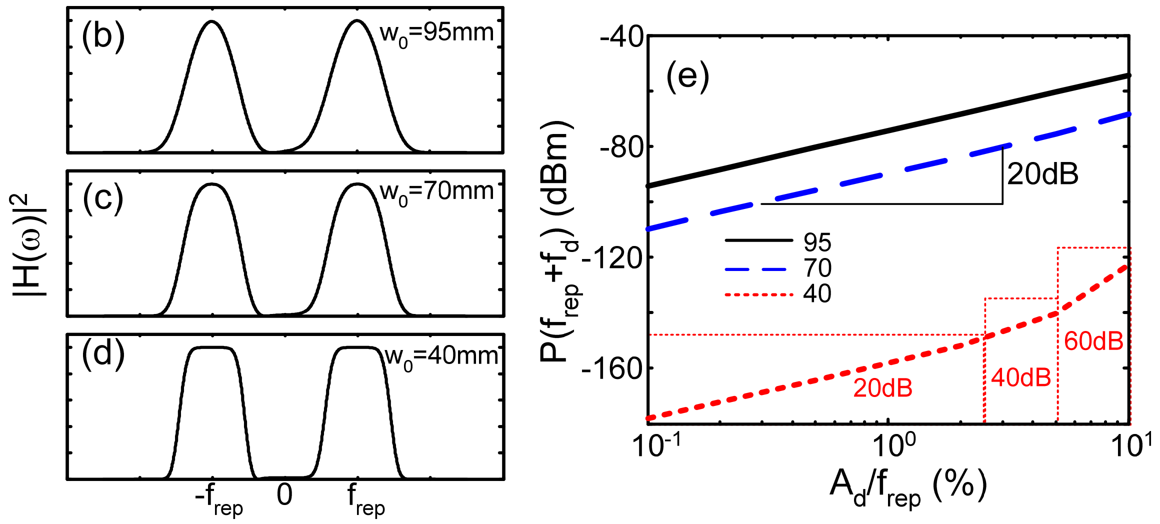

Fig. 6.11. Effects of shaper parameters on frequency dithering through simulation: using 2-line filtering at $2f_{rep}$ with $\Phi=\pi$ case as example. LCM pixel size of 100μm is fixed. (a) List of noise peaks with 10% dithering amplitude for minimum spot radius w_o = {95, 70 and 40} μm and extinction ratio (ER) of {20, 40} dB to line [0]. (b-d) $|H(\omega)^2|$ for the three radii with ER=20 dB. (e) $P(f_{rep}+f_d)$ against dithering amplitude for w_o = {95(solid), 70(dashed) and 40(dotted)} μm.

(a)

w_0 (μm)	w_p (μm)	ER (dB)	$P(f_d)$	$P(f_{rep})$	$P(f_{rep}+f_d)$	$P(2f_{rep})$	$P(2f_{rep}+f_d)$
95	100	20	-59.80	-40.31	-54.45	-27.52	-63.21
		40	-71.94	-59.41	-54.35	-27.48	-86.39
70	70	20	-74.18	-40.54	-90.58	-27.52	-94.12
		40	-75.86	-60.53	-90.43	-27.64	-100.43
40	40	20	-278.61	-41.25	-271.31	-27.52	-279.81
		40	-306.91	-61.26	-271.26	-28.36	-300.15

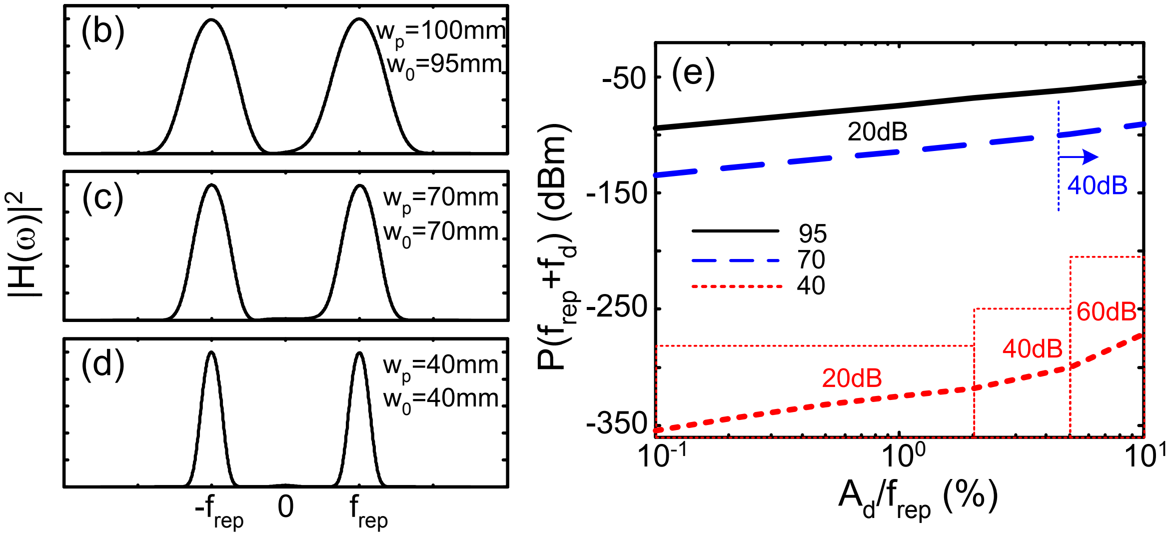

Fig. 6.12. Effects of shaper parameters on frequency dither noise: using 2-line filtering at $2f_{rep}$ with $\Phi=\pi$ case as example. LCM pixel size w_p is reduce proportional to w_0. (a) List of noise peaks with 10% dithering amplitude for w_0 = {95, 70 and 40} μm and extinction ratio (ER) of {20, 40} dB to line [0]. (b-d) $|H(\omega)^2|$ for the three sets with ER=20 dB. (e) $P(f_{rep}+f_d)$ against dithering amplitude for w_o = {95(solid), 70(dashed) and 40(dotted)} μm.

7. CONCLUSIONS AND FUTURE PERSPECTIVES

In conclusion, optical combs with relatively high frequency stability have been generated by phase-modulating a CW laser. Various results have been accomplished, namely:

(1) In the comb controlling perspectives, line-by-line pulse shaping have been used to demonstrate the generation of transform-limited high repetition rate optical pulse trains, optical arbitrary waveform generations and rapid reprogrammable microwave arbitrary waveforms, both using phase-modulated CW laser frequency combs.

(2) In the comb characterization perspectives, two different frequency combs, generated via phase modulation of a continuous-wave laser and spectrally broadened in either dispersion-decreasing fiber or normal dispersion highly nonlinear fiber have been characterized via a variety of methods. Our work shows that DPSK decoding, which accounts for intensity noise, timing jitter, and linewidth degradations within one single process, may be a valuable addition to the suite of tools available for characterization of optical comb sources.

(3) In characterizing the impact of comb frequency instability on the line-by-line shaped waveforms, both static and time-varying frequency instabilities have been systematically studies using the advantage of tuning ability offered by the PMCW combs.

Based on the demonstrations and current conclusions drawn from this dissertation, various future improvements and/or directions can be directly anticipated:

(1) Generation of broader optical frequency combs

As stated in Chapter 1, true optical arbitrary waveform generation (O-AWG) not only requires independent amplitude/phase control to individual comb lines, but also demands the number of lines available for waveform generation. As seen in Chapter 2, we generated ~ 100 lines (within -12 dB level) and ~ 300 lines (within – 40 dB) from a PMCW comb after soliton compression at repetition frequency of 9 GHz. However, the comb spectral profile is not smooth due to non-ideal soliton compression. Here we would seek to further extend the comb bandwidth (available lines) generated to beyond 10 THz (over 1000 comb lines) at repetition frequency of 10 GHz, while also obtaining a smooth comb spectral profile.

Throughout the years, many additional comb broadening methods from high repetition-rate seeding optical pulses using nonlinear optical effects have been demonstrated [22,23, 51-54]. Optical fibers with specially designed dispersion profiles of both 2nd and 3rd order (even ups to 4th order in [70]) are used and are the essential determining elements. Figure 7.1 shows the schematic of the proposed experimental configuration. In Fig. 7.1(a), picosecond optical pulses at 10 GHz repetition-rate from either mode-locked fiber laser (MLL) or PMCW comb is first amplified and sent to our DDF soliton compressor. The output comb profile will have the resemblance shown in Fig. 7.1(b). In order to obtain a broad and smooth comb, Fig. 7.1(a) uses a pulse shaper (PS) for smoothening the comb profile and possible spectral phase compensation. The corrected pulse is then send to a second optical amplifier and excites a HNLF of length L and dispersion value D at an average power of P_{HNLF}. Fig 7.1(b) shows another configuration, in which the spectral correction is achieved by a NOLM proposed in the previous section.

Figure 7.2 shows the simulated results by solving Eqn. (2.1) using split-step Fourier method. For a broad and smooth optical frequency comb generation, large P_{HNLF} is required. Anomalous dispersion is therefore not desired since higher-order soliton formation induces soliton fission [71], generating large spectral dips as illustrated in Fig. 7.2(a). In Fig. 7.2(a), 50 m of HNLF with D= 2 ps/nm/km and P_{HNLF} = 25 dBm is used. To properly generate the desired comb, SPM and normal dispersion is preferred. Figure 7.2(b) shows simulation results assuming the input spectrum (solid) is ideally corrected using configuration proposed in Fig. 7.1(a), using 50 m of HNLF with D= -2 ps/nm/km and P_{HNLF} = 25 dBm. The output spectrum (dash) reveals a smoothly broadened comb with a -3 dB bandwidth of greater than 5.7 THz, and a -10 dB bandwidth of greater than 10 THz. Figure 7.2(c) shows simulation results assuming the input spectrum (solid) is corrected using a NOLM proposed in Fig. 7.1(b). The NOLM parameters are consistent with the discussions made in Chapter 2. Within the simulation, 50 m of HNLF with D= -2 ps/nm/km and P_{HNLF} = 25 dBm is used. The output spectrum (dash) reveals a smoothly broadened comb with a -3 dB bandwidth of greater than 4.75 THz, and a -10 dB bandwidth of greater than 12.5 THz. Figure 7.2(d) shows the magnified squared central spectral portion in Fig. 7.2(c). With P_{HNLF} exceeding 30 dBm, the smooth optical frequency comb may be further extended to having a -3 dB bandwidth of greater than 7.3 THz, and a -10 dB bandwidth of greater than 22 THz with the same HNLF condition.

(2) Improvements of reprogrammable microwave waveforms

As discussed in the end of Chapter 3, the rapid reprogrammable waveform update scheme proposed therein has great potential for significant scalability and extensibility. For example: (a) Waveforms of different repetition rates and bandwidths may be obtained through a slight modification of the comb generator setup, where each CW wavelength has its own temporal gating function followed by unique phase-modulation period. (b) The waveform update rate can be increased by using a faster data pattern generator. (c) The bulk wavelength switching in our current scheme can be replaced by a monolithically integrated wavelength converter [38]. Multi-level analog driving signals can be used to drive the wavelength convertor, realizing rapid switching among multiple microwave waveforms. (d) Another approach is to current modulate (and thus frequency modulate) a distributed feedback laser diode [72]. Here multi-level current drives will induce different frequency shifts of the laser diode. A schematic sketch of using our current BERT (only two-leveled output voltage) to generate multi-level driving signal is given in Fig. 7.3. The idea is to use RF power splitter/combiner with appropriate RF delay adjustments to synthesize desired multiple leveled driving signal. Fig. 7.3(a, b) show that three- and four-leveled driving signals can be derived from the two-leveled BERT output. (e) Incorporating points (c, d) while extending the current one-dimensional shaper into two-dimensional geometry [39], switching among more than a hundred distinct waveforms can be anticipated.

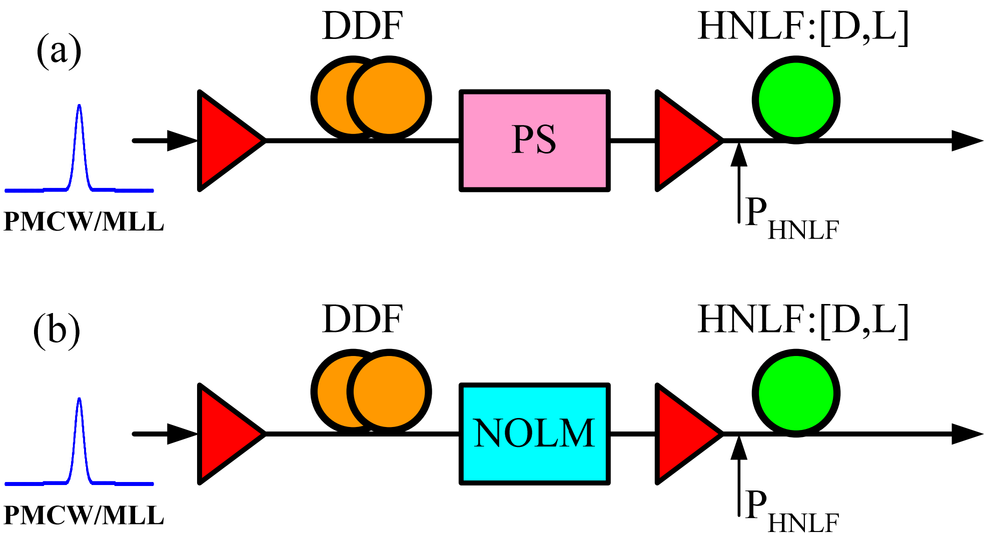

Fig. 7.1. Schematics of > 10 THz comb generation experimental setup. (a) Using pulse shaper to smoothen the DDF compressed spectrum. (b) Using NOLM to smoothen the DDF compressed spectrum.

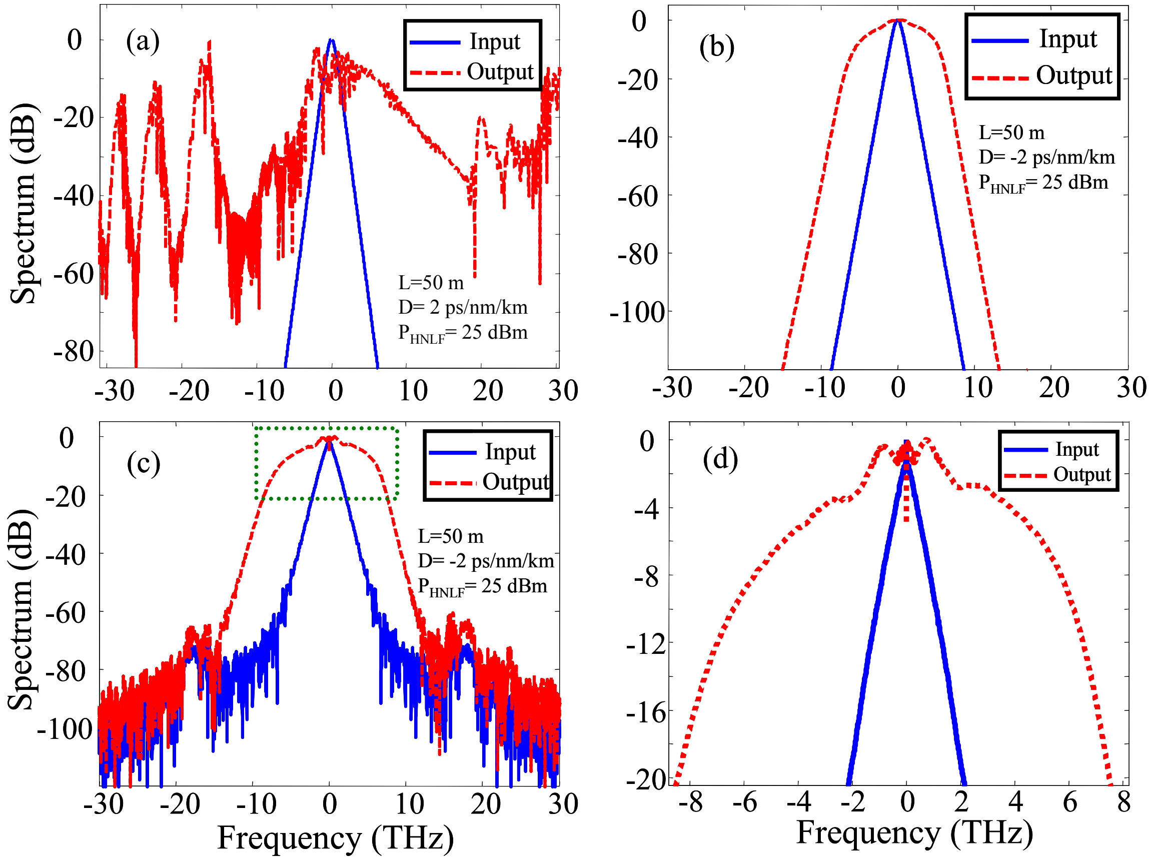

Fig. 7.2. Simulation results for broad and smooth comb generation. (a) Using HNLF with anomalous dispersion. (b) HNLF with normal dispersion, spectrum corrected using a pulse shaper. (c) HNLF with normal dispersion, spectrum corrected using a NOLM. (d) Magnified view of the central portion in (c).

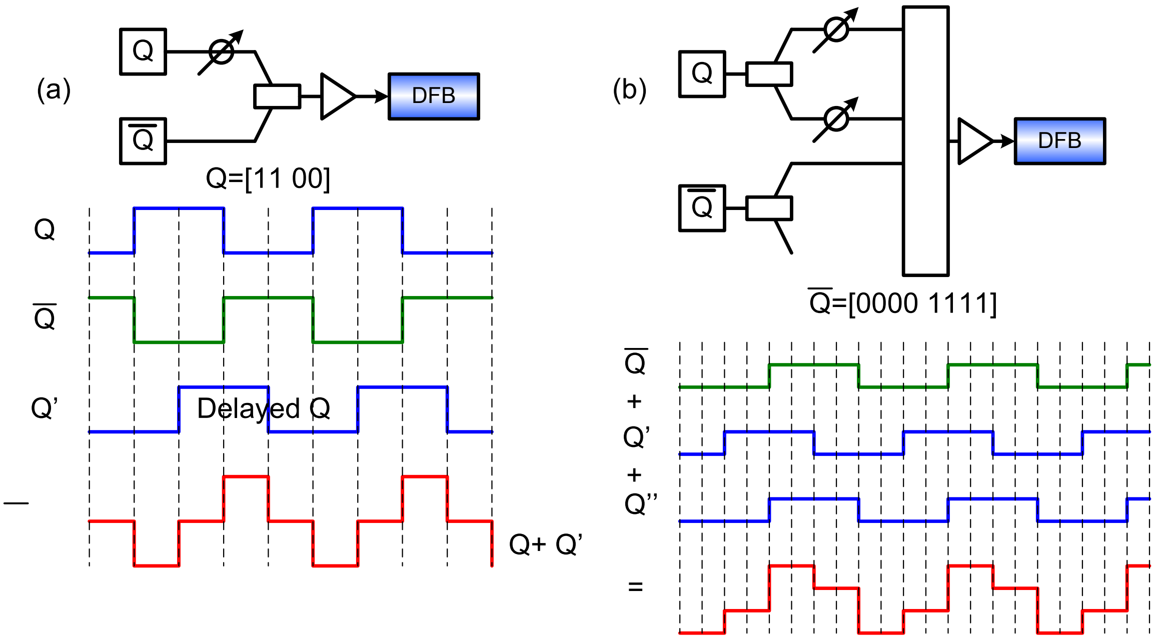

Fig. 7.3. Rapid multiple RF waveform update using a distributed feedback (DFB) laser. (a) Three level driving signal can be derived from two-leveled BERT output using splitting, delay adjustments and recombine. (b) Four level driving signal also possible.

LIST OF REFERENCES

LIST OF REFERENCES

[1] D. J. Jones, S. A. Diddams, J. K. Ranka, A. Stentz, R. S. Windeler, J. L. Hall, S. T. Cundiff, “Carrier-envelope phase control of femtosecond mode-locked lasers and direct optical frequency synthesis,” *Science*, vol. 288, pp. 635-639, April 2000.

[2] T. Udem, R. Holzwarth, T. W. Hansch, “Optical frequency metrology,” *Nature*, vol. 416, pp. 233-237, March 2002.

[3] L. S. Ma, Z. Y. Bi, A. Bartels, L. Robertsson, M. Zucco, R. S. Windeler, G. Wilpers, C. Oates, L. Hollberg, and S. A. Diddams, "Optical frequency synthesis and comparison with uncertainty at the 10^{-19} level," *Science*, vol. 303, pp. 1843-1845, March 2004.

[4] L. Xu, Ch. Spielmann, A. Poppe, T. Brabec, F. Krausz, T. W. H¨ansch, “Route to phase control of ultrashort light pulses,” *Opt. Lett.*, vol. 21, no. 24, pp. 2008-2010, Dec. 1996.

[5] T. Kobayashi, H. Yao, K. Amano, Y. Fukushima, A. Morimoto, and T. Sueta, “Optical pulse compression using high-frequency electrooptic phase modulation,” *IEEE J. Quantum Electron.*, vol. 24, no. 2, pp. 382-387, Feb. 1988.

[6] C.-B. Huang, Z. Jiang, D. E. Leaird, A. M. Weiner, “High-rate femtosecond pulse generation via line-by-line processing of a phase-modulated CW laser frequency comb,” *Electron. Lett.*, vol. 42, no. 19, pp. 1114-1115, Sep. 2006.

[7] A. M. Weiner, “Femtosecond pulse shaping using spatial light modulators,” *Rev. Sci. Instr.*, vol. 71, no. 5, pp. 1929-1960, May 2000.

[8] Z. Jiang, D. E. Leaird, A. M. Weiner, “Line-by-line pulse shaping control for optical arbitrary waveform generation,” *Opt. Express*, vol. 13, no. 25, pp. 10431-10439, Dec. 2005.

[9] Z. Jiang, D. S. Seo, D. E. Leaird, A. M. Weiner, “Spectral line-by-line pulse shaping,” *Opt. Lett.*, vol. 30, no. 12, pp. 1557-1559, June 2005.

[10] C.-B. Huang, Z. Jiang, D. E. Leaird, A. M. Weiner, “The impact of optical comb stability on waveforms generated via spectral line-by-line pulse shaping,” *Opt. Express*, vol. 14, no. 26, pp. 13164-13176, Dec. 2006.

[11] T. F. Carruthers, I. N. Duling III, "10-GHz, 1.3-ps erbium fiber laser employing soliton pulse shortening," *Opt. Lett.*, vol. 21, no. 23, pp. 1927-1929, Dec. 1996.

[12] S. Hisatake, Y. Nakase, K. Shibuya, and T. Kobayashi, "Generation of flat power-envelope terahertz-wide modulation sidebands from a continuous-wave laser based on an external electro-optic phase modulator," *Opt. Lett.*, vol. 30, pp. 777-779, April 2005.

[13] H. Murata, A. Morimoto, T. Kobayashi, and S. Yamamoto, "Optical pulse generation by electrooptic-modulation method and its application to integrated ultrashort pulse generators," *IEEE J. Select. Topics Quantum Electron.*, vol. 6, no. 6, pp. 1325-1331, Nov./Dec. 2000.

[14] J. van Howe, J. Hansryd, and C. Xu, "Multiwavelength pulse generator using time-lens compression", *Opt. Lett.*, vol. 29, no. 13, pp. 1470-1472, July, 2004.

[15] Z. Jiang, D. E. Leaird, A. M. Weiner, "Optical processing based on spectral line-by-line pulse shaping on a phase modulated CW laser," *IEEE J. Quantum Electron.,* vol. 42, no. 7, pp. 657-665, July 2006.

[16] D. Miyamoto, K. Mandai, T. Kurokawa, S. Takeda, T. Shioda, and H. Tsuda, "Waveform-controllable optical pulse generation using an optical pulse synthesizer," *IEEE Photon. Technol. Lett.*, vol. 18, no. 5, pp. 721-723, March 2006.

[17] Z. Jiang, D. E. Leaird, and A. M. Weiner, "Optical arbitrary waveform generation and characterization using spectral line-by-line control," *J. Lightwave Technol.*, vol. 24, no. 7, pp. 2487-2494, July 2006.

[18] N. J. Doran, D. Wood, "Nonlinear-optical loop mirror," *Opt. Lett.*, vol. 13, no. 1, pp. 56-58, Jan. 1988.

[19] K. Smith, N.J. Doran, P.G. Wigley, "Pulse shaping, compression, and pedestal suppression employing a nonlinear-optical loop mirror," *Opt. Lett.*, vol. 15, no. 22, pp. 1294-1296, Nov. 1990.

[20] N. J. Smith, N. J Doran, "Picosecond soliton transmission using concatenated nonlinear optical loop-mirror intensity filters," *J. Opt. Soc. Am. B*, vol. 12, no. 6, pp. 1117-1125, June 1995.

[21] M. D. Pelusi, Y. Matsui, A. Suzuki, "Pedestal suppression from compressed femtosecond pulses using a nonlinear fiber loop mirror," *IEEE J. Quantum Electron.*, vol. 35, no. 6, pp. 867-874, June 1999.

[22] K. R. Tamura, M. Nakazawa, "Spectral-smoothing and pedestal reduction of wavelength tunable quasi-adiabatically compressed femtosecond solitons using a dispersion-flattened dispersion-imbalanced loop mirror," *IEEE Photon. Technol. Lett.*, vol. 11, no. 2, pp. 230-232, Feb. 1999.

[23] K. R. Tamura, M. Nakazawa, "A polarization-maintaining pedestal-free femtosecond pulse compressor incorporating an ultrafast dispersion-imbalanced nonlinear optical loop mirror," *IEEE Photon. Technol. Lett.*, vol. 13, no. 5, pp. 526-528, May 2001.

[24] P. V. Mamyshev, S. V. Chernikov, E. M. Dianov, "Generation of fundamental soliton trains for high bit rate optical fiber communication lines," *IEEE J. Quantum Electron.*, vol. 27, no. 10, pp. 2347-2355, Oct. 1991.

[25] Z. Jiang, C.-B. Huang, D. E. Leaird, and A. M. Weiner, "Optical arbitrary waveform processing of more than 100 spectral comb lines," *Nature Photon.*, vol. 1, no. 8, pp. 463-467, Aug. 2007.

[26] C.-B. Huang, D. E. Leaird, A. M. Weiner, "Time-multiplexed photonically enabled radio-frequency arbitrary waveform generation with 100 ps transitions," *Opt. Lett.*, vol. 32, no. 22, pp. 3242-3244, Nov. 2007. (Selected by Virtual Journal of Ultrafast Science, vol. 7, no. 1, 2008.)

[27] E. Frumker, Y. Silberberg, "Femtosecond pulse shaping using a two-dimensional liquid-crystal spatial light modulator," *Opt. Lett.*, vol. 32, no. 11, pp. 1384-1386, June 2007.

[28] C. W. Hillegas, J. X. Tull, D. Goswami, D. Strickland, and W. S. Warren, "Femtosecond laser pulse shaping by use of microsecond radio-frequency pulses," *Opt. Lett.*, vol. 19, no. 10, pp. 737-739, May 1994.

[29] E. Frumker, E. Tal, Y. Silberberg, and D. Majer, "Femtosecond pulse-shape modulation at nanosecond rates," *Opt. Lett.*, vol. 30, no. 20, pp. 2796-2798, Oct. 2005.

[30] N. K. Fontaine, R. P. Scott, J. Cao, A. Karalar, W. Jiang, K. Okamoto, J. P. Heritage, B. H. Kolner, and S. J. B. Yoo, "32 phase X 32 amplitude optical arbitrary waveform generation," *Opt. Lett.*, vol. 32, no. 7, pp. 865-867, April 2007.

[31] T. Yilmaz, C. M. DePriest, T. Turpin, J. H. Abeles, and P. J. Delfyett, "Towards a photonic arbitrary waveform generator using a modelocked external cavity semiconductor laser," *IEEE Photon. Technol. Lett.,* vol. 14, no. 11, pp. 1608-1610, Nov. 2002.

[32] S. Ozharar, F. Quinlan, S. Gee, and P. J. Delfyett, "Demonstration of endless phase modulation for arbitrary waveform generation," *IEEE Photon. Technol. Lett.*, vol. 17, no. 12, pp. 2739-2741, Dec. 2005.

[33] S. Ozharar, S. Gee, F. J. Quinlan, and P. J. Delfyett, "Time-division-multiplexing-based modulation scheme for RF chirp extension," *Electron. Lett.*, vol. 42, no. 12, pp. 714-715, June 2006.

[34] D. E. Leaird, Z. Jiang, and A. M. Weiner, "Experimental investigation of security issues in OCDMA: a code-switching scheme," *Electron. Lett.*, vol. 41, no. 14, pp. 817-819, July 2005.

[35] P. J. Delfyett, S. Gee, C. Myoung-Taek, H. Izadpanah, L. Wangkuen, S. Ozharar, F. Quinlan, and T. Yilmaz, "Optical frequency combs from semiconductor lasers and applications in ultrawideband signal processing and communications," *J. Lightwave Technol.*, vol. 24, no. 7, pp. 2701-2719, July 2006.

[36] J. D. McKinney, D. E. Leaird, and A. M. Weiner, "Millimeter-wave arbitrary waveform generation with a direct space-to-time pulse shaper," *Opt. Lett.*, vol. 27, no. 15, pp. 1345-1347, Aug. 2002.

[37] I. S. Lin, J. D. McKinney, and A. M. Weiner, "Photonic synthesis of broadband microwave arbitrary waveforms applicable to ultra-wideband communication," *IEEE Microw. Wireless Compon. Lett.*, vol. 15, no. 4, pp. 226-228, April 2005.

[38] V. Lal, M. L. Masanovic, J. A. Summers, L. A. Coldren, and D. J. Blumenthal, "Performance optimization of an InP-based widely tunable wavelength converter operating at 40Gb/s," *IEEE Photon. Technol. Lett.*, vol. 18, no. 4, pp. 577-579, Feb. 2006.

[39] S. X. Wang, S. Xiao, and A. M. Weiner, "Broadband, high spectral resolution 2-D wavelength-parallel polarimeter for dense WDM systems," *Opt. Express*, vol. 13, no. 23, pp. 9374-9380, Nov. 2005.

[40] C.-B. Huang, S.-G. Park, D. E. Leaird, A. M. Weiner, "Nonlinearly broadened phase-modulated continuous-wave laser frequency combs characterized using DPSK decoding," *Opt. Express*, vol. 16, no. 4, pp. 2520-2527, Feb. 2007.

[41] R. A. Linke and A. H. Gnauck, "High-capacity coherent lightwave systems," *J. Lightwave Technol.*, vol. 6, no. 11, pp. 1750–1769, Nov. 1988.

[42] H. Toba, K. Oda, and K. Nosu, "Design and performance of FSK-direct detection scheme for optical FDM systems," *J. Lightwave Technol.*, vol. 9, no. 10, pp. 1335–1343, Oct. 1991.

[43] T. Chikama, S. Watanabe, T. Naito, H. Onaka, T. Kiyonaga, Y. Onoda, H. Miyata, M. Suyama, M. Seino, and H. Kuwahara, "Modulation and demodulation techniques in optical heterodyne PSK transmission systems," *J. Lightwave Technol.*, vol. **8**, no. 3, pp. 309–325, Mar. 1990.

[44] A. H. Gnauck and P. J. Winzer, "Optical phase-shift-keyed transmission," *J. Lightwave Technol.*, vol. 23, no. 1, pp. 115–130, Jan. 2005.

[45] M. Mlejnek, "Balanced differential phase-shift keying detector performance: an analytical study," *Opt. Lett.*, vol. 31, no. 15, pp. 2266-2268, Aug. 2006.

[46] S. Weisser, S. Ferber, L. Raddatz, R. Ludwig, A. Benz, C. Boerner, and H. G. Weber, "Single- and alternating polarization 170 Gb/s transmission up to 4000 km using dispersion-managed fiber and all-Raman amplification," *IEEE Photon. Technol. Lett.*, vol. 18, no. 12, pp. 1320–1322, June 2006.

[47] H. G. Weber, S. Ferber, M. Kroh, C. Schmidt-Langhorst, R. Ludwig, V. Marembert, C. Boerner, F. Futami, S. Watanabe, and C. Schubert, "Single channel 1.28 T/s and 2.56 Tb/s DQPSK transmission," *Electron. Lett.*, vol. 42, no. 3, pp. 178–179, Feb. 2006.

[48] H. G. Weber, R. Ludwig, S. Ferber, C. Schmidt-Langhorst, M. Kroh, V. Marembert, C. Boerner, and C. Schubert, "Ultrahigh-speed OTDM-transmission technology," *J. Lightwave Technol.*, vol. 24, no. 12, pp. 4616–4627, Dec. 2006.

[49] F. Quinlan, S. Gee, S. Ozharar, and P. J. Delfyett, "Ultralow-jitter and –amplitude-noise semiconductor-based actively mode-locked laser," *Opt. Lett.*, vol. 31, no. 19, pp. 2870-2872, Oct. 2006.

[50] S. Gee, S. Ozharar, F. Quinlan, J. J. Plant, P. W. Juodawlkis, and P. J. Delfyett, "Self-stabilization of an actively mode-locked semiconductor-based fiber-ring laser for ultralow jitter," *IEEE Photon. Technol. Lett.*, vol. 19, no. 7, pp. 498-500, April 2007.

[51] K. Tamura, H. Kubota, M. Nakazawa, "Fundamentals of stable continuum generation at high repetition rates," *IEEE J. Quantum Electron.*, vol. 36, no. 7, pp. 773-779, July 2000.

[52] F. Futami and K. Kikuchi, "Low-noise multiwavelength transmitter using spectrum-sliced supercontinuum generated from a normal group-velocity dispersion fiber," *IEEE Photon. Technol. Lett.*, vol. 13, no. 1, pp. 73-75, Jan. 2001.

[53] H. Sotobayashi and K. Kitayama, "Observation of phase conservation in multiwavelength binary phase shift–keying pulse-sequence generation at 10 Gbits_s by use of a spectrum-sliced supercontinuum in an optical fiber," *Opt. Lett.*, vol. 24, no. 24, pp. 1820-1822, Dec. 1999.

[54] T. Kuri, T. Nakasyotani, H. Toda and K. Kitayama, "Characterization of supercontinuum light source for WDM millimeter-wave-band radio-over-fiber systems," *IEEE Photon. Technol. Lett.*, vol. 17, no. 6, pp. 1274-1276, June 2005.

[55] K. L. Corwin, N. R. Newbury, J. M. Dudley, S. Coen, S. A. Diddams, K. Weber, and R. S. Windeler, "Fundamental noise limitations to supercontinuum generation in microstructure fiber," *Phys. Rev. Lett.*, vol. 90, no. 11, 113904, Mar. 2003.

[56] N. R. Newbury, B. R. Washburn, K. L. Corwin, and R. S. Windeler, "Noise amplification during supercontinuum generation in microstructure fiber," *Opt. Lett.*, vol. 28, no. 11, pp. 944-946, June 2003.

[57] D. M. Baney and W. V. Sorin, "High resolution optical frequency analysis," in Fiber Optic Test and Measurement, D. Derickson, ed. (Prentice Hall, 1998), pp.169-219.

[58] T. Sakamoto, T. Kawanishi, and M. Izutsu, "Asymptotic formalism for ultraflat optical frequency comb generation using a Mach-Zehnder modulator," *Opt. Lett.*, vol. 32, no. 11, pp. 1515-1517, June 2007.

[59] J. van Howe, J. H. Lee, and C. Xu, "Generation of 3.5 nJ femtosecond pulses from a continuous-wave laser without mode-locking," *Opt. Lett.*, vol. 32, no. 11, pp. 1408-1410, June 2007.

[60] S. V. Chernikov and P. V. Mamyshev, "Femtosecond soliton propagation in fibers with slowly decreasing dispersion," J. Opt. Soc. Am. B, vol. 8, no. 8, pp. 1633-1641, Aug. 1991.

[61] J. J. O. Pires, J. R. F. da Rocha, "Performance analysis of DPSK direct detection optical systems in the presence of interferometric intensity noise," *J. Lightwave Technol.*, vol. 10, no. 11, pp. 1722-1730, Nov. 1992.

[62] R. P. Scott, C. Langrock, and B. H. Kolner, "High-dynamic-range laser amplitude and phase noise measurement techniques," *IEEE J. Select. Topics Quantum Electron.*, vol. 7, no. 4, pp. 641-655, July/Aug. 2001.

[63] D. von der Linde, "Characterization of the noise in continuously operating mode-locked lasers," *Appl. Phys. B*, vol. 39, pp. 201-217, 1986.

[64] K. R. Tamura and M. Nakazawa, “Femtosecond soliton generation over a 32-nm wavelength range using a dispersion-flattened dispersion-decreasing fiber,” *IEEE Photon. Technol. Lett.*, vol. 11, no. 3, pp. 319-321, March 1999.

[65] S.T. Cundiff, J. Ye, J.L. Hall, “Optical frequency synthesis based on mode-locked lasers,” *Rev. Sci. Instr.*, vol. 72, no. 10, pp. 3749-3771, Oct. 2001.

[66] M. Kourogi, K. Nakagawa, and M. Ohtsu, “Wide-span optical frequency comb generator for accurate optical frequency difference measurement,” *IEEE J. Quantum Electron.*, vol. 29, no. 10, pp. 2693-2701, Oct. 1993.

[67] Z. Jiang, D. E. Leaird, C.-B. Huang, H. Miao, M. Kourogi, K. Imai, A. M. Weiner, “Spectral line-by-line pulse shaping on an optical frequency comb generator,” *IEEE J. Quantum Electron.*, vol. 43, no. 12, pp. 1163-1174, Dec. 2007.

[68] E. Shekel, D. Majer, G. Matmon, A. Krauss, S. Ruschin, T. McDermott, M. Birk and M. Boroditsky, “Broadband testing of a 64x64 nanosecond optical switch,” in *Proceeding of 15th Annual Meeting of the IEEE-Lasers-and-Electro-Optics-Society*, Glasgow, Scotland, pp. 371-372, 2002.

[69] S. Osten, S. Kruger and A. Steinhoff, “Spatial light modulators based on reflective micro-displays,” *Technisches Messen*, vol. 73, no. 3, pp. 149-156, 2006.

[70] K. Igarashi, S. Saito, M. Kishi, M. Tsuchiya, “Broad-band and extremely flat super-continuum generation via optical parametric gain extended spectrally by fourth-order dispersion in anomalous-dispersion-flattened fibers,” *IEEE J. Select. Topics Quantum Electron.*, vol. 8, no. 3, pp. 521-526, May/June 2002.

[71] J. Hermann, U. Griebner, N. Zhavoronkov, A. Husakou, D. Nickel, J.C. Knight, W.J. Wadsworth, P.S.J. Russell, G. Korn “Experimental evidence for supercontinuum generation by fission of higher-order solitons in photonic crystal fibers,” *Phys. Rev. Lett.*, vol. 88, no. 17, 173901, Apr. 2002.

[72] L. A. Coldren and S. W. Corzine, *Diode Lasers and Photonic Integrated Circuits*, New York, NY, USA: John Wiley and Sons, 1995.